DISCOVERY OF A NEW BOSON IN THE SEARCH FOR A STANDARD MODEL HIGGS BOSON IN THE DIPHOTON FINAL STATE WITH THE ATLAS DETECTOR

by

Haichen Wang

A dissertation submitted in partial fulfillment of
the requirements for the degree of

Doctor of Philosophy

(Physics)

at the

UNIVERSITY OF WISCONSIN–MADISON

2013

Date of final oral examination: July 19, 2013

The dissertation is approved by the following members of the Final Oral Committee:

Yang Bai, Assistant Professor, Physics
Sridhara Dasu, Professor, Physics
Terrence Millar, Professor, Mathematics
Wesley Smith, Professor, Physics
Sau Lan Wu, Professor, Physics

To my parents.

ACKNOWLEDGMENTS

First of all, I am deeply grateful to my advisor, Professor Sau Lan Wu, whose dedication, perseverance, and insight have been a source of inspiration for me during my PhD years. She has been guiding and supporting my particle physics endeavor in so many different ways since I joined the Wisconsin ATLAS group.

The senior researchers, postdocs, and graduate students in the Wisconsin group are a group of intelligent and hardworking physicists. It is a great pleasure for me to work with them. I would like to especially thank Yaquan Fang, Andrew Hard, Hongtao Yang and Fuquan Wang. At various stages of my PhD program, I have worked with them on the search for $H \rightarrow \gamma\gamma$. We often stayed up late at night in the days, months, and even years leading up to the Higgs discovery. Many thanks to Luis Roberto Flores Castillo, Bill Quayle, Tapas Sarangi, Ximo Poveda, Lian-Liang Ma, Haiping Peng, Lashkar Kashif and Swagato Banerjee for sharing with me their perspective and experience in the field of particle physics. I want to thank Neng Xu, Wen Guan and Shaojun Sun for their technical support on computing. I also want to thank Haoshuang Ji, Haifeng Li, German Carrillo, Fangzhou Zhang, Xiangyang Ju, Yao Ming, Yang Heng, Alfredo Martin Castaneda

Hernandez, Isabel Pedraza, Elizabeth Castaneda Miranda, Sophio Pataraia, Haimo Zobernig, and Werner Wiedenmann, for the friendship that they have offered to me during the past years.

I have benefited a great deal from the interactions with my collaborators in the ATLAS collaboration over the past five years. I want to thank Eilam Gross, Marumi Kado, Louis Fayard, Junichi Tanaka, John Parsons, Nicolas Berger, Nansi Andari, Jana Schaarschmidt, Bill Murray, Alex Read, Krisztian Peters, Marc Escalier, Kerstin Tackmann, Bruno Lenzi, Daniel Froidevaux, Leonardo Carminati, Bertrand Laforge and Sandro De Cecco, for countless discussions and debates.

I also want to thank the administrative personnel at CERN and in Madison, including, Jane Schimmel, Aimee Lefkow, Renne Lefkow, Teresa Sherron, Sylvie Padlewski. My research could not be done without distractions, if they were not there to help.

Last but not the least, I want to thank my parents and my girl friend, Cheng Zhang. Over the past years, their support for my pursuing particle physics research has never wavered, even though that means less time spent with them. I owe a debt to them, which I never can pay back.

TABLE OF CONTENTS

Page

Appendix

Page

Appendix

Appendix

Page

Appendix

Page

APPENDICES

LIST OF TABLES

Appendix
Table Page

LIST OF FIGURES

Appendix
Figure Page

Appendix
Figure Page

Appendix
Figure Page

Appendix
Figure Page

Appendix
Figure Page

Appendix
Figure Page

Appendix
Figure Page

Appendix
Figure Page

Chapter 1

Introduction

The Standard Model of particle physics (SM) is an elegant and concise theory of elementary particles and their interactions. The electromagnetic, weak and strong interactions are described in a locally gauge invariant theory [1] based on an $SU(3) \bigotimes SU(2) \bigotimes U(1)$ gauge symmetry. The key development of the Standard Model happened in 1960s when the unification of electromagnetism and weak interactions was realized in a local gauge theory by Glashow, Weinberg, and Salam (GWS) [2, 3, 4, 5, 6]. Prior to 1960s, investigation of weak interaction data had pointed to the existence of a charged massive vector boson acting as the weak force carrier [7, 8]. In addition, a neutral weak boson had been postulated in the GWS model [3] although no experimental evidence had suggested the existence of this particle until 1973. One theoretical obstacle in establishing the unified electroweak theory was that the introduction of mass terms of weak bosons in the electroweak Lagrangian. A spontaneous symmetry breaking of a global symmetry could give rise to the mass of weak bosons, but that would necessarily introduce massless Goldstone bosons [9]. In 1964, Englert and Brout [10], Higgs [11], and others [12] demonstrated that the Goldstone bosons can be eliminated in the spontaneous symmetry breaking of a local gauge symmetry. This is usually referred to as the Higgs mechanism. In the simplest implementation of the Higgs mechanism, a scalar field is introduced, indicating the existence of a scalar boson which is usually referred to as the Higgs boson or the EBH boson.

In 1973, the existence of weak neutral current was confirmed in the observation of $\nu_\mu/\bar{\nu_\mu}$ + N $\rightarrow$ $\nu_\mu/\bar{\nu_\mu}$ + hadrons process [13]. In 1983, both the charged weak bosons $W^\pm$ [14, 15] and the neutral weak boson Z [16, 17] were observed at the CERN $Sp\bar{p}S$ collider. The experimental search for the Higgs boson has been conducted mostly at the Large Electron Positron collider at CERN and the Tevatron at Fermilab, and at various other experiments. As of the beginning of 2010, all previous experimental searches failed to observe the Higgs boson [18, 19].

The CERN Large Hadron Collider (LHC) is a 27-kilometer circular collider designed to collide two bunches of protons at $\sqrt{s} = 14$ TeV with an instantaneous luminosity of 10^{34} $\mathrm{cm}^{-2}\mathrm{s}^{-1}$ [20]. The search for the Higgs boson, as one of the most important goals of the LHC physics program, is carried out by two general purpose particle physics experiments, the ATLAS [21] and CMS [22] experiments. Two other major experiments at the LHC are the ALICE [23] and LHCb [24] experiments. The former specializes on heavy ion physics, and the latter on B-physics. The LHC started to produce collisions at $\sqrt{s} = 900$ GeV in 2009, and at $\sqrt{s} = 7$ TeV in 2010 with a low instantaneous luminosity of $\approx 1 \times 10^{31} - 2 \times 10^{32}$ $\mathrm{cm}^{-2}\mathrm{s}^{-1}$. In 2011, the LHC continued to collide protons at $\sqrt{s} = 7$ TeV but with a higher instantaneous luminosity, and the ATLAS experiment collected a data sample with an integrated luminosity of ≈ 5.2 fb^{-1}. In 2012, the LHC collided protons at $\sqrt{s} = 8$ TeV, and the ATLAS experiment collected a data sample with an integrated luminosity of ≈ 21.7 fb^{-1}. The LHC's peak instantaneous luminosity in 2012 reached 7.73×10^{33} cm^{-2}s^{-1}, close to the design instantaneous luminosity. The CMS experiment also collected data samples with similar integrated luminosities during the same period of time. The large data samples collected by the ATLAS and CMS experiments make the search for the SM Higgs boson for the first time sensitive in a large range of allowed Higgs boson mass.

This thesis presents the search for the Standard Model Higgs boson in the diphoton final state with the ATLAS detector at the LHC. With 4.8 fb^{-1} data at $\sqrt{s} = 7$ TeV taken in 2011 and 5.9 fb^{-1} data at $\sqrt{s} = 8$ TeV taken from March to June in 2012, an excess of diphoton events, corresponding to a statistical significance of 4.5 σ, is observed at 126.5 GeV. This observation, combined with observations of event excesses in the search for SM $H \rightarrow ZZ^{(\star)} \rightarrow 4l$ and the search for SM $H \rightarrow WW^{(\star)} \rightarrow l\nu l\nu$, established convincing evidence of the discovery of a new boson. Both the ATLAS and CMS collaborations submitted the discovery of this new boson in July, 2012 [25, 26].

After the 2012 data taking, the statistical significance of the excess in the diphoton final state in the 4.8 fb^{-1} data at $\sqrt{s} = 7$ TeV and 20.7 fb^{-1} data at $\sqrt{s} = 8$ TeV reaches 7.4 σ. The diphoton final state by itself can establish the discovery of the new boson. In addition to reporting the discovery of a new boson, this thesis also presents measurements of properties of the new boson in the diphoton final state with the full data samples collected in 2011 and 2012.

The coming chapters are organized as follows: Chapter 2 reviews the phenomenology of the SM Higgs boson and discusses the background to the $H \to \gamma\gamma$ signal. Chapter 3 describes the ATLAS experiment. Chapter 4 describes data sample collected in 2011 and 2012, the object reconstruction, and the diphoton event selection. Chapter 5 introduces the strategy to search for a SM Higgs boson in diphoton final state (the "search" analysis). Chapter 6 discusses the statistical methodology. Chapter 7 reports the observation of an excess of diphoton events in the data sample collected in 2011 and from March to June in 2012. The observations in the $H \to ZZ^{(\star)} \to 4l$ and $H \to WW^{(\star)} \to l\nu l\nu$ channels and the combination of all Higgs boson searches are also briefly summarized in this chapter. Chapter 8 describes the analysis strategy for measuring properties of the Higgs boson in the diphoton final state (the "measurement" analysis) and reports the statistical significance of the diphoton excess and measurement results with 4.8 fb^{-1} data at $\sqrt{s} = 7$ TeV and 20.7 fb^{-1} data at $\sqrt{s} = 8$ TeV. Chapter 9 concludes this thesis.

Chapter 2

Phenomenology

This chapter discusses the basics of the phenomenology of the SM Higgs boson. After a brief overview, Sec. 2.1 discusses the major SM Higgs boson production modes, and Sec. 2.2 discusses the Higgs boson decays, in particular, the $H \to \gamma\gamma$ decay. The major background to the $H \to \gamma\gamma$ signal is discussed in Sec. 2.3.

The mass of the Higgs boson is the least constrained part of the Standard Model. Prior to the start of LHC 2011 run, the experimental search at LEP excluded a SM Higgs boson with $m_H <$ 114.5 GeV [18], and the experimental search at Tevatron excluded a SM Higgs boson with 163 GeV $< m_H <$ 166 GeV [19]. The phenomenological profile of the Higgs boson and hence the search strategy depends on the m_H. Once the m_H is fixed, the phenomenological profile of the Higgs boson is well defined: its production cross section and decay branching ratios can be calculated from its coupling to fermions and weak bosons. Table 2.1 summarizes the coupling strengths between the Higgs boson and different type of particles.

Table 2.1 Summary of Higgs boson couplings to different particles. Here v is the vacuum expectation value of the Higgs field.

Coupling	Strength
$Hf\bar{f}$	M_f/v
HW^+W^-	$2M_W^2/v$
HZ^0Z^0	M_Z^2/v
HHW^+W^-	M_W^2/v^2
HHZ^0Z^0	$M_Z^2/2v^2$
HHH	$M_H^2/2v$
$HHHH$	$M_H^2/8v^2$

2.1 Production of the SM Higgs boson at the LHC

At the LHC, there are four major production modes for the SM Higgs boson, namely, the gluon fusion production (ggF), the vector boson fusion production(VBF), the production associated with a vector boson (VH), and the production associated with a pair of top quarks (ttH). Detailed discussion and references to the literature on these production modes can be found the in Ref. [27].

The dominant production mode of the SM Higgs boson at the LHC is the gluon fusion process, and its leading order(LO) Feynman diagram is shown in Fig. 2.1 [27]. Although gluons are massless bosons, it is possible that gluons couple to a Higgs boson through a massive colored particle loop. In the SM, the top quark loop provides the largest contribution to the gluon fusion cross section. Since the ggF cross section makes up approximately 90% of the total Higgs boson production cross section at the LHC, an observation of a Higgs boson with a cross section consistent with the

SM expectation would indicate the existence of the ggF production and hence indirectly confirm that the Higgs boson couples to fermions.

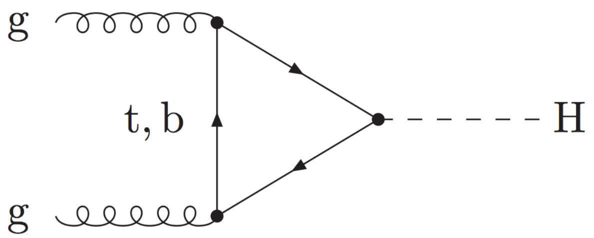

Figure 2.1 Feynman diagram contributing to $gg \to H$ at the lowest order.

The second dominant SM Higgs boson production mode at the LHC is the vector boson fusion (VBF) process. Fig. 2.2 [27] shows the Feynman diagrams of electroweak Higgs boson productions at the LHC. It is customary to refer to the t- and u-channel processes as the VBF production. The VBF Higgs boson signal is typically associated with two jets in the forward and backward regions of the detector, whereas the s-channel $qq \to qqH$ production contribution is suppressed after requiring the presence of two forward/backward jets. The VBF production process provides information about the coupling between the Higgs boson and weak bosons. Experimental observation of the VBF production would imply that the Higgs boson is responsible for the spontaneous symmetry breaking of the electroweak symmetry as it does couple to weak bosons.

The third largest SM Higgs boson production mode at the LHC is the production associated with vector bosons. The leading order Feynman diagrams of the VH production are shown in Fig. 2.3 [27] along with the contribution from $gg \to HZ$. The presence of a vector boson in

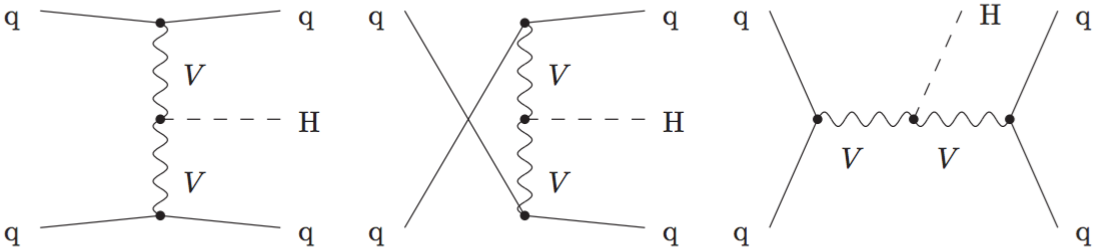

Figure 2.2 Topologies of t-, u-, and s-channel contributions for electroweak Higgs-boson production, $qq \rightarrow qqH$ at LO, where q denotes any quark or antiquark and V stands for W and Z boson.

the same event that produces the Higgs boson provides topological information that can be used to trigger the event. This is especially crucial in the search for $H \rightarrow b\bar{b}$ decay as the huge $b\bar{b}$ background at the LHC makes it unrealistic to trigger on the b-jets from the Higgs boson decay. It is also important to search and measure the VH production in other Higgs boson decay channels, including the $H \rightarrow \gamma\gamma$ channel, because the VH contribution and $H \rightarrow b\bar{b}$ contribution in the VH($\rightarrow b\bar{b}$) measurement can only be separated with the constraints on the VH production from channels other than $b\bar{b}$.

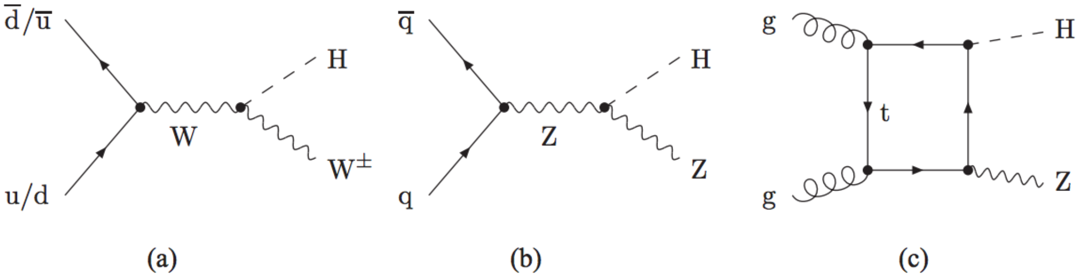

Figure 2.3 (a), (b) LO diagrams for the partonic processes $pp \rightarrow VH(V = W, Z)$; (c) diagram contributing to the $gg \rightarrow HZ$ channel.

Another important SM Higgs boson production mode at the LHC is the production associated with a top quark pair. Fig. 2.4 [27] shows the leading order Feynman diagrams of the ttH production. The ttH vertex is related to the Yukawa coupling between the Higgs boson and top quarks. The measurement of the ttH cross section, along with measurements of the Higgs boson's fermion decay branching ratios, can be used to test whether the coupling strength between the Higgs boson and a fermion is proportional to the fermion mass.

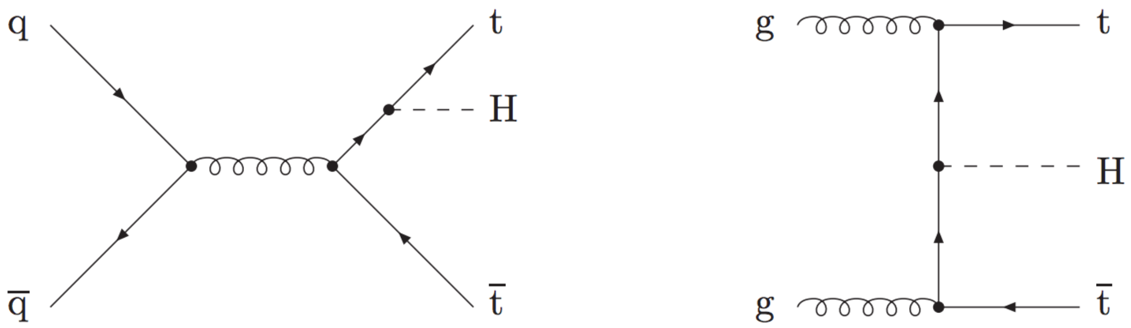

Figure 2.4 Examples of LO Feynman diagrams for the partonic processes $q\bar{q}, gg \rightarrow ttH$.

The cross sections of these production modes at $\sqrt{s} = 7$ TeV are shown as functions of m_H in Fig. 2.5 [27]. The total SM Higgs boson production cross sections at $\sqrt{s} = 7$ TeV, $\sqrt{s} = 8$ TeV and $\sqrt{s} = 14$ TeV are also shown in Fig. 2.5 [27].

The cross section of ggF production is very sensitive to the effect of QCD radiative corrections. The next-to-leading-order (NLO) calculation on the QCD correction increases the LO cross section by $80\text{-}100\%$ at the LHC [28, 29, 30, 31]. The next-to-next-to-leading-order(NNLO) calculation using the large-m_t limit approximation can further increase the ggF cross section by $\sim 25\%$ [32,

Figure 2.5 Standard Model Higgs boson production cross section as a function of m_H. The cross section at $\sqrt{s} = 7$ TeV is shown for each production mode in the left plot. The right plot shows the total production cross section at $\sqrt{s} = 7$ TeV, $\sqrt{s} = 8$ TeV and $\sqrt{s} = 14$ TeV.

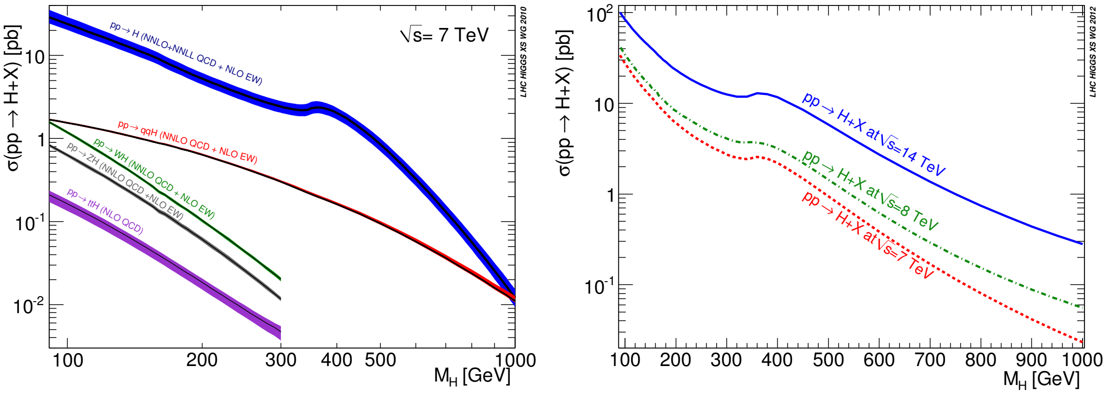

33, 34, 35, 36, 37, 38]. The large-m_t limit approximation has been shown to work extremely well for $m_H < 300$ GeV

The VBF production cross section is computed up to the NLO for QCD and EW corrections [39, 40, 41], and approximate calculations are also done up to NNLO for QCD corrections in VBF process [42]. The W/ZH processes are calculated up to NNLO [43, 44], and NLO EW radiative corrections [45] are included. The ttH process cross section is calculated up to NLO in QCD corrections [46, 47, 48, 49].

Tables 2.2 and 2.3 [27] show the cross sections of these major production modes at the LHC at a few benchmark m_H points for $\sqrt{s} = 7$ TeV and $\sqrt{s} = 8$ TeV, respectively.

Table 2.2 The Higgs boson production cross section at a few benchmark m_H at $\sqrt{s} = 7$ TeV at the LHC.

m_H (GeV)	ggF	VBF	WH	ZH	ttH
			(pb)		
115	18.1	1.34	0.755	0.411	0.111
125	15.3	1.22	0.572	0.316	0.0863
150	10.6	0.980	0.300	0.171	0.0487
500	0.871	0.141	-	-	-

Table 2.3 The Higgs boson production cross section at a few benchmark m_H at $\sqrt{s} = 8$ TeV at the LHC.

m_H (GeV)	ggF	VBF	WH	ZH	ttH
			(pb)		
115	22.7	1.73	0.927	0.536	0.165
125	19.3	1.58	0.705	0.415	0.129
150	13.6	1.28	0.373	0.231	0.0736
500	1.28	0.156	-	-	-

2.2 Decays of the SM Higgs boson

The branching ratio of the Higgs boson is shown as a function of m_H between 100 GeV and 1 TeV in Fig. 2.6 [27] for various decay final states. The features in these curves can be understood from the partial widths of the weak boson and fermion final states [50, 51, 52, 53]:

$$\Gamma(H \to f\bar{f}) = \frac{N_c g^2 m_f^2}{32\pi m_w^2} \beta^3 m_H \tag{2.1}$$

$$\Gamma(H \to VV) = N_C \frac{g^2}{128\pi} \frac{m_H^3}{m_V^2} \sqrt{1 - x_V}(1 - x_V + \frac{3}{4}x_V^2) \tag{2.2}$$

Figure 2.6 Standard Model Higgs boson decay branching ratio is shown as a function of m_H for individual final states (left). The width of the Higgs boson is also shown as a function of m_H (right).

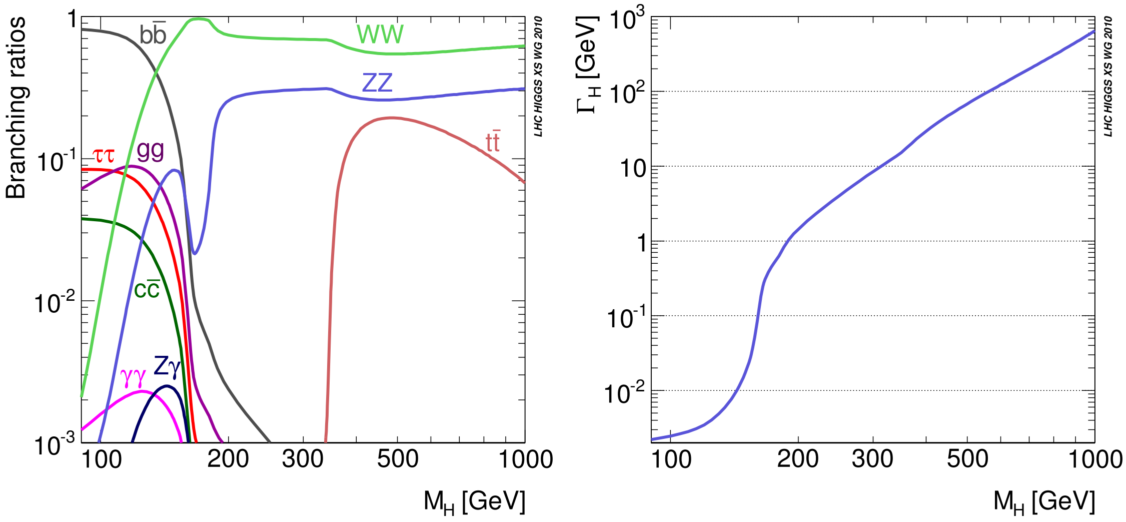

In Eqs. 2.1 and 2.2, g is the standard $SU(2)$ gauge group coupling, $V = W, Z$, f represents fermions, $\beta = 1 - 4m_f^2/m_H^2$, and $x_V = 4m_V^2/m_H^2$. Compared to a lepton pair final state, a quark pair final state gains an additional factor of $N_c = 3$ in its partial width as a result of having the quantum number of color. Similarly, the WW final state gains a factor of $N_C = 2$ in its partial width compared to the ZZ final state, due to its having the quantum number of charge.

In the Higgs boson mass range of $m_H < 130$ GeV, the VV final states are kinematically disfavored and the $t\bar{t}$ final state is not allowed. Therefore, the dominant decay final state is $b\bar{b}$ since the b-quark is the heaviest fermion with a mass less than 130 GeV. Above 130 GeV, the VV final states gradually open, and they account for $\approx$90% of the Higgs boson decays even when the $t\bar{t}$ final state is opened. This is primarily because $\Gamma(H \to VV)$ is proportional to m_H^3 while $\Gamma(H \to f\bar{f})$ is proportional to m_H.

What are not explained by Eqs. 2.1 and 2.2 are the three final states that consist of at least one massless particle, namely, gg, $\gamma\gamma$, and $Z\gamma$. They are all loop-induced decays. The $H \to gg$ decay is induced by a colored particle loop (Fig. 2.7 [54]), similar to the gluon fusion production of Higgs boson.

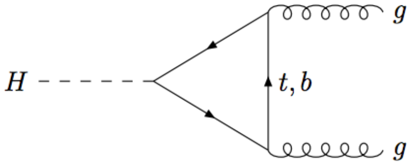

Figure 2.7 Feynman diagrams contributing to $H \to gg$ at the lowest order.

The $H \to \gamma\gamma$ and $H \to Z\gamma$ decays are both induced by charged particle loops (Fig. 2.8 [54]). In the SM, the W-loop is the largest contribution to the $H \to \gamma\gamma$ decay, and the second largest contribution comes from a top-loop. The W-loop and top-loop contributions lead to a destructive interference in the $H \to \gamma\gamma$ partial width. The loop-induced decays of $H \to \gamma\gamma$ and $H \to Z\gamma$ are sensitive to potential contributions from charged particles in some Beyond the Standard Model

(BSM) theories, and thus the measurements of the two decay branching ratios can provide valuable constraints on these BSM scenarios.

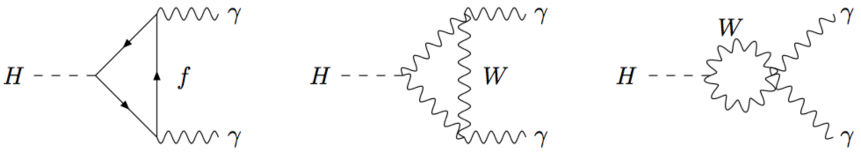

Figure 2.8 Feynman diagrams contributing to $H \to \gamma\gamma$ at the lowest order.

In the SM, the $H \to \gamma\gamma$ decay is at the level of $\approx (1-2) \times 10^{-3}$ in the region of 110 GeV $< m_H <$ 150 GeV. Although the $H \to \gamma\gamma$ branching ratio is tiny, the diphoton final state provides the possibility of reconstructing a narrow peak that can be used to discriminate against the QCD background continuum.

Table. 2.4 [27] shows the branching ratio for $\gamma\gamma$, $b\bar{b}$, WW and ZZ final states at a few benchmark m_H.

Table 2.4 The Higgs boson decay branching ratio for $\gamma\gamma$, $b\bar{b}$, WW and ZZ final states at a few benchmark m_H.

m_H (GeV)	$\gamma\gamma$	$b\bar{b}$	WW	ZZ
115	2.11×10^{-3}	7.03×10^{-1}	8.60×10^{-2}	8.65×10^{-3}
125	2.28×10^{-3}	5.77×10^{-1}	2.15×10^{-1}	2.64×10^{-2}
150	1.37×10^{-3}	1.57×10^{-1}	6.96×10^{-1}	8.25×10^{-2}
500	3.12×10^{-7}	1.09×10^{-4}	5.46×10^{-1}	2.61×10^{-1}

2.3 Background

At the LHC, diphoton events can be promptly produced from the proton-proton collisions via several processes. At the lowest order of α_s, there are the box process $gg \to \gamma\gamma$ (Fig. 2.10), the Born process $q\bar{q} \to \gamma\gamma$ (Fig. 2.9), and the Bremstrahlung process $qg \to q\gamma\gamma$ (Fig. 2.9) where one of the final state photons comes from a quark line. Photons can also come out of quark fragmentations (Fig. 2.11 and Fig. 2.12 [1]) and this gives additional contribution to the diphoton production at the LHC. These processes produce genuine diphoton events and are the "irreducible" background to the $H \to \gamma\gamma$ signal process.

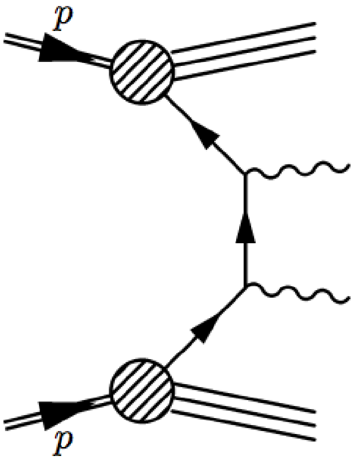

Figure 2.9 The diagrams for the lowest order $\gamma\gamma$ production.

There are also "reducible" backgrounds at the LHC. These backgrounds are mostly from $\gamma-$jet production where one genuine photon is produced and at least one jet is mis-identified as a photon

---

[1] Diagrams in Figures 2.10, 2.9, 2.11 and 2.12, are taken from the DIPHOX paper [55].

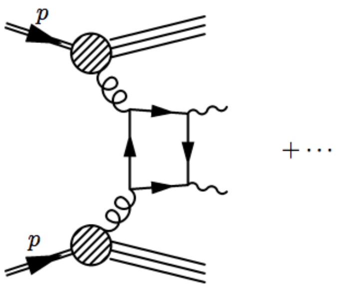

Figure 2.10 The diagrams for $\gamma\gamma$ production via the “box” process.

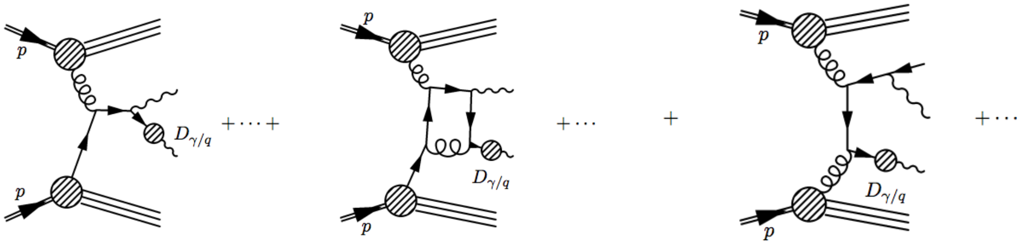

Figure 2.11 The diagrams for the $\gamma\gamma$ production where one photon is produced from the fragmentation of a quark.

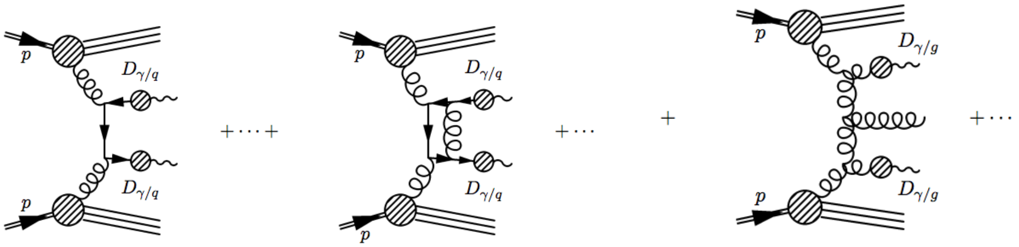

Figure 2.12 The diagrams for the $\gamma\gamma$ production where both photons are produced from quark fragmentations.

in the electromagnetic calorimeter. The multi-jets production can also contribute to the reducible background.

Table 2.5 shows the production cross sections for $\gamma\gamma$, γ-jet and multi-jets processes at $\sqrt{s} = 8$ TeV and $\sqrt{s} = 14$ TeV. The $\gamma\gamma$ cross section includes the contributions from Born and box processes and is calculated by DIPHOX [55, 56, 57] at the NLO. The $\gamma-$jet and multi-jets cross sections are calculated at the LO by Pythia [58]. The numbers in Table 2.5 can be used to give a rough estimation of the signal-to-background ratio in the $\gamma\gamma$ final state. The cross section of genuine $\gamma\gamma$ background is about $2-3$ orders of magnitude higher than the cross section of Higgs boson production times the $H \to \gamma\gamma$ branching ratio. In addition, the cross sections of γ-jet background and multi-jets are higher than the cross section of the genuine $\gamma\gamma$ production by 3 and 6 orders of magnitude, respectively. This means that the search for the $H \to \gamma\gamma$ signal requires the electromagnetic calorimeter have a very powerful γ-jet separation capability and excellent resolution for reconstructing the $H \to \gamma\gamma$ resonance.

Table 2.5 The production cross sections for $\gamma\gamma$, $\gamma-$jet and multi-jets processes at the LHC at $\sqrt{s}$ = 8 TeV and $\sqrt{s}$ = 14 TeV. The $\gamma\gamma$ cross section includes the contributions from Born and box processes and is calculated by DIPHOX at the NLO. The $\gamma-$jet and multi-jets cross sections are calculated at the LO by Pythia.

$\sqrt{s}$ (TeV)	$\gamma\gamma$	$\gamma-$jet (pb)	multi-jets
8	12.13	4.4 $\times 10^4$	1.5 $\times 10^8$
14	21.72	8.9 $\times 10^4$	3.7 $\times 10^8$

Chapter 3

The ATLAS detector

This chapter gives a brief introduction to the ATLAS detector system. The detailed documentation about the ATLAS experiment can be found in Ref. [21].

3.1 Overview

The ATLAS detector is a general purpose particle physics detector at the LHC. It has a forward-backward symmetric, cylindrical geometry, and a coverage in solid angle close to $4\pi^1$. The overall detector layout can be found in Fig. 3.1 [21]. The main performance goals of the experiment can be found in Table 3.1 [21]. The innermost part of the ATLAS detector system is the inner tracking detector, which is immersed in a 2 T solenoidal magnetic field. A Liquid Argon sampling calorimeter, locating outside the inner tracking detector, provides precision measurements of the electromagnetic objects. The hadronic calorimeter system, surrounding the electromagnetic calorimeter, consists of a Tile hadronic calorimeter, a Liquid Argon hadronic Endcap calorimeter,

---

[1] ATLAS uses a right-handed coordinate system with its origin at the nominal interaction point (IP) in the centre of the detector, and the z-axis along the beam line. The x-axis points from the IP to the centre of the LHC ring, and the y-axis points upwards. Cylindrical coordinates (r, ϕ) are used in the transverse plane, ϕ being the azimuthal angle around the beam line. Observables labelled "transverse" are projected into the $x - y$ plane. The pseudorapidity is defined in terms of the polar angle θ as $\eta = -\ln\tan(\theta/2)$. The transverse momentum is defined as $p_{\mathrm{T}} = p\sin\theta = p/\cosh\eta$, and the transverse energy E_{T} has a similar definition.

and a Liquid Argon Forward calorimeter. The outermost part of the ATLAS detector is a muon spectrometer with an air-core toroid system. A trigger system that has a hardware based Level 1 trigger system and a computer farm-based High Level Trigger system is capable of keeping the event taking rate to the level of approximately of 200 Hz.

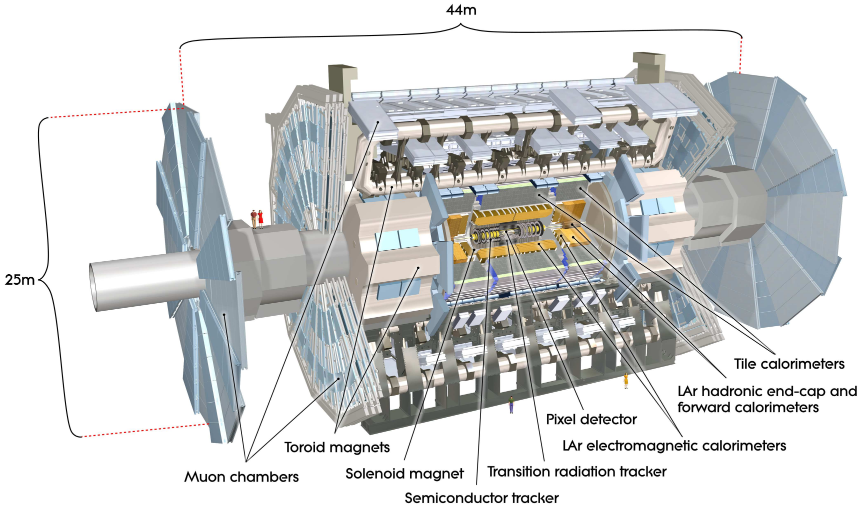

Figure 3.1 Cut-away view of the ATLAS detector.

3.2 Inner Tracking Detector

The ATLAS Inner Tracking Detector (ID) system consists of pixel and silicon microstrip (SCT) trackers and a Transition Radiation Tracker (TRT), extending over 5.3 m in length with a diameter of 2.5 m. The layout of the Inner Detector is shown in Fig. 3.2 [21].

A central solenoid generates a 2 T magnetic field that permeates the entire ID system. The pixel and SCT detectors cover the pseudorapidity range of $|\eta| < 2.5$. In the barrel region, these

Table 3.1 General performance goals of the ATLAS detector. For high-p_T muons, the muon spectrometer performance is independent of the inner detector system. The units for E and p_T are in GeV.

Detector component	Required resolution	η coverage
Tracking	$\sigma_{p_T}/p_T = 0.05\% p_T \bigoplus 1\%$	±2.5
EM calorimetry	$\sigma_E/E = 10\%/\sqrt{E} \bigoplus 0.7\%$	±3.2
Hadronic calorimetry		
barrel and end-cap	$\sigma_E/E = 50\%/\sqrt{E} \bigoplus 3\%$	±3.2
forward	$\sigma_E/E = 100\%/\sqrt{E} \bigoplus 10\%$	$3.1 < \lvert\eta\rvert < 4.9$
Muon spectrometer	$\sigma_{p_T}/p_T = 10\%$ at $p_T = 1$ TeV	±2.7

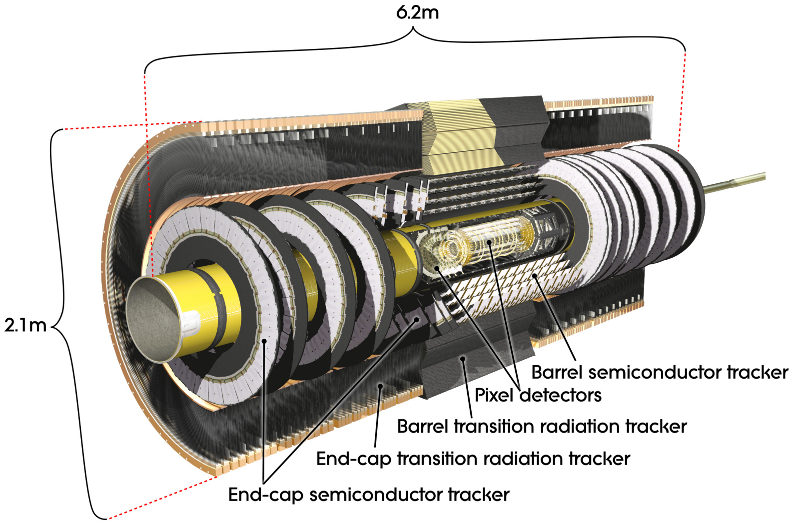

Figure 3.2 Cut-away view of the ATLAS Inner Detector.

two detectors are attached to concentric cylinders around the beam axis. In the endcap regions, they are arranged on disks perpendicular to the beam axis. The pixel detector is finely segmented in $R-\phi$ and z with a minimum pixel size of 50×400 μm^2, and it has approximately 80.4 million readout channels. A track typically crosses three layers of the pixel detector. The measurement accuracy for such a track can be as good as 10 μm in $R - \phi$ and 115 μm in z. The SCT detectors have small angle stereo strips parallel to the beam axis in the barrel region and strips perpendicular to the beam axis in the endcap region. The number of SCT readout channels is approximately 6.3 millions. A track typically crosses eight strip layers at four space points. The intrinsic accuracies per module can be as good as 17 μm in $R - \phi$ and 580 μm in z.

The TRT, with 4 mm straw tubes, provides measurement in $R - \phi$. There are typically 36 hits per track. The TRT barrel straws are 144 cm in length and parallel to the beam axis, and TRT endcap straws are attached to wheels perpendicular to the beam axis. The intrinsic accuracy of TRT is 130 μm per straw. The total number of TRT readout channels is approximately 351000.

A robust pattern recoginition and high precision measurements of tracks are achieved by a combination of measurements from the precision pixel and SCT trackers at small radii and the TRT at a larger radius.

3.3 Calorimetry

The ATLAS calorimetry system consists of a Liquid Argon electromagnetic calorimeter and hadronic calorimeters. Fig. 3.3 [21] shows a cut-away view of the calorimetry system.

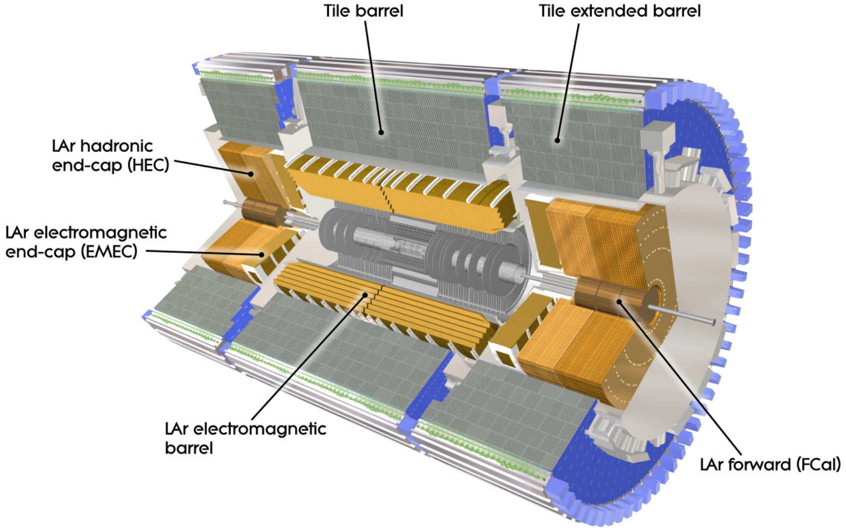

Figure 3.3 Cut-away view of the ATLAS calorimeter system.

The electromagnetic calorimeter is a fine-grained lead-liquid argon sampling calorimeter that consists of a central barrel calorimeter covering pseudorapidity range of $|\eta| < 1.45$, and two end-cap calorimeters covering $1.375 < |\eta| < 3.2$. In the region of $|\eta| < 2.5$, the calorimeter has three longitudinal layers and allows precision measurements of electromagnetic (EM) objects. The first EM calorimeter layer is finely divided into cells with a granularity of $\Delta\eta = 0.003$-0.006, depending on η. This design provides strong discrimination power between single photon showers and EM showers resulted from two photons from π_0 decays. The second layer, where EM objects deposit the most energy, has a granularity of $\Delta\eta \times \Delta\phi = 0.025 \times 0.025$. The third layer mainly measures the energy deposit from a highly energetic EM object and also provides an estimation of EM object's energy leakage into the hadronic calorimeter. A presampler, covering $|\eta| < 1.8$, is used to correct for energy loss upstream of the calorimeter. A sketch of the three-layer structure of the EM calorimeter is shown in Fig. 3.4 [21].

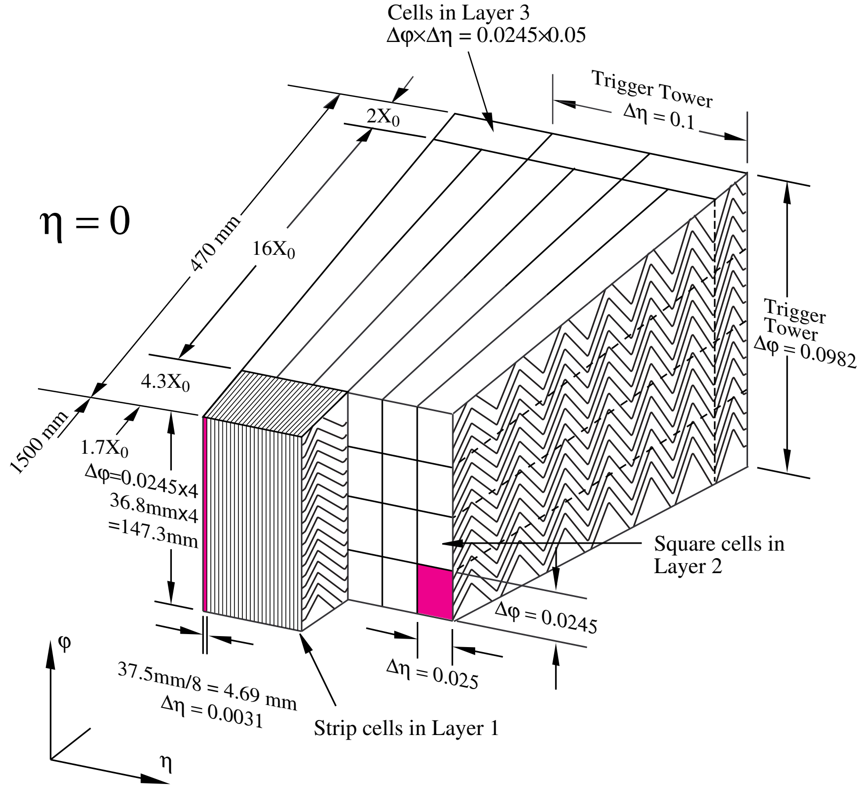

Figure 3.4 Sketch of a barrel module where the different layers are clearly visible with the ganging of electrodes in phi. The granularity in η and ϕ of the cells of each of the three layers and of the trigger towers is also shown.

The hadronic calorimeter system consists of a Tile calorimeter covering $|\eta| < 1.7$, a LAr hadronic endcap calorimeter covering $1.5 < |\eta| < 3.2$, and a LAr forward calorimeter. The Tile calorimeter is immediately outside the electromagnetic calorimeter envelope, with a barrel in the region of $|\eta| < 1.0$, and two extended barrels in the region of $0.8 < |\eta| < 1.7$. The Tile calorimeter is segmemted in depth into three layers and divided azimuthally into 64 modules. The absorber of the Tile calorimeter is steel and the active material is scintillating tiles. The Hadronic End-cap Calorimeter has two wheels for each end-cap and they are located immediately outside the end-cap electromagnetic calorimeter. Each wheel is segmented into two layers in depth, totaling four layers for each end-cap.

3.4 Muon system

The layout of the muon spectrometer is shown in Fig. 3.5 [21].

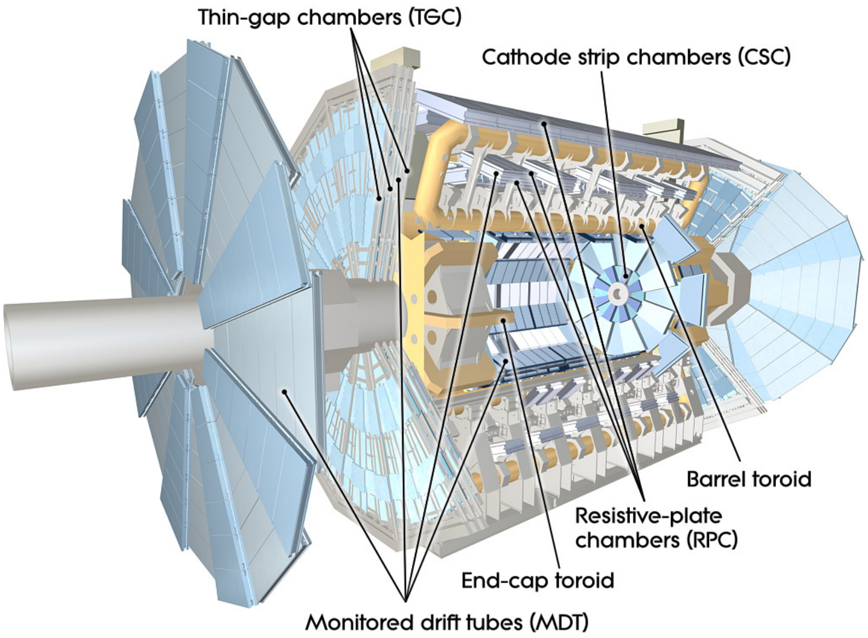

Figure 3.5 Cut-away view of the ATLAS muon system.

The muon chambers are immersed in a magnetic field generated by a system of three large toroids. The Monitored Drift Tubes (MDTs) provide a precision measurement of the track coordinates in the principal bending direction over most of the η range. The Cathode Strip Chambers (CSCs) are used in the innermost plane over $2 < |\eta| <$2.7. The relative alignments of the muon chamber layers are realized by precision mechanical assembly techniques and optical alignment systems. The muon trigger system, consisting of Resistive Plate Chambers(RPCs) in the barrel and Thin Gap Chambers (TGCs) in the end-cap, provides bunch crossing identification, determine the p_T thresholds, and measures the track coordinate in the direction orthogonal to that measured by the precision tracking chambers.

Chapter 4

Data sample and object reconstruction

This chapter summarizes the ATLAS experiment's data-taking in 2011 and 2012, describes the reconstruction of objects such as photons, electrons, muons, jets, and E_T^{miss}, and details the diphoton event selection for both the "search" analysis and the "measurement" analysis.

4.1 Data taking

The LHC started delivering pp collisons in Novmeber, 2009. A total of 9 μb^{-1} data at $\sqrt{s} = 900$ GeV were collected. In 2010, the LHC collision energy increased to 7 TeV, and a total of 36 pb^{-1} data were collected.

In 2011, the LHC continued to collide protons at $\sqrt{s} = 7$ TeV. The data-taking started in March and finished on October. The instantaneous luminosity gradually increased from $\sim\ 1.0 \times 10^{32}$ cm^{-2}s^{-1} to 3.65×10^{33} cm^{-2}s^{-1} over the entire period of 2011 data taking. The integrated luminosity of the collected 2011 data is 5.25 $\pm$ 0.09 fb^{-1}, and the average mean number of interactions per bunch crossing is 9.1.

In 2012, the LHC collision energy increased to 8 TeV, and the data-taking started in March and finished in November. This year also saw an increase in the instantaneous luminosity; most runs achieved an instantaneous luminosity beyond 5.0×10^{33} cm^{-2}s^{-1}, and the peak instantaneous luminosity reached 7.73×10^{33} cm^{-2}s^{-1}. On June 18, 2012, the LHC started a technical stop that lasted until July 2, 2012, and a data sample with an integrated luminosity of 5.2 fb^{-1} had been collected prior to this technical stop. The discovery of a new boson in the Standard Model Higgs boson searches was based on analyses of this sample and the 2011 sample. The integrated lumionsity of the entire 2012 run is about 21.7 fb^{-1}, and the average mean number of interactions per bunch crossing is 20.7.

The data used in the physics analysis should meet certain data quality requirements. In general, all subdetector systems should be fully functioning during a run and no irrecoverable data defects should be present in a run. After the data quality requirement, 4.8 fb^{-1} data at $\sqrt{s} = 7$ TeV and 20.7 fb^{-1} data at $\sqrt{s} = 8$ TeV are available for this analysis.

4.2 Photon reconstruction

4.2.1 Clusterization

The reconstruction of photon starts with the clusterization in the EM calorimeter. A cluster is formed if the sum of transverse energies from three calorimeter layers and the presampler in a projective tower with a size of $\Delta\eta \times \Delta\phi = 0.075 \times 0.125$ exceeds 2.5 GeV. A matching in η and ϕ is performed between the EM cluster in the calorimeter and the extrapolated tracks reconstructed in the inner detector. Clusters that fail to match any tracks are classified as unconverted photon candidates. Clusters that are matched to a pair of tracks sharing the same conversion vertex or a single track without a pixel hit in the layer nearest to the beam pipe are classified as converted photon candidates.

Depending on the conversion status and η position of the photon candidate, different cluster sizes are used to measure the energy and direction of a photon candidate. In the EM calorimeter barrel ($|\eta| < 1.45$), the size of the photon cluster in $\Delta\eta \times \Delta\phi$ is 0.075×0.125 for unconverted photon candidates, and 0.075×0.175 for converted photon candidates. The converted photon cluster is expanded in the ϕ dimension compared to the unconverted photon cluster, in order to cover the larger energy spread resulting from the electron and/or positron of photon conversion. In the EM calorimeter endcap ($1.45 < |\eta| < 2.5$), the cluster size is 0.125×0.125 in $\Delta\eta \times \Delta\phi$ for both unconverted and converted photon candidates.

4.2.2 Energy calibration

A Monte Carlo based calibration is performed by using energy deposit information from the three layers and the presampler [59, 60]. The calibration procedure needs to be applied separately for unconverted and converted photons as their shower developments in the calorimeter and upstream energy losses are different. This calibration critically depends on correctly simulating the calorimeter response to an EM object and accurately describing the materials upstream of the EM calorimeter. The current ATLAS detector simulation has been tuned with test beam data [61]. In addition, the description of the materials is validated from data. This Monte Carlo-based calibration is applied to EM objects in both data and Monte Carlo samples.

Additionally, an η-dependent energy scaling factor is derived from data-MC comparison in $Z \to ee$ samples and is applied to EM objects. This scaling factor corrects the electron energy so that the Z line shape in the Monte Carlo sample can match that in data. By applying such a scaling factor derived from an electron sample to photons, the difference in shower behavior and (its resulting difference in) detector performance between electrons and photons are ignored. This should be accounted for as the systematic uncertainty of the energy measurement.

4.2.3 Photon identification

The photon identification is based on energy deposit information in different layers of the EM calorimeter. Statistically, fake photon candidates tend to have a broader shower compared to genuine photon candidates. Besides, the energy deposit of a fake photon candidate from the $\pi_0 \to \gamma\gamma$ decay can have two energy maxima in the first layer of the EM calorimeter. Several shower shape variables are defined to reflect differences in the longitudinal and lateral shower profiles between genuine photons and fake photons.

In ATLAS, two identification methods are developed. The first one is a $cut - based$ identification method. For each shower shape variable, an η-dependent cut is applied so that genuine photon candidates and fake photon candidates can be separated. A set of cuts on photon shower shape variables are optimized and the combination of these optimized cuts constitutes the photon identification requirement. In the other identification method, a neutral network discriminator is trained using these shower shape variables, and the photon identification menu is defined by an optimized η-dependent cut on the neutral network response. The neural network identification can achieve a better photon efficiency with a jet rejection similar to the cut-based identification. For each identification method, a $loose$ requirement and a $tight$ requirement are defined. Only the second layer shower shape variables and the EM shower's leakage into the hadronic calorimeter are used to define the $loose$ requirement. The tight selection further takes advantage of the information from the first layer shower shape variables and tightens the cuts on the second layer shower shape variables. The neural network identification is used to select photons from the 2011 sample, while the cut-based identification is used for the 2012 analysis.

In the Monte Carlo sample that is used to optimize the photon identification requirement, the shower shape variables are shifted slightly in order to achieve a better data and Monte Carlo agreement in these distributions. For a genuine photon from a Higgs boson decay, the tight identification efficiency varies from 85% to 95% in the p_T range beyond 30 GeV. The identification related systematic uncertainty is described in Sec. 5.3.

4.2.4 Photon isolation

In addition to photon identification requirement, the photon isolation that reflects the hadronic activity around the photon candidate is also used to reject fake photon candidates.

The isolation variable can be built either using the calorimeter information or using the tracking information. The calorimeter isolation variable is defined as the sum of the transverse energies of positive energy topological clusters [62] in a cone of size $\Delta R = \sqrt{(\Delta\eta)^2 + (\Delta\phi)^2} < 0.4$ around the photon cluster. In the calculation of the isolation energy, the contribution from the photon candidate is excluded, and effects introduced by pile-up and underlying events are corrected on an event-by-event basis. Fig. 4.1 shows distributions of calorimeter isolation for genuine photons and fake photons. The shape of the calorimeter isolation is different between genuine photons and fake photons even after the *tight* photon identification is required. This means that applying calorimeter isolation brings additional suppression of fake photons. The tracking isolation variable is defined as the scalar sum of the transverse momenta of tracks inside a cone of size $\Delta R < 0.2$ around the photon cluster. Those tracks should be associated with the vertex from which the two

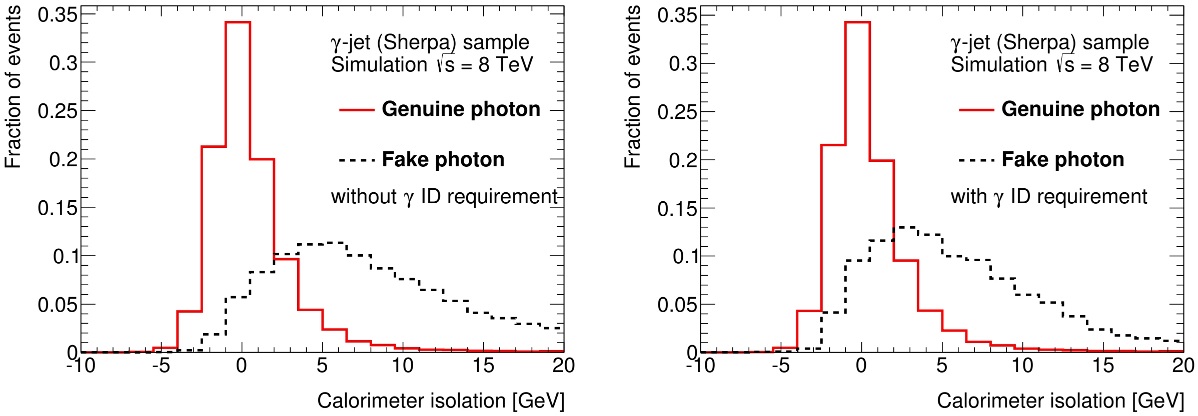

Figure 4.1 Distributions of calorimeter isolation for genuine photons and fake photons. Left plot shows the distributions of photon candidates without requiring photon identification. Right plot shows the distributions of photons that pass the *tight* identification requirement.

photon candidates originated. Tracks that are associated with the converted photon candidates are excluded from the calculation of track isolation. Fig. 4.2 shows the distributions of track isolation for genuine photons and fake photons, and the majority of photon candidates have a track isolation value of 0.

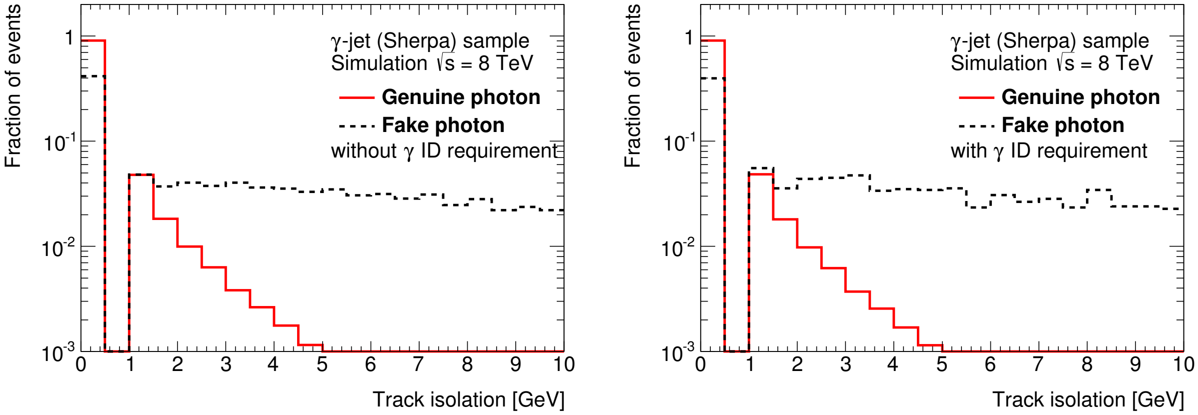

Figure 4.2 Distributions of track isolation for genuine photons and fake photons. Left plot shows the distributions of photon candidates without requiring photon identification. Right plot shows the distributions of photons that pass the *tight* identification requirement.

4.2.5 Photon direction measurement

The photon direction measurement is critically dependent on the determination of the interaction point position. In principle, the flight direction of a photon can be naturally determined by extrapolating the photon shower to the interaction point. In ATLAS, the spread of the beam spot position in the x or y directions is negligible, but the spread of the beam spot in z direction is about 5 cm. This means that assuming the detector coordinate origin as the interaction point would introduce a contribution of $\sim$ 1.4 GeV to the diphoton mass resolution. To better determine the z position of the interaction point, a combination of information from multiple sources is used.

First, the primary vertex of the event is reconstructed from tracks in the event and can give a good measurement of the z position of the interaction point. In a high pile up environment, multiple primary vertex candidates can be reconstructed in the same event. It is common to assume the primary vertex is the one whose sum of track p_T^2 is the highest. This vertex provides one measurement of the interaction point position.

Second, the ATLAS EM calorimeter is a sampling calorimeter that provides measurements of the photon shower position in its longitudinal compartments. The barycenters of the energy deposits in the first and second layers can be determined precisely due to the fine granularities of these two layers. These two barycenters can be used to define a straight line that crosses the beam pipe and therefore determines the z position origin of the photon. This extrapolation is usually referred to as the "calorimeter pointing", and it provides one additional measurement of the interaction point per photon.

Third, approximately 60% of the photons in the selected diphoton events are converted photons which have at least one associated track. The conversion track can be extrapolated back to the beam line, giving one additional measurement of the interaction point per converted photon. This information is only used for the z determination in the $\sqrt{s} = 7$ TeV sample due to more severe pile-up impact on the photon conversion reconstruction in the $\sqrt{s} = 8$ TeV data.

In ATLAS, all these measurements are used in a combined likelihood method that determines the primary vertex candidate that is most likely to be the true reconstructed vertex. This likelihood method is used for the "search" analysis. Fig. 4.3 shows the $m_{\gamma\gamma}$ distributions reconstructed with different vertex z measurement methods from a Higgs boson signal sample at m_H = 125 GeV at $\sqrt{s} = 8$ TeV. The $m_{\gamma\gamma}$ with z measured from the likelihood method has the best performance and the contribution to the $m_{\gamma\gamma}$ resolution from the measurement of z is negligible. Between different measurements, the most important improvement in $m_{\gamma\gamma}$ resolution comes from the calorimeter pointing information.

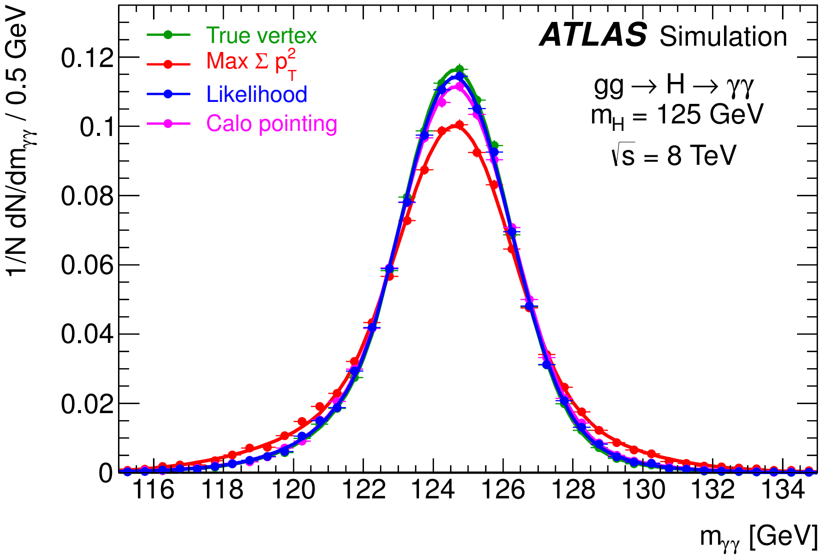

Figure 4.3 Distribution of the expected diphoton mass for $H \rightarrow \gamma\gamma$ signal events as a function of the algorithm used to determine the longitudinal vertex position of the hard-scattering event. The use of the calorimeter information, labelled as "Calo pointing" is fully adequate to reach the optimal achievable mass resolution labeled as "True vertex".

For the "measurement" analysis, a neural network discriminant is trained to find the reconstructed primary vertex candidate that best fits in the characteristics of the true primary vertex. The following variables are used: the diphoton vertex z position and its error from the calorimeter pointing measurement, the diphoton vertex z position and its error from the conversion extrapolation(when applicable), the sum of squared momenta of tracks associated with the vertex, Σp_T^2, the scalar sum of momentum of tracks associated with the vertex, Σp_T, the difference in the azimuthal angle ϕ between the direction defined by the vector sum of all associated tracks momenta and the direction of the diphoton system.

4.3 Reconstruction and selection of other objects

In this analysis, objects such as jets, leptons and E_T^{miss} are used to select signal events with a particular topology. The reconstruction and selection of these objects are briefly described here. Jet objects are used in both the "search" analysis and the "measurement" analysis, and lepton objects and E_T^{miss} are only used in the "measurement" analysis.

4.3.1 Jet reconstruction and selection

Jets are reconstructed by using the anti-k_t algorithm [63] in which the distance parameter R is 0.4. The jet finding is seeded from a three-dimensional topological calorimeter cluster [62, 64, 65]. The energy calibration of the jet is done in three steps. First, the pile-up contribution is removed by applying corrections that are dependent on the number of primary vertices and the average number of interactions per bunch crossing [66]. These corrections are derived from Monte Carlo samples. In the second step, another correction is applied so that the jet direction is adjusted to point to the primary vertex identified as the one with the highest $\sum p_T^2$ of all the associated tracks [65]. In the third step, an energy and rapidity-dependent correction derived from Monte Carlo is applied [65]. For the $\sqrt{s} = 7$ TeV data, jet four-momenta are also corrected with data-driven calibrations that exploit the transverse momentum balance between a jet and a reference object [67].

4.3.1.1 Jet selection in the “search” analysis

In the “search” analysis, a jet is selected if it passes following requirements:

- its pseudo-rapidity η_j is in the region of $|\eta_j| < 4.5$.
- its transverse momentum $p_{T,j}$ is greater than 25 GeV. For the $\sqrt{s} = 8$ TeV sample, the $p_{T,j}$ is required to be greater than 30 GeV if η_j is in the region of $2.5 < |\eta_j| < 4.5$.
- the jet-vertex-fraction (JVF) should be larger than 0.75 if η_j is less than 2.5. The jet-vertex-fraction is defined as ratio of the scalar sum of p_T of tracks associated with both the jet and the primary vertex identified by the vertex finding algorithm over the scalar sum of p_T of all tracks associated with the jet.

4.3.1.2 Jet selection in the “measurement” analysis

In the “measurement” analysis, a jet is selected if it passes the following requirements

- its pseudo-rapidity η_j is in the region of $|\eta_j| < 4.5$.

- its transverse momentum $p_{T,j}$ is greater than 25 GeV. For the $\sqrt{s} = 8$ TeV sample, the $p_{T,j}$ is required to be greater than 30 GeV if η_j is in the region of $2.4 < |\eta_j| < 4.5$.

- the jet-vertex-fraction should be larger than 0.25 if η_j is less than 2.4. The jet-vertex-fraction requirement is loosened with respect to the "search" analysis as the "search" requirement is considered to be too tight for the full 2012 dataset where events have very high pile-up. The $|\eta_j|$ range where the JVF is applicable is also reduced so that jets at the edge of inner detector coverage are exempt from the requirement.

4.3.2 Electron reconstruction and selection

Electron candidates originate from the same clusterization procedure used for the photon candidates. The clusters that are matched to tracks extrapolated from the inner detector are classified as electron candidates. The energy and momentum calibration procedure is similar to that of photon, but the information from electron track in the inner detector is also used. All electron tracks are fitted using a Gaussian-Sum Fitter [68] that corrects the bremsstrahlung energy loss. The electron energy is also corrected by the same η-dependent scaling factor derived from the data-MC comparison in $Z \to ee$ sample. The electron candidates are required to pass the electron identification selection. In addition to the shower shape variables, the electron identification also uses tracking information. The electron transverse momentum is computed from the cluster energy measured from the EM calorimeter and the track direction measured from the inner detector. More details of the electron reconstruction and its performance in data can be found in Ref. [60]

All electrons used in the analysis are required to have a transverse momentum $p_{T,e}$ greater than 15 GeV and a pseudo-rapidity η_e in the range of $|\eta_e| < 2.47$. The electrons are also required to pass normalized track and calorimeter isolation selections. The normalized calorimeter isolation is defined as $E_T^{cone40}/E_{T,e}$ where E_T^{cone40} is the sum of transverse energy in a cone with a size of $\Delta R = 0.4$ around the electron excluding the electron cluster energy and $E_{T,e}$ is the transverse energy of the electron. The normalized track isolation is defined as $p_T^{cone20}/E_{T,e}$ where p_T^{cone20} is the scalar sum of p_T of all tracks in a cone with a size of $\Delta R = 0.4$ around the electron except the electron track. The electron is required to have $E_T^{cone40}/E_{T,e} < 0.2$ and $p_T^{cone20}/E_{T,e} < 0.15$.

4.3.3 Muon definition

Muons are reconstructed as “combined muons” and “segmented muons”. The combined muons are those muons whose track reconstruction is based on a combination of two independent track measurements in the inner detector and muon spectrometer. A segmented muon is based on a track that is measured in the inner detector and whose extrapolation in the precision muon chambers matches straight track segments.

In this analysis, both combined muon and segmented muon are used. A muon track must have Pixel, SCT and TRT hits. The pseudo-rapidity of a muon η_μ is in the region of $\eta_\mu < 2.7$, and the transverse momentum of a muon $p_{T,\mu}$ is required to be greater than 10 GeV. A muon candidate is required to have a normalized calorimeter isolation $E_T^{cone40}/p_{T,\mu}$ less than 0.2 and a normalized track isolation $p_T^{cone20}/E_{T,\mu}$ less than 0.15, where the two normalized muon isolation variables are defined in the same way as the electron normalized isolation variables are defined.

4.3.4 Object overlap removal

Since the same detector signal can be reconstructed to multiple types of objects, an object overlap removal procedure is applied to make sure every detector signal only enters the analysis once. This overlap removal is performed in the following order:

- The two leading photons are always kept;
- Electrons with $\Delta R(e, \gamma) < 0.4$ are removed;
- Jets such as $\Delta R(jet, e) < 0.2$ or $\Delta R(jet, \gamma) < 0.4$ are removed
- Muons with $\Delta R(\mu, jet) < 0.4$ or $\Delta R(\mu, \gamma) < 0.4$ are removed

4.3.5 Missing transverse energy reconstruction

The missing transverse energy E_T^{miss} is reconstructed from the "visible" transverse energies of all objects, assuming the momentum conservation in the transverse plane. To calculate the E_T^{miss} in an event, all objects are first identified to photons, electrons, muons and jets; then the appropriate calibrations are applied to each type of objects. Each object has to be classified to one type of object without ambiguity and only enters the calculation once. For example, an EM cluster may be reconstructed as more than one objects, e.g., a photon and an electron. If such an EM cluster passes the photon identification requirement, then it will be only counted as a photon even if it can also pass the electron identification selection. The preference in object classification is to prefer photon to electron. The photon identification used to classify objects is made fully consistent with the photon identification used for this analysis. The reconstructed $x(y)$ component of the E_T^{miss} can be expressed as:

$$\begin{aligned} E_{x(y)}^{\text{miss}} = -(\sum E_{x(y)}^{\gamma} + \sum E_{x(y)}^{e} + \sum E_{x(y)}^{\tau} + \sum E_{x(y)}^{\mu} + \sum E_{x(y)}^{\text{jets}} \\ + \sum E_{x(y)}^{\text{soft jets}} + \sum E_{x(y)}^{\text{cell out}}) \end{aligned}$$

The E_T^{miss} determination is very sensitive to the pile-up condition, and the E_T^{miss} resolution degrades with the square root of the total energy in the calorimeter, $\sum E_T$. To more efficiently select events with genuine E_T^{miss}, E_T^{miss} significance variable is used as the discriminating variable in this analysis, which is defined as $E_T^{miss}/\sigma(E_T^{miss})$ where $\sigma(E_T^{miss}) = k \sum E_T$. The k value is 0.67 which is measured from the 2011 data. The k value is different in 2012 data, but it does not affect the analysis as the final optimized cut on the E_T^{miss} significance is tuned with this constant factor.

4.4 Diphoton event selection

4.4.1 Trigger

Diphoton triggers are implemented so that events of interest to this analysis can be efficiently collected. In the 2011 data taking, the diphoton trigger requires the presence of two photons with transverse energy greater than 20 GeV and at the event filter level the photon clusters that fire the trigger should meet the $loose$ photon identification criteria. In the 2012 data taking, the transverse energy threholds for the leading photon and subleading photon are raised to 35 GeV and 25 GeV, respectively, in order to cope with the increased instantaneous luminosity.

The trigger efficiency is estimated by a "bootstrap" method. In this method, the trigger efficiency is factorized to the efficiency of high level trigger selection relative to the Level-1 seed times the efficiency of Level-1 seeding. These efficiencies can be independently measured from a sample of minimum biased events [69]. The estimated diphoton trigger efficiency is $98.9 \pm 0.2\%$ for 7 TeV data and $99.6 \pm 0.1\%$ for 8 TeV data.

4.4.2 Event selection for the "search" analysis

The "search" analysis is based on 4.8 fb^{-1} data at $\sqrt{s} = 7$ TeV and the first 5.9 fb^{-1} data at $\sqrt{s} = 8$ TeV. The diphoton events used in the analysis must fire the diphoton trigger. The transverse energy of the leading photon should be greater than 40 GeV and the transverse energy of the subleading photon should be greater than 25 GeV. The photon pseudorapidity measured by the second layer of the EM calorimeter, η_{s2}, should be in the range of $|\eta_{s2}| < 1.37$ or $1.52 < |\eta_{s2}| < 2.37$. The leading and subleading photon candidates in the event must pass the *tight* identification criteria. In addition, the calorimeter isolation energy should be less than 4 GeV. The invariant mass of two photons should be between 100 GeV and 160 GeV. In total, 23788 events were selected from the $\sqrt{s} = 7$ TeV data and 35271 events were selected from the $\sqrt{s} = 8$ TeV data. The expected number of Higgs boson signal event at $m_H = 126.5$ GeV passing the same selection is approximately 79 for the $\sqrt{s} = 7$ TeV sampled and 112 for the $\sqrt{s} = 8$ TeV sample.

The composition of the selected diphoton sample is understood with several data driven background estimation methods [70, 71]. The fraction of genuine diphoton events is found to be $80\pm4\%$ in the $\sqrt{s} = 7$ TeV sample and $75^{+3}_{-2}\%$ in the $\sqrt{s} = 8$ TeV sample. The fraction of γ-jet background is found to be $19\pm3\%$ in the $\sqrt{s} = 7$ TeV sample and $22\pm2\%$ in the $\sqrt{s} = 8$ TeV sample. The fraction of multi-jets background is found to be $1.8 \pm 0.5\%$ in the $\sqrt{s} = 7$ TeV sample and $2.6 \pm 0.5\%$ in the $\sqrt{s} = 8$ TeV sample. Fig. 4.4.2 shows the composition of the selected diphoton sample in the $m_{\gamma\gamma}$ distribution for these two samples.

4.4.3 Event selection for the “measurement” analysis

The “measurement” analysis is based on the full dataset of the 2011 and 2012 runs, corresponding to 4.8 fb^{-1} data at $\sqrt{s} = 7$ TeV and 20.7 fb^{-1} data at $\sqrt{s} = 8$ TeV. Changes are only made for the selection of $\sqrt{s} = 8$ TeV events, and the $\sqrt{s} = 7$ TeV selection is not changed. Two changes are made with respect to the event selection used for the “search” analyis: First, the

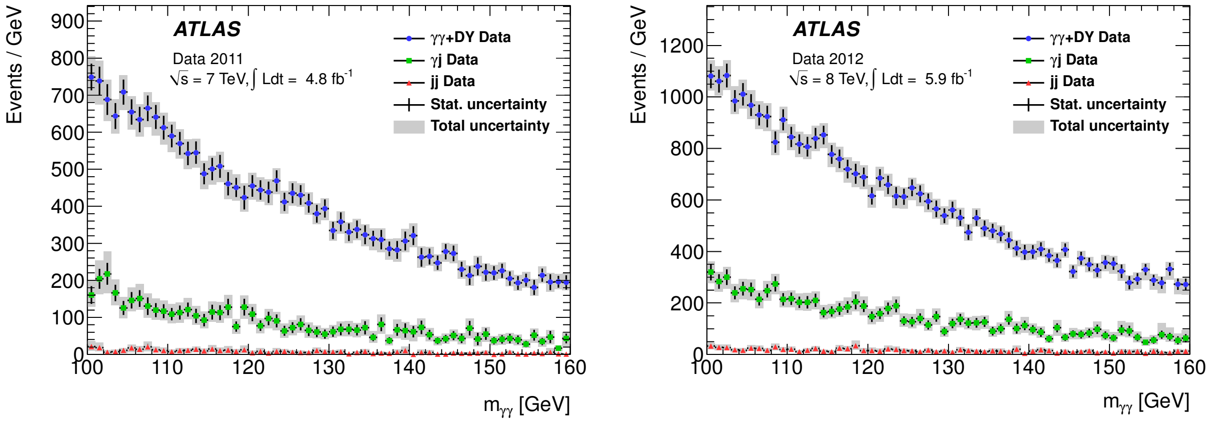

Figure 4.4 Diphoton sample composition as a function of the invariant mass for the $\sqrt{s} = 7$ TeV sample (left) and the $\sqrt{s} = 8$ TeV sample (right). The small contribution from Drell-Yan events is included in the diphoton component.

acceptable η_{s2} range is changed to $|\eta_{s2}| < 1.37$ or $1.56 < |\eta_{s2}| < 2.37$, due to the deteriorated performance of the photon identification in the $\sqrt{s} = 8$ TeV sample. Second, the E_T threshold for the subleading photon is increased to 30 GeV to enhance the sensitivity. In the 20.7 fb^{-1} 8 TeV data, 118893 events were selected, and the corresponding expected number of Higgs boson signal events at $m_H = 126.5$ GeV passing the same selection is approximately 395. The fraction of genuine diphoton events in the full $\sqrt{s} = 8$ TeV data sample is estimated by data driven methods and found to be $75^{+3}_{-4}\%$.

4.5 Monte Carlo samples

In ATLAS, events produced in the standard HepMC format from a generator are passed to a full detector simulation and reconstructed with the same software release used for data [72]. Pile-up effects are simulated by overlaying the MC event from the hard process with a variable number of

MC inelastic pp collisions. This variable number is generated from a Poisson distribution whose mean value is the mean number of interactions per bunch crossing. The Monte Carlo events are weighed to have the same distribution of mean number of interactions per bunch crossing of data.

4.5.1 Signal Monte Carlo samples

Signal Monte Carlo samples are generated at 11 hypothesized Higgs boson mass points between 100 GeV and 150 GeV in steps of 5 GeV. The gluon fusion and vector boson fusion signal processes are simulated by the POWHEG [73, 74] generator that is interfaced to PYTHIA [58] for showering and hadronization. The processes in which the Higgs boson is produced with a pair of top quarks or a vector bosons are simulated by PYTHIA.

4.5.2 Background Monte Carlo samples

In this analysis, background Monte Carlo samples are not directly used for deriving the expected background yield, and they are only used for analysis optimization and $m_{\gamma\gamma}$ modeling systematics studies.

The SM $\gamma\gamma$ events and γ-jet production are generated by Sherpa [75]. The SM γ-jet events are also generated by Alpgen [76, 77, 78] in 5 number-of-parton-bins. The multi-jet events are generated by Pythia. These generator-level events are also passed to a full detector simulation.

Chapter 5

Analysis for searching the Standard Model Higgs boson in the diphoton final state

This chapter presents the analysis designed to search for the Standard Model Higgs boson in the diphoton final state(i.e., the “search” analysis). Sec. 5.1 gives an overview of the general idea on how to search for a narrow resonance on top of a smooth background. Sec. 5.2 discusses the idea of event categorization and defines the categories. Sec. 5.3 discusses systematic uncertainties related to the analysis.

5.1 Overview

The primary goal of the analysis is to find or exclude a Higgs boson signal in the collected data sample. The discriminating variable that separates the signal and the background is the invariant mass of diphoton, $m_{\gamma\gamma}$, as the signal is a narrow resonance while the background $m_{\gamma\gamma}$ distribution is a smooth and falling continuum. These distributions can be modeled by Probability Density Functions (PDF). The signal and background normalizations in a data sample can be determined by fitting the linear combination of a signal PDF and background PDF to data. This is illustrated by Fig. 5.1. Those events in data that are away from the mass region of the signal largely serve the purposes of constraining the background shape and its normalization, and therefore the signal normalization can be simultaneously determined. In this analysis, the fit is always a maximum likelihood fitm, which means the variation of parameter values is driven by maximizing the log likelihood with the given data and PDF.

In order to maximize the search sensitivity, the diphoton sample is divided into multiple categories of events that have different signal to background ratios (S/B) and $m_{\gamma\gamma}$ resolutions. The improvement due to categorization can be understood from a simple example: consider a counting analysis where the expected number of signal event and the expected number of background events are s and b, respectively. Now, the sample is divided to two subsamples, and there are s_1 expected signal events and b_1 expected background events in one subsample and s_2 expected signal events and b_2 expected background events in the other subsample. The expected statistical significance combing these two subsamples is then:

$$Z_{comb} = \sqrt{(\frac{s_1}{\sqrt{b_1}})^2 + (\frac{s_2}{\sqrt{b_2}})^2} \tag{5.1}$$

and the difference between Z_{comb} and $Z_{inclusive} = s/\sqrt{b}$, the expected statistical significance without dividing the sample is:

$$\begin{aligned} Z_{comb} - Z_{inclusive} &= \sqrt{(\frac{s_1}{\sqrt{b_1}})^2 + (\frac{s_2}{\sqrt{b_2}})^2} - \frac{s_1 + s_2}{\sqrt{b_1 + b_2}} \\ &= \sqrt{b_1 b_2 \frac{(\frac{s_1}{b_1} - \frac{s_2}{b_2})^2}{b_1 + b_2}} \end{aligned}$$

The above result suggests that the analysis dividing the sample to two subsamples (the "category analysis") has a better sensitivity than the analysis without dividing the sample (the "inclusive analysis") as long as the two subsamples have different signal-to-background ratios. This conclusion can be easily generalized to the case where multiple categories are defined.

The categorization of events can be implemented with two approaches: one can divide the sample by placing cuts on a variable whose distribution is different between signal and background; alternatively, one can also group together events with the same topology related to a particular Higgs boson production mode. In the latter case, the sensitivity to Higgs boson signals from particular production modes is also enhanced. Both of these approaches are used in this analysis.

The observation from data will be interpreted statistically using hypothesis testing. The results of the statistical interpretation include the signal statistical significance and limit on the Higgs boson production cross section. The statistics methodology is to be discussed in detail in Chapter 6.

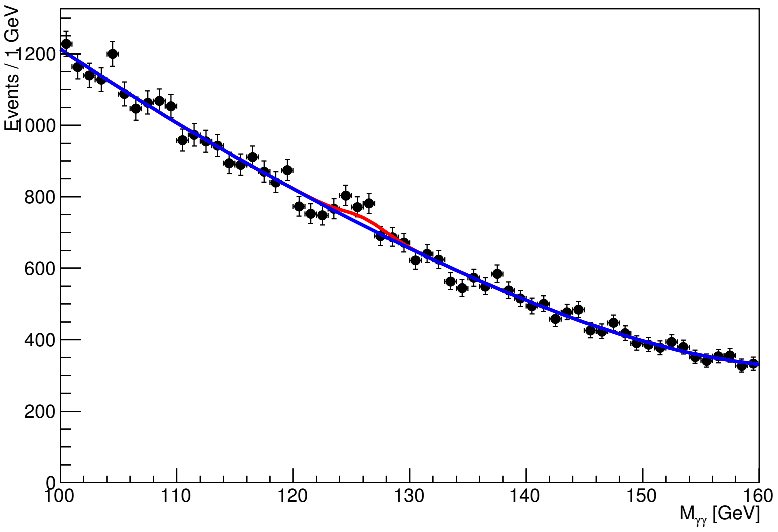

Figure 5.1 A dummy plot that illustrates the idea of using likelihood fit to determine the signal and background normalization. The blue curve is the fitted background PDF and the red curve is the fitted signal PDF. Both PDFs normalizations are determined in the fit by data.

5.2 Categorization strategy

As shown in Sec. 5.1, dividing the selected diphoton sample into multiple categories of events with different S/B can improve the analysis sensitivity. The most naive strategy to categorize the diphoton events is to identify a variable whose distribution is different between signal and background, and divide the sample by placing one or more cuts on the variable. This single variable-based categorization is discussed in Sec. 5.2.1. Based on the knowledge of the signal production modes, one can also categorize the diphoton events according to their event topologies and obtain categories — each of which is enriched in signal events from one particular production mode. This event topology-based categorization is discussed in Sec. 5.2.2.

5.2.1 Single variable categorization

The p_{Tt}, $|\eta|$ and conversion status of diphoton events are used to categorize the events. They are discussed below.

- p_{T_t} **of the diphoton system.** p_{T_t} is defined as the transverse component of the two photon transverse momentum with respect to the thrust axis of the two photon system as illustrated in Fig. 5.2. Explicitly, $p_{Tt} = |(\vec{p}_T^{\gamma 1} + \vec{p}_T^{\gamma 2}) \times \hat{t}|$, where $\hat{t} = (\vec{p}_T^{\gamma 1} - \vec{p}_T^{\gamma 2})/|\vec{p}_T^{\gamma 1} - \vec{p}_T^{\gamma 2}|$. The choice of p_{T_t} variable is motivated by the fact that p_{T_t} and p_T are strongly correlated and the Higgs boson p_T distribution is harder compared to the QCD backgrounds. The study of using Higgs boson p_T for the event categorization was reported in the Ref. [59]. However, it is found that the $m_{\gamma\gamma}$ distribution from the events with high p_T is not monotonically falling in the mass range between 100 GeV and 160 GeV, and this introduces complications in choosing background functions and also in the fit. This effect can be avoided by placing the cut on the p_{T_t} instead of p_T, as shown in Fig. 5.3 where the $m_{\gamma\gamma}$ distributions with various cuts on p_T or p_{T_t} from a background $\gamma\gamma$ MC sample are plotted. Fig. 5.4 shows p_{T_t} distributions for the major Higgs boson production modes and the Monte Carlo background. A large fraction of VH and VBF signal events are of high p_{T_t} as the $\gamma\gamma$ system in those events are boosted while the majority of background events are of low p_{T_t} . The ggF signal has a smaller fraction of events in the high p_{T_t} region, but it still has a larger p_{T_t} tail compared to the background.

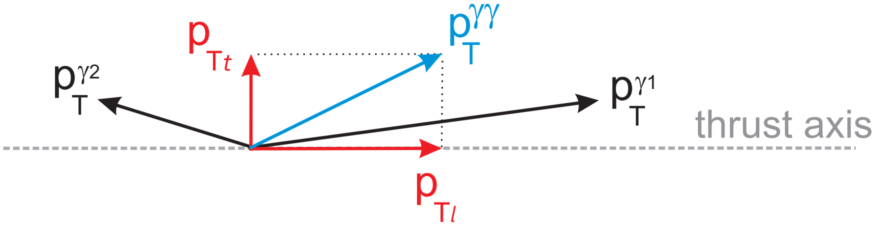

Figure 5.2 Sketch of the p_{T_t} definition.

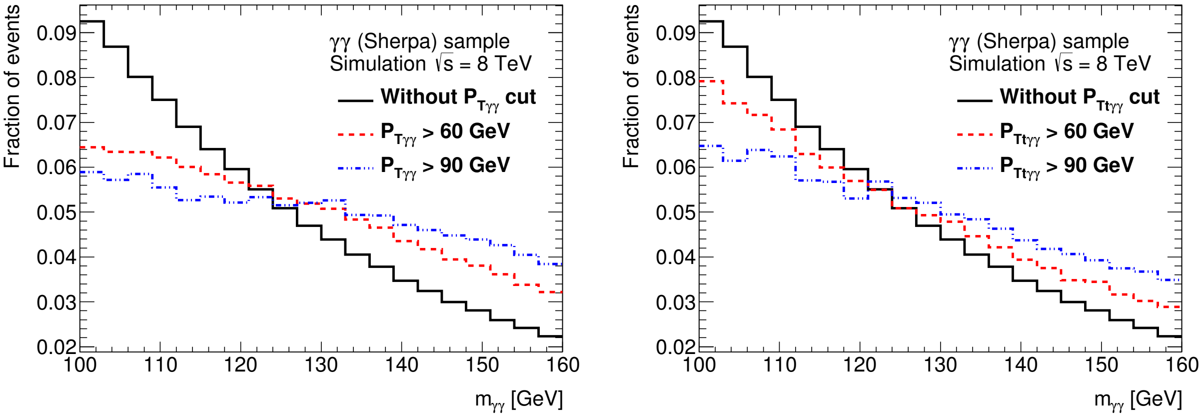

Figure 5.3 Effects of requiring a $p_{T\gamma\gamma}$ cut or a p_{T_t} cut on the $m_{\gamma\gamma}$ background shape. Left plot shows the $m_{\gamma\gamma}$ distributions without any $p_{T\gamma\gamma}$ cut, with $p_{T\gamma\gamma} > 60$ GeV, and with $p_{T\gamma\gamma} > 90$ GeV. Right plot shows the $m_{\gamma\gamma}$ distributions without any p_{T_t} cut, with $p_{T_t} > 60$ GeV, and with p_{T_t} > 90 GeV.

- **conversion status of the photon cadidates.** In the signal sample, about 50% of events has at least one converted photon candidate, while 66% of background events has at least one converted photon candidate. The difference in conversion fraction between signal and background is due to that the fake photons in the γ-jet background sample mostly come from π^0 decays which gives two photons and doubles the probability of having a converted

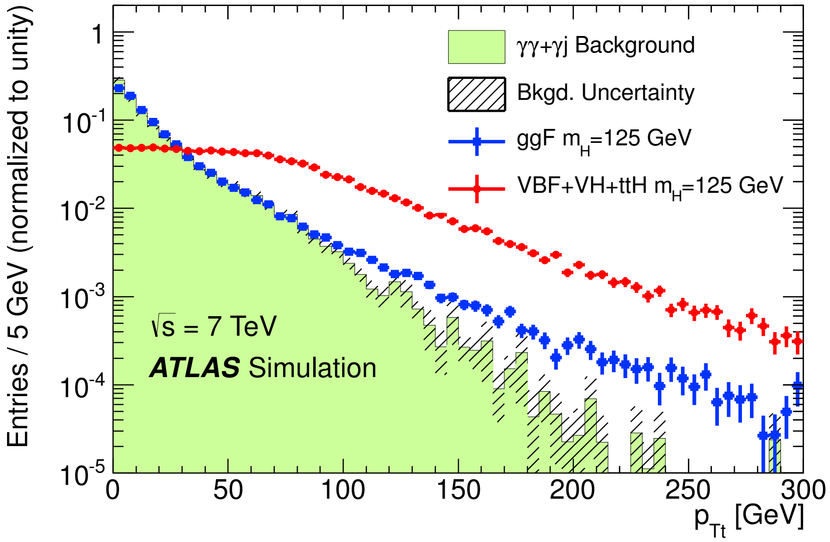

Figure 5.4 Distribution of p_{Tt} in simulated events with Higgs boson production and in background events. The signal distribution is shown separately for gluon fusion (blue), and vector-boson fusion together with associated production (red). The background MC samples are described in the publication. The background MC and the two signal distributions are normalised to unit area.

photon in the event. In addition, converted photons have a worse energy resolution compared to unconverted photons, and this is equivalent to having a worse S/B. For example, for a given mass window, e.g., ±2 GeV around the peak of signal, the background expectation is not sensitive to the resolution of $m_{\gamma\gamma}$, but the signal expectation is. The better the signal $m_{\gamma\gamma}$ resolution, the more signal events will fall in the mass window, improving the S/B.

- **η of the photon.** The η distribution of photons is different between signal and background. More importantly, photons in the very central region of the calorimeter have a better energy resolution compared to photons in the rest of the calorimeter. Therefore, the S/B is larger in the central η region.

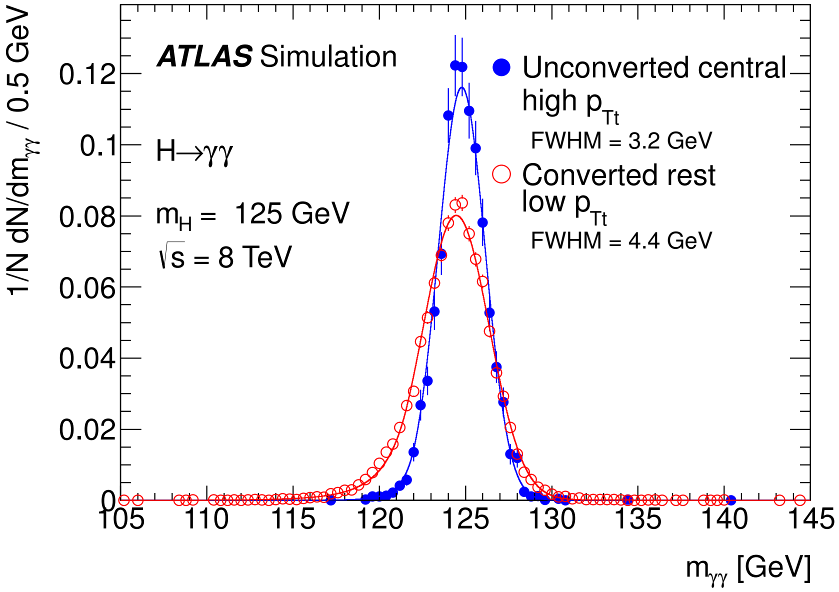

Figure 5.5 Invariant mass distributions for a Higgs boson with m_H = 125 GeV, for the best-resolution category (Unconverted central, high pTt) shown in blue and for a category with lower resolution (Converted rest, low pTt) shown in red, for the $\sqrt{s}$ = 8 TeV simulation. The invariant mass distribution is parametrized by the sum of a Crystal Ball function and a broad Gaussian, where the latter accounts for fewer than 12% of events in all categories (fewer than 4% in most categories).

Fig. 5.5 shows the $m_{\gamma\gamma}$ distribution for two categories of events. The category that has unconverted and central photons has a better resolution compared to the category that has converted and relatively forward photons.

5.2.2 Event topology-based categorization

Event topologies related to certain Higgs boson production modes can also be used to categorize diphoton events. For the “search” analysis, only the VBF event topology is considered. The event topologies related to various VH final states are considered for the “measurement” analysis and detailed in Chapter 8.

The two jets in the VBF Higgs boson signal events have some distinct characteristics compared to the jets in background events or ggF Higgs boson signal events. A few variables are considered for defining a VBF-enriched category. The first variable is the pseudo-rapidity difference between the two jets, $|\Delta\eta_{jj}|$. The VBF signal is expected to have two jets widely separated in pseudo-rapidity, and thus its $|\Delta\eta_{jj}|$ distribution tends to give a peak at a large value (see Fig. 5.6). The second variable considered is the invariant mass of the two jets, m_{jj}. The VBF signal events tend to have large m_{jj} compared to the SM background events and ggF signal events as shown in Fig. 5.7. The third variable considered is the difference in the azimuthal ϕ direction between the diphoton system and the dijet system, $\Delta\phi_{jj,\gamma\gamma}$. In the VBF signal events, the diphoton system and dijet system are expected to be more back-to-back, as shown in Fig. 5.8. What is common to Fig. 5.6, Fig. 5.7 and Fig. 5.8 is that the VBF distribution is not only different from the SM background distribution but also different from the ggF signal distribution. This indicates that cuts on theses variables will reject both background events and ggF signal events, thus improving the search sensitivity and the sensitivity to VBF production simultaneously.

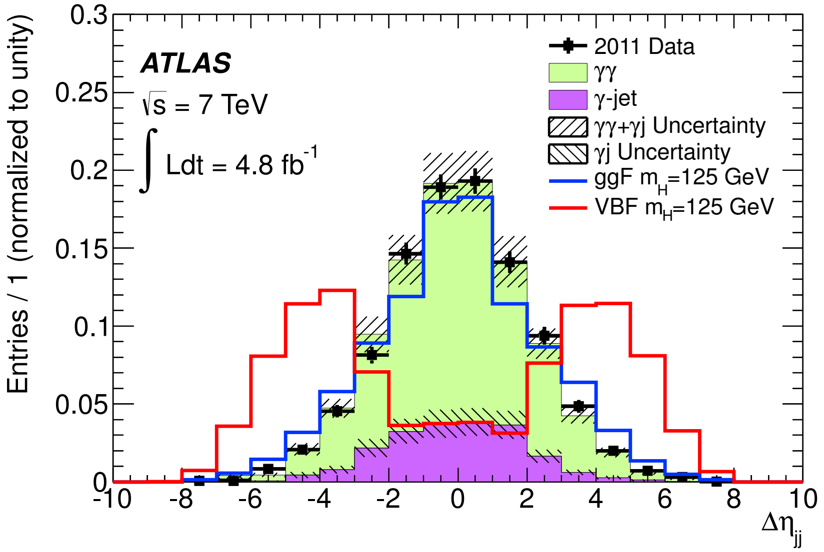

Figure 5.6 The $\Delta\eta_{jj}$ distributions for the VBF signal, ggF signal and SM background events from $\sqrt{s} = 7$ TeV Monte Carlo samples. The $\Delta\eta_{jj}$ distribution from $\sqrt{s} = 7$ TeV data sample is also shown.

Fig. 5.9 shows the distributions of a few other variables that also offer discriminating power. These variables include the number of jets in the event (jet multiplicity), the p_T of the leading jet, the p_T of the subleading jet, the η of the leading jet, and the η of the subleading jet. These variables shown in Fig. 5.9 are generally correlated with the three aforementioned variables and cannot improve the sensitivity in a significant way. Some of these variables, e.g., the η of leading jet or the η of subleading jet are used in the “measurement” analysis described in Chapter 8.

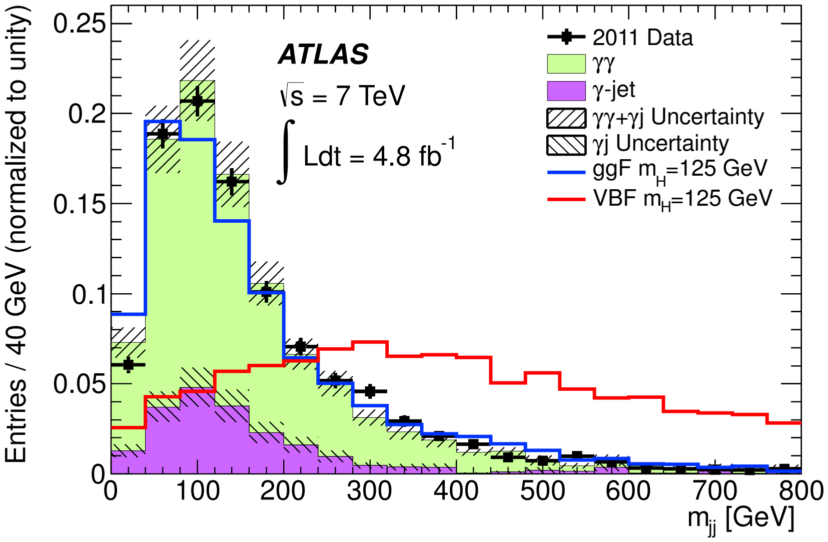

Figure 5.7 The m_{jj} distributions for the VBF signal, ggF signal and SM background events from $\sqrt{s} = 7$ TeV Monte Carlo samples. The m_{jj} distribution from $\sqrt{s} = 7$ TeV data sample is also shown.

5.2.3 Definition of categories

The categorization starts with taking out the diphoton events with two additional jets of VBF characteristics. Then, the rest of the sample is divided to nine categories according to the p_{T_t} , $|\eta|$ and conversion information of the diphoton events. The 2-jet category and nine p_{Tt}-η-conversion categories are implemented for $\sqrt{s} = 7$ TeV sample and $\sqrt{s} = 8$ TeV sample separately, resulting in 20 categories.

5.2.3.1 2-jet category

The 2-jet category is defined with the following requirements:

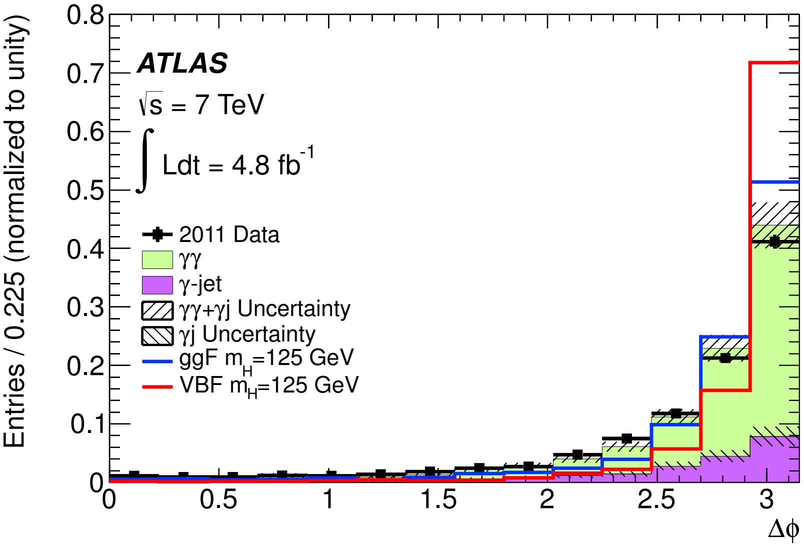

Figure 5.8 The $\Delta\phi_{jj,\gamma\gamma}$ distributions for the VBF signal, ggF signal and SM background events from $\sqrt{s} = 7$ TeV Monte Carlo samples. The $\Delta\phi_{jj,\gamma\gamma}$ distribution from $\sqrt{s} = 7$ TeV data sample is also shown.

- **the presence of at least two additional jets**
- **the invariant mass of the two jets,** m_{jj} should be greater than 500 GeV.
- **the pseudo-rapidity gap between the two jets,** $|\Delta\eta_{jj}|$ should be larger than 3.6.
- **the difference in the ϕ direction between the diphoton system and dijet system,** $\Delta\phi_{\gamma\gamma,jj}$ should be larger than 2.6.

5.2.3.2 p_{Tt}-η-conversion categories

The naming convention for the p_{Tt}-η-conversion categories are itemized below, and exact definitions of the nine categories are given in Table. 5.1.

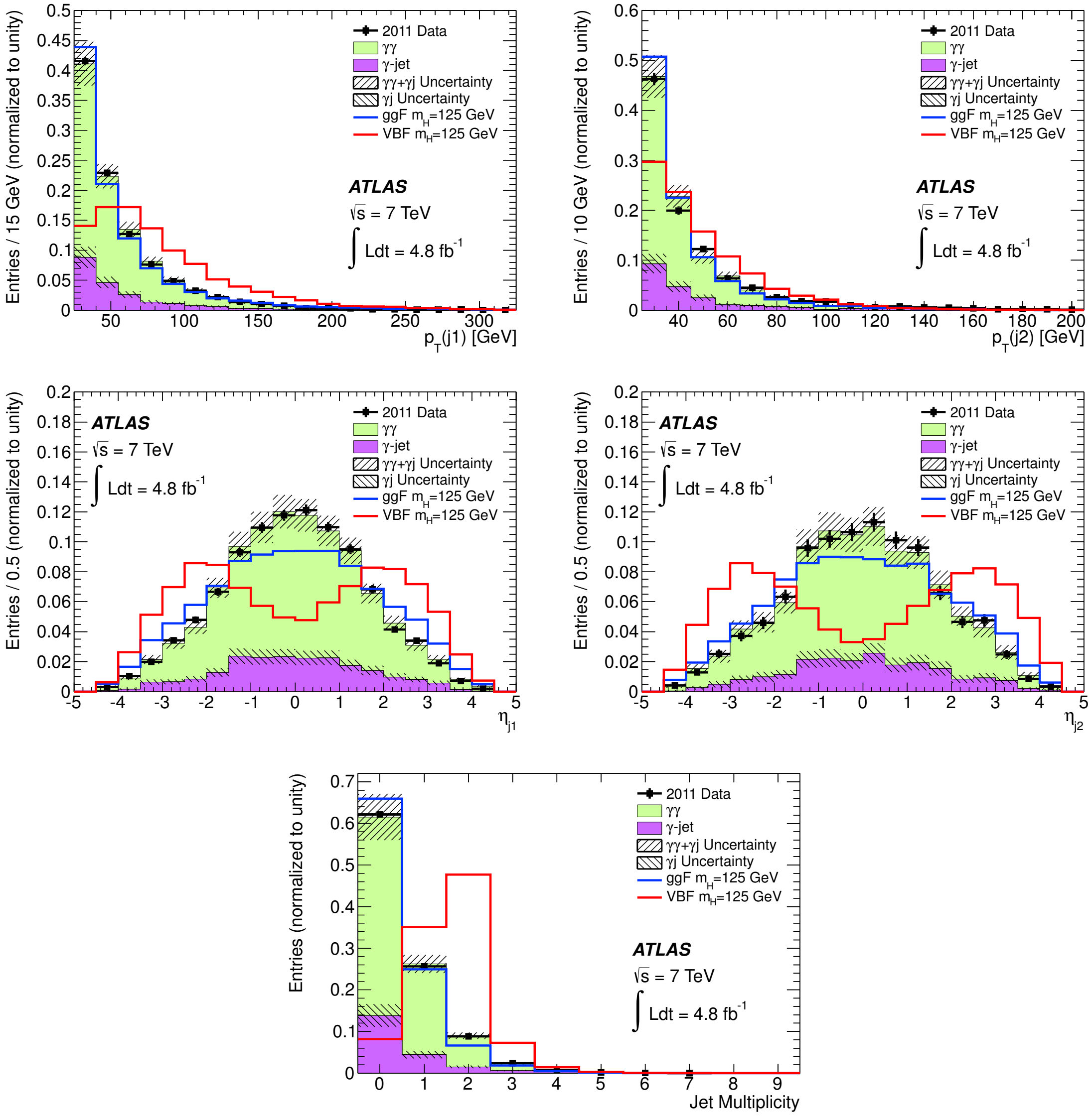

Figure 5.9 The $\Delta\phi_{jj,\gamma\gamma}$ distributions for the VBF signal, ggF signal and SM background events from $\sqrt{s} = 7$ TeV Monte Carlo samples. The $\Delta\phi_{jj,\gamma\gamma}$ distribution from $\sqrt{s} = 7$ TeV data sample is also shown.

- p_{T_t} **categorization.** The diphoton events with $p_{T_t} > 60$ GeV are classified as **High-**p_{T_t} events, while the diphoton events with $p_{T_t} \leq 60$ GeV are classified as **Low-**p_{T_t} events.

- **Conversion categorization.** The diphoton events with two unconverted photons are classified as **Unconverted** events, while the diphoton events with at least one converted photon are classified as **Converted** events.

- $|\eta|$ **categorization.** The diphoton events with both photons in the region of $|\eta| < 0.75$ are classifed as **Central** events. The **Unconverted** diphoton events with at least one photon in the region of $|\eta| \geq 0.75$ are classifed as **Unconverted Rest** events. The **Converted** diphoton events with at least one photon in the region of $1.35 \leq |\eta| \leq 1.75$ are classifed as **Converted Transition** events. The **Converted** diphoton events that are not classified as **Central** or **Converted Transition** events are classified as **Converted Rest** events.

5.2.4 Summary of category information

The signal mass resolution, number of observed events, number of expected signal events (N_S), number of expected background events (N_B), and signal to background ratio (N_S/N_B) in a mass window around $m_H = 126.5$ GeV (containing 90$\%$ of the expected signal events) in each category and the inclusive sample are shown in Table. 5.2. The the $m_{\gamma\gamma}$ resolution from the "inclusive" sample is $\sim$ 1.74 - 1.77 GeV. Between categories, the Unconverted Central High p_{T_t} categories have the best resolution, ~ 1.40 GeV, and Converted Transition categories have the worst resolution, $\sim 2.27 - 2.57$ GeV. The signal to background ratio is about 3% in the inclusive samples, and it varies between 0.01 and 0.22 in the $\sqrt{s} = 7$ TeV categories and between 0.01 and 0.57 in the

Table 5.1 Exact definitions of the nine p_{T_t} -η-conversion categories. In the table, γ_u and γ_c stand for unconverted photon and converted photon, respectively; η without a subscript indicates the requirement is for both photons; η_{γ_i} indicates the requirement is for γ_i ; $\exists\gamma_i$ means that there exists at least one photon and this photon is labeled as γ_i.

Category	Conversion status	η	p_{T_t}
Unconverted Central Low p_{T_t}	$\gamma_u\gamma_u$	$\lvert\eta\rvert \leq 0.75$	≤ 60 GeV
Unconverted Central High p_{T_t}	$\gamma_u\gamma_u$	$\lvert\eta\rvert \leq 0.75$	> 60 GeV
Unconverted Rest Low p_{T_t}	$\gamma_u\gamma_u$	$\exists\gamma_i, \lvert\eta_{\gamma_i}\rvert > 0.75$	≤ 60 GeV
Unconverted Rest High p_{T_t}	$\gamma_u\gamma_u$	$\exists\gamma_i, \lvert\eta_{\gamma_i}\rvert > 0.75$	> 60 GeV
Converted Central Low p_{T_t}	$\gamma_u\gamma_c$ or $\gamma_c\gamma_c$	$\lvert\eta\rvert \leq 0.75$	≤ 60 GeV
Converted Central High p_{T_t}	$\gamma_u\gamma_c$ or $\gamma_c\gamma_c$	$\lvert\eta\rvert \leq 0.75$	> 60 GeV
Converted Rest Low p_{T_t}	$\gamma_u\gamma_c$ or $\gamma_c\gamma_c$	$\exists\gamma_i, \lvert\eta_{\gamma_i}\rvert > 0.75$ $\lvert\eta_{\gamma_i}\rvert < 1.35$ or $\lvert\eta_{\gamma_i}\rvert > 1.75$ $\lvert\eta_{\gamma_j}\rvert < 1.35$ or $\lvert\eta_{\gamma_j}\rvert > 1.75$	≤ 60 GeV
Converted Rest High p_{T_t}	$\gamma_u\gamma_c$ or $\gamma_c\gamma_c$	$\exists\gamma_i, \lvert\eta_{\gamma_i}\rvert > 0.75$ $\lvert\eta_{\gamma_i}\rvert < 1.35$ or $\lvert\eta_{\gamma_i}\rvert > 1.75$ $\lvert\eta_{\gamma_j}\rvert < 1.35$ or $\lvert\eta_{\gamma_j}\rvert > 1.75$	> 60 GeV
Converted Transition	$\gamma_u\gamma_c$ or $\gamma_c\gamma_c$	$\exists\gamma_i, 1.35 < \lvert\eta_{\gamma_i}\rvert < 1.75$	No requirement

$\sqrt{s} = 8$ TeV categories. The Converted Transition categories have the worst S/B, and the 2-jet categories have the best S/B.

The expected number of signal events normalized to the integrated luminosity and the fraction of each production mode in each category are shown in Table 5.3 for the $\sqrt{s} = 7$ TeV sample and in Table 5.4 for the $\sqrt{s} = 8$ TeV sample. In the inclusive sample, the ggF signal events make up about 88% of all signal events. The ggF is also the dominant signal component in all nine p_{T_t} -η-conversion categories. The 2-jet categories are defined to select a VBF-enriched sample, and

Table 5.2 Number of expected signal S for $m_H = 126.5$ GeV and background events B in a mass window around $m_H = 126.5$ GeV that would contain 90% of the expected signal events, along with the observed number of events in this window. In addition, σ_{CB}, the Gaussian width of the Crystal Ball function (The signal parameterization is detailed in Sec. 6.1.1) describing the invariant mass distribution, and the full width at half maximum (FWHM) of the distribution, are given. The numbers are given for the data and simulation at $\sqrt{s} = 7$ TeV (top) and 8 TeV (bottom) for different categories and the inclusive sample.

$\sqrt{s}$			7 TeV			
Category	σ_{CB} (GeV)	FWHM (GeV)	Observed	N_S	N_B	N_S/N_B
Unconv. central, low p_{T_t}	1.45	3.41	161	9.4	154.9	0.061
Unconv. central, high p_{T_t}	1.37	3.22	7	1.3	7.2	0.181
Unconv. rest, low p_{T_t}	1.57	3.71	700	19.5	669.7	0.029
Unconv. rest, high p_{T_t}	1.43	3.36	57	2.5	37.7	0.066
Conv. central, low p_{T_t}	1.63	3.84	166	6	136.4	0.044
Conv. central, high p_{T_t}	1.48	3.48	2	0.9	6.4	0.141
Conv. rest, low p_{T_t}	1.79	4.23	986	18.9	967.3	0.02
Conv. rest, high p_{T_t}	1.61	3.8	48	2.5	51.2	0.049
Conv. transition	2.27	5.52	709	8.5	703.9	0.012
2-jet	1.52	3.59	12	2	8.7	0.23
Inclusive	1.63	3.84	2653	71.5	2557.6	0.028

$\sqrt{s}$			8 TeV			
Category	$\sigma_{CB}(\,GeV)$	Observed	N_S	N_B	N_S/N_B	
Unconv. central, low p_{T_t}	1.46	3.44	237	12.7	224.7	0.057
Unconv. central, high p_{T_t}	1.37	3.24	16	2.3	13.6	0.169
Unconv. rest, low p_{T_t}	1.58	3.73	1141	27.8	1122.5	0.025
Unconv. rest, high p_{T_t}	1.52	3.57	75	4.7	68.3	0.069
Conv. central, low p_{T_t}	1.64	3.86	207	8	186.6	0.043
Conv. central, high p_{T_t}	1.5	3.53	13	1.5	9.7	0.155
Conv. rest, low p_{T_t}	1.89	4.45	1311	24.2	1299.9	0.019
Conv. rest, high p_{T_t}	1.65	3.9	71	4	71.3	0.056
Conv. transition	2.59	6.1	849	11.5	821.2	0.014
2-jet	1.59	3.74	19	2.7	13.3	0.203
Inclusive	1.64	3.88	3649	100.7	3584.8	0.028

the VBF signal fraction is about 77% in the $\sqrt{s} = 7$ TeV 2-jet category and about 68% in the $\sqrt{s} = 8$ TeV 2-jet category. The 2-jet category definition is optimized with $\sqrt{s} = 7$ TeV samples and is not fully optimal for the $\sqrt{s} = 8$ TeV sample, leading to a lower fraction of VBF signal in the $\sqrt{s} = 8$ TeV 2-jet category compared to its counterpart at $\sqrt{s} = 7$ TeV. For other categories, ggF signal constitutes $\sim 90\%$ of the total signal events in the low p_{T_t} categories and $\sim 70\%$ of the total signal events in the high p_{T_t} categories. The VBF and VH signal fractions are enhanced in the high p_{T_t} categories, where VH and VBF each constitutes $\sim 15\%$ of the signal events. This pattern is due to the fact that the VH and VBF signals are more boosted compared to the ggF signal as shown in Fig. 5.4.

Table 5.3 Number of expected signal events per category at $m_H = 126.5$, at $\sqrt{s} = 7$ and the breakdown by production process.

Category	Events	ggF [%]	VBF [%]	WH [%]	ZH [%]	ttH [%]
Inclusive	79.3	87.8	7.3	2.9	1.6	0.4
Unconverted central, low p_{Tt}	10.4	92.9	4.0	1.8	1.0	0.2
Unconverted central, high p_{Tt}	1.5	66.5	15.7	9.9	5.7	2.4
Unconverted rest, low p_{Tt}	21.6	92.8	3.9	2	1.1	0.2
Unconverted rest, high p_{Tt}	2.7	65.4	16.1	10.8	6.1	1.8
Converted central, low p_{Tt}	6.7	92.8	4.0	1.9	1.0	0.2
Converted central, high p_{Tt}	1.0	66.6	15.3	10	5.7	2.5
Converted rest, low p_{Tt}	21.0	92.8	3.8	2.0	1.1	0.2
Converted rest, high p_{Tt}	2.7	65.3	16.0	11.0	5.9	1.8
Converted transition	9.5	89.4	5.2	3.3	1.7	0.3
2-jets	2.2	22.5	76.7	0.4	0.2	0.1

Table 5.4 Number of expected signal events per category at $m_H = 126.5$, at $\sqrt{s} = 8$ and the breakdown by production process.

Category	Events	ggF [%]	VBF [%]	WH [%]	ZH [%]	ttH [%]
Inclusive	111.6	88.5	7.4	2.7	1.6	0.5
Unconverted central, low p_{Tt}	14.4	92.9	4.2	1.7	1.0	0.2
Unconverted central, high p_{Tt}	2.5	72.5	14.1	6.9	4.2	2.3
Unconverted rest, low p_{Tt}	31.4	92.5	4.1	2.0	1.1	0.2
Unconverted rest, high p_{Tt}	5.3	72.1	13.8	7.8	4.6	1.7
Converted central, low p_{Tt}	9.1	92.8	4.3	1.7	1.0	0.3
Converted central, high p_{Tt}	1.6	72.7	13.7	7.1	4.1	2.3
Converted rest, low p_{Tt}	27.3	92.5	4.2	2.0	1.1	0.2
Converted rest, high p_{Tt}	4.6	70.8	14.4	8.3	4.7	1.7
Converted transition	13.0	88.8	6.0	3.1	1.8	0.4
2-jets	2.9	30.4	68.4	0.4	0.2	0.2

5.3 Systematic uncertainties

The systematic uncertainties are discussed in two parts. The first part is about those systematic uncertainties that affect the signal yields, and the second part is about those systematic uncertainties that affect the modeling of signal and background $m_{\gamma\gamma}$ distributions.

5.3.1 Yield uncertainties

The signal yield uncertainties can be further classified to various types according to the source (theoretical or experimental) or how it affects the expected signal yield of the analysis. The latter is more helpful in understanding the systematic effect on the analysis and the discussion below follows this classification. Some of the yield uncertainties concern the signal normalization or signal selection efficiency, while other yield uncertainties concern how the signal events are distributed between categories. For the latter one, it is named as the "migration" uncertainty within ATLAS, although no individual event physically migrates between categories. The effect of this type of uncertainty is simply to cause correlated variations of $expected$ event yields in different categories.

For those uncertainties that are evaluated in the context of the $H \rightarrow \gamma\gamma$ analysis, the source of the uncertainty and the estimation method are discussed below. For those uncertainties that are common experiment-wide or are provided by the theoretical community, the values of those uncertainties are quoted and the references are given.

Luminosity uncertainty. The measurement of luminosity and its uncertainty for the ATLAS experiment is reported in Ref. [79]. The luminosity uncertainty is found to be 1.8% for the 2011 data, and 3.6% for the 2012 data.

Pile up uncertainty. A very conservative approach to evaluate the impact of potential mis-modeling of pile-up is taken: the $\sqrt{s}$ = 7 TeV (8 TeV) sample is divided to two subsamples, one with the average number of interactions less than 10 (18), and the other one with the average number of interactions greater than or equal to 10 (18). 10 (18) is approximately the mean value of the average number of interactions per bunch crossing distribution for the $\sqrt{s}$ = 7 TeV ($\sqrt{s}$ = 8 TeV) sample. Both subsamples are normalized to the same integrated luminosity used for this analysis, and the difference in the expected yield between these two subsamples is taken as the uncertainty on the signal yields due to mis-modeling of pile-up. This uncertainty is found to be $\sim$ 4%.

Photon selection uncertainty. The two dominant uncertainties related to the photon selection are the photon identification uncertainty and the photon isolation uncertainty. Due to the similarity in calorimeter showers between photons and electrons, a sample of $Z \to ee$ events selected from data has been used as a control sample to estimate various uncertainties. Estimating systematic uncertainty from such a data control sample has the advantage of incorporating some realistic detector effects that may not be well simulated in the Monte Carlo samples. However, additional systematic uncertainties have to be assigned to cover the difference in shower behavior between photons and electrons. The radiative photons from $Z \to ll\gamma$ data control sample are also used, but these photons are mostly of low p_T and cannot completely replace $Z \to ee$ events in the estimation of systematic uncertainty.

The electron shower shape variables are validated in a $Z \to ee$ data control sample, and the difference between data and Monte Carlo is extrapolated to the photon shower shape variables. The expected photon identification efficiency from the electron extrapolated data sample is compared to the photon identification efficiency in the Monte Carlo sample, and the difference is taken as the uncertainty. A $Z \to ll\gamma$ sample is also used to estimate the identification efficiency of the photons with lower p_T and its systematic uncertainty. It is found that the photon identification uncertainty is about 8% per event for the $\sqrt{s} = 7$ TeV data, and about 10% for the $\sqrt{s} = 8$ TeV data. The uncertainties between the two years' samples are considered to be fully correlated.

The $Z \to ee$ samples from data and Monte Carlo also serve as control samples for estimating the photon isolation selection efficiency. Electrons in these control samples are required to pass the same kinematic cuts used for photons. The calorimeter isolation variable for electrons are defined in the same way as they are defined for photons. The electron isolation selection efficiency in the $Z \to ee$ data sample is calculated and compared to its counterpart in the Monte Carlo sample. The difference in the electron isolation selection efficiency between the data control sample and the Monte Carlo sample is taken as the uncertainty on the photon isolation selection efficiency, and this uncertainty is found to be about 1% per event.

The diphoton trigger efficiency uncertainty is estimated using a boot-strap method and found to be 0.5% per event.

The photon energy scale uncertainty also introduces an uncertainty of about 0.1% per event.

Cross section and branching ratio uncertainty. The uncertainties of Higgs boson production cross sections are mainly related to the choice of QCD scales and the choice of parton distribution functions. Refs [27, 80] provide detailed studies of these uncertainties. In general, these uncertainty are estimated by varying the choice of the QCD scale or the choice of parton distribution function set and taking the maximum variation in cross section as the uncertainty. The parton distribution fucntion sets of CTEQ [81], MSTW [82] and NNPDF [83] are used for the calculation. Uncertainties provided by Ref [27] are used for this analysis, and all other SM Higgs boson analyses in both the ATLAS and CMS collaborations. The introduction of 2-jet category leads to additional uncertainties for the ggF process in the particular phase space relevant to the 2-jet category, and this is discussed in Sec. 5.3.1.1. The branching ratio uncertainty is estimated in a similar way as the cross section uncertainty and found to be about 5% [84].

5.3.1.1 "Migration" uncertainty

There is a group of uncertainties that affects the distributions of the variables defining the categories. The effect of such uncertainty is to introduce multiple correlated uncertainties in event yield between categories. For example, if the p_{T_t} shape suffers from an uncertainty, then a one sigma variation of this uncertainty may lead to an upward variation in the event yields of low p_{T_t} categories and a downward variation in the event yields of high p_{T_t} categories. These uncertainties in the low and high p_{T_t} categories are of the same source and fully correlated.

Such kind of uncertainties considered in this analysis include:

The Higgs boson p_T uncertainty. The choice of QCD scales and parton distribution function sets can lead to variations in the shape of Higgs boson p_T, which is strongly correlated to the p_{T_t} variable used for categorization in the analysis. The variation of QCD scale choice and parton distribution function set is done with the HqT package [85, 86, 87, 88]. One sigma variation of this uncertainty can lead to 1.1% upward event yield variation in the low p_{T_t} categories, and 12.5% downward event yield variation in the high p_{T_t} categories.

Theoretical uncertainty in the jet binning. The QCD scale uncertainty on the ggF signal yield is amplified in the particular phase space where the presence of at least 2 jets is required. The procedure of estimating this uncertainty is documented in Ref. [89]. The QCD scale variation is done for the ggF signal sample with 2 jets requirement added. The resulting new uncertainty is $\sim$ 25% on the ggF signal yield in the 2-jets category [90]. The impact on the event yields in other categories is neglected.

Conversion uncertainty The imperfect knowledge of the amount of material upstream of the EM calorimeter can lead to a mis-modeling of the photon conversion and the conversion rate. To estimate this uncertainty, the event yields from the Monte Carlo sample with a nominal amount of material, Monte Carlo samples with additional 5% and 10% materials are compared in each category. The largest variation in the signal yield is taken as the uncertainty, and it is found that one sigma variation of this uncertainty would lead to a 4% upward signal yield variation in the unconverted categories and a 3.5% downward signal yield variation in the converted categories.

Jet energy scale and resolution. The uncertainties on the jet energy scale are evaluated by varying the scale corrections within their respective uncertainties [67]. The jet energy scale uncertainties have major impacts on the signal yields in the 2-jet categories. The total uncertainty on the jet energy scale is found to be 19% for the 2-jet categories, and up to 4% for other categories. The effect due to the jet energy resolution uncertainty is found to be negligible.

Underlying event uncertainty. The uncertainty due to the modeling of underlying event is checked by comparing the signal yield from the default Monte Carlo sample with underlying event tune AUET2B and the signal yield from the Monte Carlo sample with Perugia2011 tune [91]. A one sigma variation of the underlying event uncertainty would lead to a 30% upward signal yield variation for the ggF, VH and ttH process in the 2-jet categories, and a 6% upward signal yield variation for the VBF process in the 2-jet categories.

Jet-vertex-fraction uncertainty. The jet-vertex-fraction efficiencies in the Z + 2 jets data and MC samples are compared, and the difference is considered as the systematic uncertainty. This leads to a 13% uncertainty on the 2-jet category signal yield.

5.3.2 $m_{\gamma\gamma}$ modeling uncertainty

The analysis uses analytic PDFs to model both the signal and background $m_{\gamma\gamma}$ distributions in the 20 categories. The uncertainty on the $m_{\gamma\gamma}$ modeling is discussed below.

5.3.2.1 Signal modeling uncertainties

The signal $m_{\gamma\gamma}$ distribution is modeled from Monte Carlo samples. The signal Monte Carlo samples went through a full detector simulation, and corrections obtained from data and MC comparison in $Z \rightarrow ee$ data are applied. Signal PDF parameters are fixed to the values determined from Monte Carlo samples. The main uncertainties in the signal modeling are related to the photon energy calibration. The uncertainty of photon energy resolution leads to an uncertainty on the width of the CB function, and the uncertainty of photon energy scale leads to an uncertainty on the mean of the CB function.

The following sources are considered for the $m_{\gamma\gamma}$ resolution uncertainty. First, the uncertainties on the constant term and the sampling term of the photon energy calibration are estimated from $Z \to ee$ sample, amounting to an uncertainty of $\pm 12\%$ relative to the nominal value of the $m_{\gamma\gamma}$ resolution. Second, the application of the electron energy scaling factor to photons is associated with an electron-to-photon extrapolation uncertainty. This is because material in front of the calorimeter affect the electrons and photons differently. From Monte Carlo study, this uncertainty is found to be $\sim 6\%$ of the nominal $m_{\gamma\gamma}$ resolution. Third, the photon energy measurement can be affected by pile-up contribution. This effect is estimated by checking random EM cluster energy in randomly triggered bunch crossings and found to be less than 3%. Fourth, the uncertainty coming from photon direction measurement is estimated with $Z \to ee$ sample where the primary vertex is selected by using electron shower information in the calorimeter, and this uncertainty is found to be negligible. The total relative uncertainty on the $m_{\gamma\gamma}$ resolution is therefore 14%. This is directly translated to 14% uncertainty on the width parameter of the CB function. The $m_{\gamma\gamma}$ resolution uncertainty is considered as having uniform size and being fully correlated between categories.

The photon energy scale uncertainty is also related to the fact that the electron calibration is applied to photons, and there are slight but crucial differences between photons and electrons. The following sources are considered for the photon energy scale uncertainty.

- **Material uncertainty.** Compared to electrons, photons deposit less energy in the material upstream of the EM calorimeter. The energy loss due to material effects is smaller for photons, and therefore the energy scaling factor derived from $Z \to ee$ sample overcorrects the photon energy. This overcorrection is a component of the photon energy scale uncertainty and its size is estimated from Monte Carlo samples.

- **Presampler uncertainty.** Compared to electrons, the photon showers start “late”, and a smaller fraction of its energy is deposited in the presampler. This also leads to an overcorrection when the energy scaling factor derived from $Z \to ee$ sample is applied to photons. This overcorrection is also treated as one component of the photon energy scale uncertainty.

- **Calibration method uncertainty.** There are also various small uncertainties related to the $in\ situ$ calibration method that is shared by electrons and photons. This component of photon energy scale uncertainty is correlated between electrons and photons.

The above energy scale uncertainties are estimated and translated to the $m_{\gamma\gamma}$ mass scale uncertainty for each category of diphoton events. To correctly take into account the η-dependent correlation of these uncertainties, the material uncertainty is broken up to a low $|\eta|$ ($|\eta| < 1.8$) component and a high $|\eta|$ ($|\eta| \geq 1.8$) component. The presampler uncertainty is broken up to a barrel component and an endcap component. The size of these uncertainties relative to the signal $m_{\gamma\gamma}$ peak position in each category, is shown in Table 5.5

Table 5.5 Peak position shift due to energy scale uncertainties in different categories

Category	Method	Material low $\|\eta\|$ ($\|\eta\| < 1.8$)	Material high $\|\eta\|$ ($\|\eta\| > 1.8$)	Presampler Barrel	Presampler End-Cap
Unconverted Central Low p_{T_t}	$\pm 0.30\%$	$\pm 0.30\%$	-	$\pm 0.10\%$	-
Unconverted Central High p_{T_t}	$\pm 0.30\%$	$\pm 0.30\%$	-	$\pm 0.10\%$	-
Unconverted Rest Low p_{T_t}	$\pm 0.30\%$	$\pm 0.50\%$	$\pm 0.10\%$	$\pm 0.20\%$	-
Unconverted Rest High p_{T_t}	$\pm 0.30\%$	$\pm 0.50\%$	$\pm 0.10\%$	$\pm 0.30\%$	-
Converted Central Low p_{T_t}	$\pm 0.30\%$	$\pm 0.10\%$	-	-	-
Converted Central High p_{T_t}	$\pm 0.30\%$	$\pm 0.10\%$	-	-	-
Converted Rest Low p_{T_t}	$\pm 0.30\%$	$\pm 0.20\%$	$\pm 0.10\%$	$\pm 0.10\%$	-
Converted Rest High p_{T_t}	$\pm 0.30\%$	$\pm 0.20\%$	$\pm 0.10\%$	$\pm 0.10\%$	-
Converted Transition	$\pm 0.40\%$	$\pm 0.60\%$	-	-	$\pm 0.10\%$
2-jets	$\pm 0.30\%$	$\pm 0.30\%$	-	$\pm 0.10\%$	-

The choice of background function may potentially lead to a shift in the signal $m_{\gamma\gamma}$ peak position. This is considered as a diphoton mass scale uncertainty in the "measurement" analysis.

5.3.2.2 Background modeling uncertainty

The background $m_{\gamma\gamma}$ distribution is modeled by an analytic PDF whose parameters are determined in a fit to data. The background shape parameters are left free because they cannot be predicted from Monte Carlo samples as accurately as the signal shape parameters. The signal shape is mostly decided by the detector performance, which is relatively well understood. The shape of background is dependent on the calculation of differential cross sections of major background processes, the modeling of jet fragmentation, the modeling of fake photon showers in the EM calorimeter, and the energy calibration. Given all these complications, the background shape parameters are best determined by data. These free shape parameters introduce a larger statistical uncertainty on the background shape and normalization, while reducing the systematic uncertainty on the background modeling.

This implementation, however, cannot cover the uncertainty due to the choice of the background function, which can be intrinsically different from the true background shape. In this case, the fit of the function to the background distribution cannot be perfect, and a $m_{\gamma\gamma}$-dependent residual, defined as the difference between the fitted background yield and the true background yield in a mass window containing and centering at $m_{\gamma\gamma}$, can be observed. In the analysis, a signal-plus-background fit is performed to determine the normalization of the signal component, and this residual is also fitted by the signal PDF and contributes to the signal normalization. Such contribution is a bias in the fitted signal normalization. If this is a positive bias, it can appear as a "spurious" signal. If this is a negative bias, it can lead to an aggressive limit.

In this analysis, all the selected background functions should pass the "spurious" signal test. This test is defined as follows: The analysis categorization is applied to a Monte Carlo sample that is normalized to the integrated luminosity used for the analysis, and the individual category background $m_{\gamma\gamma}$ distributions are used to test the background function candidates. In each category, a series of signal-plus-background fits are performed on the smeared MC distribution over the range of 110 GeV $\leq m_H \leq$ 150 GeV for each background candidate. These fits give a series of fitted number of signal events over m_H. If the Monte Carlo sample could accurately describe the real background distribution in data, then this series of fitted signal numbers would be used to correct the fitted number of signal events at each m_H. Since the Monte Carlo only serves to provide a sample that is reasonably similar to the real background shape, these fitted signal numbers cannot be considered as corrections. Instead, the largest fitted number of signal events, $n_{spr,max}$, of the series of fitted signal numbers is considered as the largest possible bias introduced by the choice of background function in the entire range of 110 GeV $\leq m_H \leq$ 150 GeV.

A quantitative requirement on the background function candidate is defined using $n_{spr,max}$ of a candidate background function. This requirement accepts a background function candidate if its $n_{spr,max}$ satisfies one of the two criteria below:

- $n_{spr,max}$ is smaller than 20% of the background statistical uncertainty at the m_H where the $n_{spr,max}$ is found.
- $n_{spr,max}$ is smaller than 10% of the expected number of signal events at the m_H where the $n_{spr,max}$ is found.

The purpose of defining such criteria is to make sure that the largest possible bias introduced by an acceptable background function is small enough so that the analysis is not affected by such a bias.

These criteria connect to the analysis sensitivity through involving the background statistical uncertainty and signal expectation in the definition. In the case of $H \rightarrow \gamma\gamma$ analysis, the statistical significance can be approximated by:

$$Z \sim \frac{S}{\sqrt{B}} \tag{5.2}$$

where S and B represent the fitted number of signal events and the fitted number of background events, respectively, and $\sqrt{B}$ is approximately the statistical uncertainty of the background. In the case that the fitted number of signal events is varied by 20% of the background statistical uncertainty, one has

$$Z \sim \frac{S \pm 0.2\sqrt{B}}{\sqrt{B}} = \frac{S}{\sqrt{B}} \pm 0.2. \tag{5.3}$$

The observed statistical significance can be affected by 0.2 σ.

In the case that the fitted number of signal events is varied by 10% of the expected number of signal events, one has

$$Z \sim \frac{S \pm 0.1 \cdot S_{exp}}{\sqrt{B}} = \frac{S}{\sqrt{B}} \pm 0.1\frac{S_{exp}}{\sqrt{B}}. \tag{5.4}$$

The observed statistical significance can be affected by 10% of the expected significance.

For each category, a pool of background function candidates are tested with the aforementioned criteria. These functions include the exponential function, the 2nd order exponentiated polynomials, and the 2nd, 3rd and 4th order Bernstein polynomials. If more than one background function candidates pass the criteria, the expected significance of the analysis is evaluated with each of these candidates. The function that gives the best expected significance is selected. The selected background function's $n_{spr,max}$ is assigned as its systematic uncertainty.

In the likelihood function, this systematic uncertainty enters the signal normalization as shown in Eq. 6.6. Table 5.6 summarizes the selected background function and the size of background modeling uncertainty for each category.

Table 5.6 Systematic uncertainty on the number of signal events fitted due to the background parametrization, given in number of events. Three different background parametrizations are used depending on the category: an exponential function; a fourth-order Bernstein polynomial; and the exponential of a second-order polynomial.

Category	Parametrization	Uncertainty $[N_{\mathrm{evt}}]$	
		$\sqrt{s} = 7$	$\sqrt{s} = 8$
Inclusive	4th order pol.	7.3	10.6
Unconverted central, low p_{Tt}	Exp. of 2nd order pol.	2.1	3.0
Unconverted central, high p_{Tt}	Exponential	0.2	0.3
Unconverted rest, low p_{Tt}	4th order pol.	2.2	3.3
Unconverted rest, high p_{Tt}	Exponential	0.5	0.8
Converted central, low p_{Tt}	Exp. of 2nd order pol.	1.6	2.3
Converted central, high p_{Tt}	Exponential	0.3	0.4
Converted rest, low p_{Tt}	4th order pol.	4.6	6.8
Converted rest, high p_{Tt}	Exponential	0.5	0.7
Converted transition	Exp. of 2nd order pol.	3.2	4.6
2-jets	Exponential	0.4	0.6

Chapter 6

Statistical Methodology

This chapter describes the statistics methodology used to interpret data. Ref. [92] provides a detailed documentation on the methodology used to combine the Higgs boson searches at the LHC. The focus of this chapter is on how to implement the procedure suggested by Ref. [92] into the $H \to \gamma\gamma$ search and measurement. Sec. 6.1 introduces a general likelihood model used for searching a resonance on top of a smooth falling background. Sec. 6.2 presents the hypothesis testing method used to interpret data at the LHC experiments. Finally, the search procedure is defined in Sec. 6.3 and the expected analysis performance is reported in the same section.

6.1 The Likelihood Model

6.1.1 Modeling the signal $m_{\gamma\gamma}$ distribution

A linear combination of a Crystal Ball (CB) function [93] and a Gaussian function is used to model the signal $m_{\gamma\gamma}$ distribution. The CB function is defined as

$$f_{CB}(m_{\gamma\gamma}) = N \cdot \begin{cases} e^{-t^2/2} & \text{if } t > -\alpha \\ (\frac{n}{|\alpha|})^n \cdot e^{-|\alpha|^2/2} \cdot (\frac{n}{|\alpha|} - |\alpha| - t)^{-n} & \text{otherwise} \end{cases} \tag{6.1}$$

where $t = (m_{\gamma\gamma} - m_H - \delta_{m_H})/\sigma_{CB}$, N is a normalization parameter, m_H is the hypothesized Higgs boson mass, δ_{m_H} is a category dependent offset, σ_{CB} is the width parameter that represents the diphoton invariant mass resolution, and n and α parametrize the non-Gaussian tail. In this parameterization, the mean value of the CB function is $m_H + \delta_{m_H}$ and it means that the peak in $m_{\gamma\gamma}$ differs from the hypothetical m_H by δ_{m_H}. The complete signal PDF is then written as:

$$f_S(m_{\gamma\gamma}) = \chi \cdot f_{CB} + (1-\chi) \cdot (m_{\gamma\gamma}; m_H + \delta_{m_H}, \sigma_G) \tag{6.2}$$

where the mean value of the Gaussian function is set to be the same as the CB function, σ_G is the width of the Gaussian function, and χ is the fraction of the CB component in the signal PDF. Fig. 6.1 shows the signal $m_{\gamma\gamma}$ distribution at m_H = 120 GeV superimposed with the fit of the Crystal Ball plus Gaussian function. For $H \to \gamma\gamma$ signal MC samples, the fit favored value of parameter χ is beyond 90%, which indicates that the Crystal Ball function models the peak part of the $m_{\gamma\gamma}$ distribution while the Gaussian function models the tail part of the $m_{\gamma\gamma}$ distribution.

To produce signal PDFs at m_H values where Monte Carlo samples are not available, all signal parameters are assumed to have a linear dependence on m_H. The slope and offset of this linear parameterization are determined in a simultaneous fit to signal Monte Carlo samples at 10 different m_H from 100 GeV to 150 GeV. In this simultaneous fit, the mean values of the CB function and the Gaussian function are forced to be the same, and the widths of the CB function and the Gaussian function are fully correlated which means that σ_{CB} and σ_G always differ by a constant. The effects of the linear-dependence assumption and correlation requirement have been checked with Monte Carlo samples, and no obvious bias is observed when these requirements are imposed. At each of the 10 m_H points where the Monte Carlo samples are available, the signal PDF determined from the simultaneous fit is found to reproduce the signal PDF determined from a fit to Monte Carlo samples at the single m_H point.

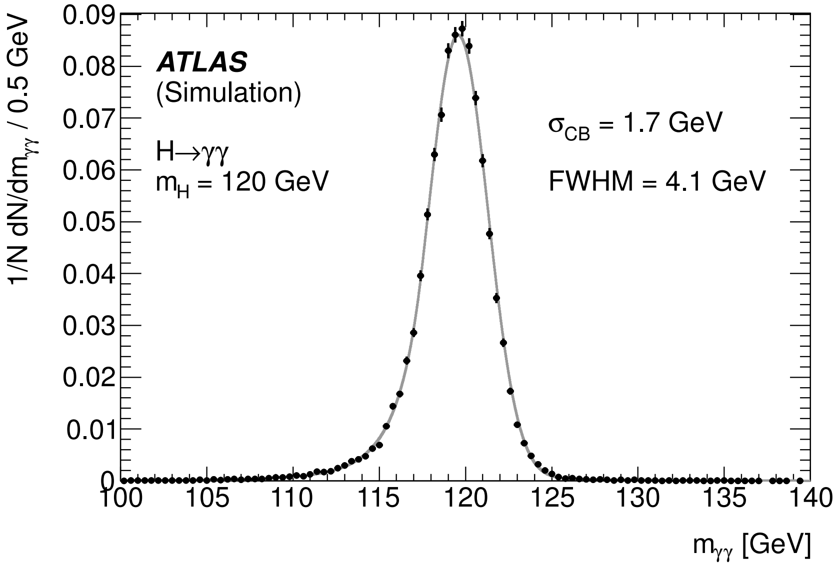

Figure 6.1 Reconstructed invariant mass distribution for a simulated signal of m_H = 120 GeV, superimposed with the fit to the signal model.

In a fit to data, the signal shape parameters are fixed to the values determined from Monte Carlo samples. The uncertainty on this parameterization mainly arises from the photon energy determination and is discussed in Sec. 5.3.2.1.

6.1.2 Modeling the background invariant mass distribution

The background $m_{\gamma\gamma}$ distributions are modeled by a number of smooth analytic PDFs, including the exponential function, exponentiated polynomials, Bernstein polynomials, etc.. The parameters of these background functions are treated as free parameters in a fit and their values are fully determined by data as the current available Monte Carlo samples cannot provide a precision background shape prediction. The effect of leaving these parameters free in a fit is equivalent to increasing the statistical uncertainty so that the systematic uncertainty can be mitigated. The procedure of choosing a background function and the treatment of the background modeling uncertainty are detailed in Sec. 5.3.

6.1.3 The expression of the signal expectation

The expected signal yield with systematic uncertainties can be expressed as:

$$N_S = \mu \cdot \prod_i \Theta_i \cdot n_s \tag{6.3}$$

where μ is the signal strength parameter, n_s is the nominal value of the expected signal yields after the selection, i is the index of nuisance parameter, and Θ_i is the expected contribution of a particular nuisance parameter θ_i which can be further expanded to:

$$\Theta_i = 1 + \theta_i \cdot \delta_i \tag{6.4}$$

where the nuisance parameter θ_i is normalized and takes the meaning of the number of standard deviations from the nominal value, and δ_i is the size of the nuisance parameter's corresponding systematic uncertainty.

If there are multiple categories involved in the analysis, the expected contribution of the nuisance parameter can be rewritten as:

$$\Theta_{i,l} = 1 + \theta_i \cdot \delta_{i,l} \cdot \beta_l \tag{6.5}$$

where l is the index of category, the size of the systematic uncertainty, $\delta_{i,l}$ is category-dependent, and β_l is a coefficent that controls the sign of correlation of the same nuisance parameter between categories. In the case that a systematic uncertainty is uncorrelated between categories, each category is assigned one nuisance parameter, $\theta_{i,l}$. Here, the nuisance parameter $\theta_{i,l}$ has no impact on the signal yield in category $k(k \neq l)$, and therefore, $\beta_{i,k}$ is set to be 0.

The contribution from the background modeling uncertainty is dependent on the background and does not scale with the size of signal yield . This contribution, therefore, introduces an additive term in the expected signal yield:

$$N_S = \mu \cdot \prod_i \Theta_i \cdot n_s + \theta_{spr} \cdot n_{spr} \tag{6.6}$$

where θ_{spr} is the nuisance parameter for the background modeling uncertainty and n_{spr} is the size of the background modeling uncertainty in the unit of number of events. The determination of n_{spr} is detailed in Sec. 5.3.2.

At a particular mass point $m^j_{\gamma\gamma}$, the expected signal yield can be written as:

$$N^{exp}_S = N_S \cdot f(m^j_{\gamma\gamma} \mid m_H) \tag{6.7}$$

where $f(m^j_{\gamma\gamma} \mid m_H)$ is the $m_{\gamma\gamma}$ PDF for a signal at m_H.

Similarly, the expected background yield at the point of $m^j_{\gamma\gamma}$ is:

$$N^{exp}_B = N_B \cdot g(m^j_{\gamma\gamma}) \tag{6.8}$$

where $g(m^j_{\gamma\gamma})$ is the background $m_{\gamma\gamma}$ PDF, and N_B is the number of background events which is determined from data.

The total expected yield at the point of $m^j_{\gamma\gamma}$, then is

$$N^{exp}_{tot} = N_S \cdot f(m^j_{\gamma\gamma} \mid m_H) + N_B \cdot g(m^j_{\gamma\gamma}) \tag{6.9}$$

6.1.4 The likelihood without incorporating systematic uncertainties

With the expected event yield at the point of $m^j_{\gamma\gamma}$, the likelihood of observing one event at the same mass point is:

$$L_j = Pois(1 \mid N^{exp}_{tot}) \tag{6.10}$$

where $Pois$ represents the $Poisson$ function.

The likelihood of observing all the events in the category l is:

$$L_l = \prod_{j=1}^{n_l} L_{j,l} \tag{6.11}$$

where n_l is the total number of events in the category l.

The likelihood combining all categories then is:

$$L_{comb} = \prod_{l=1}^{N_c} L_l = \prod_{l=1}^{N_c} \prod_{j=1}^{n_l} L_{l,j} \tag{6.12}$$

where N_c is the total number of categories.

The likelihood described by Eq. 6.12 is the statistcal component of the final likelihood.

6.1.5 The likelihood incorporating systematic uncertainties

Both the signal strength parameter and nuisance parameters are free parameters, and in a fit, this can present multiple possible sets of maximum likelihood estimators and thus prevent the fit from converging. This is dealt with by introducing a constraint PDF and a global observable for each nuisance parameter. The constraint PDF can be written as:

$$\zeta(\theta_i^R \mid \theta_i) \tag{6.13}$$

where θ_i^R is the observable of the constraint PDF $\zeta(\theta_i)$. It is named the "global observable" in order to distinguish from the analysis observable $m_{\gamma\gamma}$. The constraint PDF can be $Gaussian$, $LogNormal$, etc.. In a fit, the deviation of a nuisance parameter from its nominal value would introduce a negative contribution to the log likelihood from its constraint PDF, thus breaking the degeneracy between the signal strength and nuisance parameters.

The final likelihood that incorporates the effect of systematic uncertainties is:

$$L_{final} = L_{comb} \cdot \prod_i \zeta(\theta_i^R \mid \theta_i) \tag{6.14}$$

Eq. 6.14 also reveals the statistical implication of the constraint PDF. In the final likelihood function, constraint PDFs $\prod_i \zeta(\theta_i^R \mid \theta_i)$ are acting as likelihood functions of auxiliary measurements of the nuisance parameter θ_is. The global observable θ_i^R is the "observed" value of the nuisance parameter θ_i in an auxiliary measurement. The value of the global observable should take the best estimation of the nuisance parameter. In the $H \to \gamma\gamma$ analysis, until there is a signal with very a large number of events in data, no statistically meaningful estimation of the signal related nuisance parameters can be obtained by fitting data. The best estimation of these nuisance parameter values should therefore come from the Monte Carlo. This is equivalent to requiring the global observables to take the nominal values of the nuisance parameters.

6.2 Hypothesis testing and its application in the $H \rightarrow \gamma\gamma$ analysis

6.2.1 Hypothesis Testing

The general idea of hypothesis testing is to interpret one particular experimental outcome in the context of an ensemble of pseudo-experimental outcomes that are generated from a given hypothesis of experimental observables in order to determine the compatibility between the particular experimental outcome and the hypothesis.

A hypothesis should be concerned with one or more $parameters\ of\ interest$ that characterize the experimental outcome. For instance, in an experiment searching for a signal (a "search analysis"), the signal strength parameter, μ, is usually chosen as the parameter of interest. The scenarios of $\mu = 0$, $\mu > 0$ and $\mu < 0$ correspond to an agreement with background expectation, an excess over the background expectation, and a deficit under the background expectation. In a search analysis, a background-only hypothesis means that $\mu = 0$, i.e., there is only background. A signal plus background hypothesis means that $\mu = \mu_0$, i.e., there is a signal component and the strength of the signal component is μ_0, a positive value to be tested.

An ensemble of pseudo-experiments are generated from a hypothesis. In a pseudo-experiment, the number of events is randomly generated from a poisson distribution whose mean value is the event yield expectation of the hypothesis. This randomization can be done in an observable-dependent way when the experiment investigates a distribution of observable instead of the event count.

The information of the experimental outcome needs to be condensed to a single variable, and this variable is the *test statistic*. A test statistic can be simply the parameter of interest itself or a more complicated construction related to the parameter of interest, for example, a likelihood ratio.

The hypothesis testing is done by comparing the test statistic value of a real experimental outcome and the test statistic distribution of an ensemble of pseudo-experimental outcomes. This is illustrated by the symbolic plot shown in Fig. 6.2 [94]. The probability that the given hypothesis fluctuates to give an observation such as the one from the real experiment can be calculated from the observed test statistic value and the test statistic distribution from the pseudo-experiments, and this probability is the p-value of the hypothesis given the observation.

6.2.2 p-value and confidence level

As mentioned in Sec. 6.2.1, the p-value is the probability that a given hypothesis fluctuate to give an observation such as the one from the real experiment. In the case of calculating the statistical significance of an excess, the hypothesis to be tested is the background-only ($\mu = 0$) hypothesis, and the p-value is usually called the p_0-value to indicate the hypothesis tested is a background-only hypothesis.

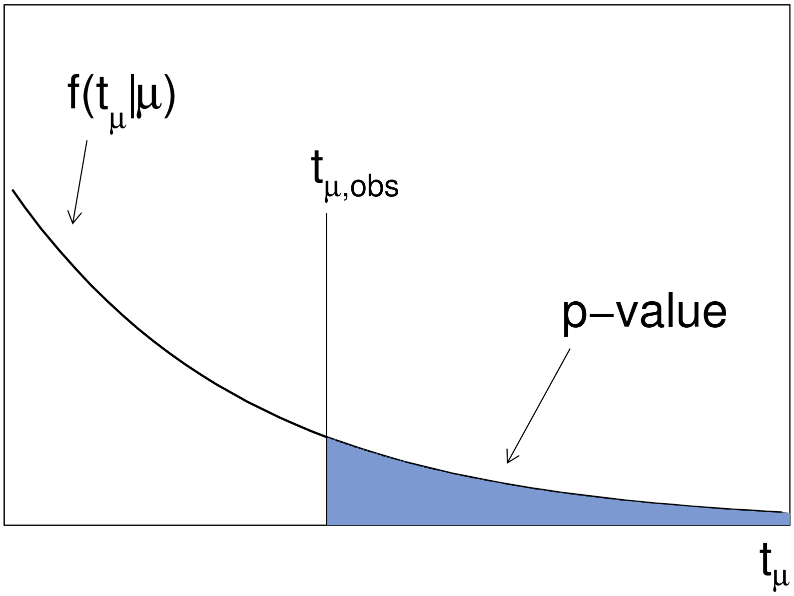

Figure 6.2 For each pseudo-experiment, the test statistic is calculated, and the distribution of the test statistic from pseudo-experiments of a hypothesis H_0 is shown as the solid black curve. The test statistic value determined from the real experiment is the labeled as $t_{\mu,obs}$. The shaded area on the right of $t_{\mu,obs}$ is the probability that the H_0 hypothesis fluctuates and gives an observation such as the one from the real experiment. This shaded area is the p-value of H_0 hypothesis.

When setting a limit on a particular cross section of a signal, the hypothesis to be tested is a signal-plus-background hypothesis, and the p-value is usually converted to a confidence level, CL where $CL = 1 - p$-value. In a fully *frequentist* statistics test, a hypothesis is claimed to be excluded if the CL calculated from data is $\geq 95\%$.

Although this confidence level is used to set a limit on a specific value of the signal strength, it is a confidence level of a signal plus background hypothesis and hence it is also denoted as CL_{s+b}.

For a specific experimental outcome, the rejection of a signal-plus-background hypothesis can be due to either the absence of a signal or a downward background fluctuation.

6.2.2.1 CL_s limit

To avoid setting an aggressive limit due to a strong downward background fluctuation, a modified frequentist CL_s method [95] is introduced. In the CL_s method, the confidence level of the signal-plus-background hypothesis is normalized to the confidence level of background-only hypothesis, and the resulting ratio, CL_s (see Eq. 6.15) is used to define the criteria that a hypothesis is rejected.

$$CL_s = \frac{p_{s+b}}{1 - p_b} \tag{6.15}$$

The CL_s is a ratio of confidence levels and does not have the probabilistic meaning. As a convention adopted in collider physics in recent years, a signal-plus-background hypothesis is claimed to be rejected at 95$\%$ CL when the CL_s is less than 0.05.

6.2.3 The profile likelihood ratio

The profile likelihood ratio [94] is used as the test statistic for this analysis and the parameter of interest is μ. In this case, the profile likelihood ratio is defined as:

$$q_\mu(\mu_0) = -2ln\frac{L(\mu_0, \hat{\theta})}{L(\hat{\mu}, \hat{\hat{\theta}})} \tag{6.16}$$

where θ is a collective denotation of nuisance parameters, the numerator of the likelihood ratio is the conditional maximum likelihood when μ is fixed to the test value μ_0, the denominator is the unconditional maximum likelihood, and parameters with a hat or double hats are maximum likelihood estimators. In this construction, the likelihood in the numerator is the likelihood of observing the outcome in data given the hypothesis of $\mu = \mu_0$.

Specific restrictions on μ are applied to the calculation of q_μ: when the test statistic is defined with a background-only hypothesis ($\mu = 0$), $\hat{\mu}$ is required to be greater than or equal to 0; when the test statistic is defined with a signal-plus-background hypothesis ($\mu = \mu_{test}$), $\hat{\mu}$ is required to be less than or equal to μ_{test}. These restrictions are imposed to ensure that the test statistic is $one - sided$.

In the context of this analysis, the "one-sided" requirement means that the hypothesis is rejected if $\mu < \mu_{test}$ ($\mu > 0$) when testing signal-plus-background (background-only) hypothesis. A "two-sided" test means that the hypothesis is rejected if $\mu \neq \mu_{test}$ ($\mu \neq 0$) when testing signal-plus-background (background-only) hypothesis.

6.2.4 Asymptotic formulae for the profile likelihood ratio

One important property of the profile likelihood ratio is that the q_μ distribution for an ensemble of pseudo-experiments generated from the hypothesis used to construct the profile likelihood ratio follows a $\frac{1}{2}\chi^2 + \frac{1}{2}\delta$ distribution, as demonstrated in Ref. [96, 97, 94]. This further leads to another important deduction: $\sqrt{q_{\mu,obs}}$ is equal to the statistical significance of the observation. This is usually referred to as the $asymptotic\ formulae$ or $asymptotic\ approximation.$ Since the computing resources required for hypothesis testing are huge in terms of time consumption and number of CPUs, the asymptotic approximation is essential to deriving results reported in this thesis.

6.2.4.1 Validity of the asymptotic formulae

The validity of the asymptotic formulae has been checked extensively in the context of the $H \to \gamma\gamma$ analysis. The implementation of two shape related uncertainties, the diphoton mass resolution uncertainty, and the diphoton mass scale uncertainty, are found to moderately break the asymptotic behavior of the test statistic. Fig. 6.3 shows the comparison between the $\frac{1}{2}\chi^2 + \frac{1}{2}\delta$ distribution and the pseudo-experiment distribution with different systematic uncertainty setups. The introduction of diphoton mass resolution uncertainty slightly worsens the agreement between these two distributions, and the implementation of diphoton mass scale uncertainty leads to a moderate breakdown of the asymptotic behavior at the tail part of the test statistic distribution, thus giving a larger p-value. In a fit, the diphoton mass scale uncertainty is effectively playing a very similar role to a float m_H parameter. In the case that both μ and m_H are treated as parameters of interest, the test statistic distribution is expected to follow a 2 degree-of-freedoms χ^2 distribution. The diphoton mass scale nuisance parameters are left free in both of the two fits that construct the test statistic, and they don't behave exactly the same as a parameter of interest in a fit. This means that the test statistic distribution from a likelihood model that incorporates diphoton mass scale uncertainties

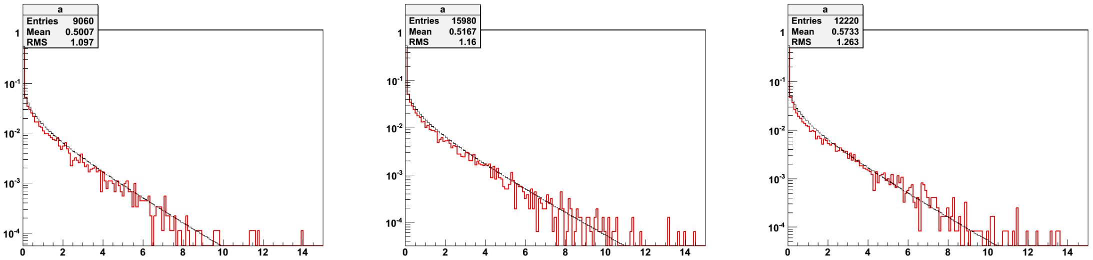

Figure 6.3 The test statistic q_0 distribution from an ensemble of background-only pseudo experiments. In the left plot, both the diphoton mass scale uncertainties and diphoton mass resolution uncertainty are not incorporated into the likelihood model. In the middle plot, the diphoton mass scale uncertainties are not incorporated into the likelihood model, but the diphoton mass resolution uncertainty is. In the right plot, both the diphoton mass scale uncertainties and diphoton mass resolution uncertainty are incorporated into the likelihood model.

will likely have a distribution in the middle between the 1 degree-of-freedom χ^2 approximation and the 2 degree-of-freedoms χ^2 approximation, which explains the larger tail shown in the right plot in Fig. 6.3.

6.2.5 Measurement

The profile likelihood ratio can also be used to measure a quantity from data. This quantity should be taken as the parameter of interest of the profile likelihood ratio. The central value of the quantity is the best-fit value of the parameter of interest and the uncertainty of the measured central value can be determined by finding the hypothetical values of the parameter of interests that are rejected by data at 68% CL. Performing a measurement using the profile likelihood ratio harmonizes the statistical implementation for the "search" analysis and the "measurement" analysis, and the same likelihood model used for the "search" analysis can be used to perform measurements.

6.2.5.1 The signal strength measurement

In the "search" analysis, the best-fit signal strength will be reported for quantifying the size of an excess or deficit. In this measurement, the best-fit signal strength is determined from a maximum likelihood fit to data, which corresponds to the denominator of the profile likelihood ratio shown in Eq. 6.16. To determine the uncertainty of this measurement, a scan of hypothetical μ values is performed to identify the μ_c that gives $-2ln\lambda(\mu) = 1$. This will give two μ_c, a μ_{c+} corresponding to the upper bound of the uncertainty, and a μ_{c-} corresponding to the lower bound of the uncertainty. Then the uncertainty of the measurement will be ${}^{+\mu_{c+}-\hat{\mu}}_{-\hat{\mu}-\mu_{c-}}$.

The requirement of $-2ln\lambda(\mu) = 1$ comes from $Wilks'\ theorem$ [96]. One can also understand this requirement with the asymptotic approximation, as μ values that give $\sqrt{-2ln\lambda(\mu)} = 1$ are rejected by data at the level of 1 standard deviation.

6.2.5.2 Systematic uncertainty and statistical uncertainty separation

In a measurement, it is also desirable to separate the statistical uncertainty and the systematic uncertainty. This is done in two steps. First, all the nuisance parameters related to systematic uncertainties are fixed to their fit-favored values. Then, the profile likelihood ratio scan over the parameter of interest is performed again, and a new uncertainty can be obtained from this scan. This new uncertainty is the statistical uncertainty as all possible effects of systeamtic uncertainty are removed by fixing their nuisance parameters to fit-favored values. Second, the systematic uncertainty can be subtracted from the total uncertainty and the statistical uncertainty with the assumption that the total uncertainty is the quadratic sum of the systematic uncertainty and statistical uncertainty. This assumption involves two independent assumptions: the systematic uncertainty and the statistical uncertainty are independent, and both the statistical and systemtic uncertainties are Gaussian-like, so that their total effect is calcualted from a quadratic summation. The first assumption is self-evident, but the latter one is not always valid, especially when the number of events is small and the staitistical uncertainty is more Poisson-like.

6.2.5.3 The mass measurement

In the case that a significant excess is observed, the mass of the particle responsible for the excess can be measured by taking m_H as the parameter of interest. All signal shape parameters are implemented as linear functions of m_H, and this linear dependence approximation is validated with Monte Carlo samples. The signal strength parameter is treated as an unconstrained nuisance parameter. With this modified likelihood model, the profile likelihood ratio for the mass measurement can be defined as:

$$-2ln\lambda(m_H) = -2ln\frac{L(m_H, \hat{\mu}, \hat{\theta})}{L(\hat{m_H}, \hat{\hat{\mu}}, \hat{\hat{\theta}})} \tag{6.17}$$

6.2.5.4 Two dimensional measurements

The profile likelihood ratio can also be used to measure two quantities simultaneously. For example, A and B are two quantities to be measured, and they are taken as the parameters of interest in the profile likelihood ratio. The test statistic should be:

$$-2ln\lambda(A,B) = -2ln\frac{L(A,B,\hat{\theta})}{L(\hat{A},\hat{B},\hat{\hat{\theta}})} \tag{6.18}$$

Since there are two parameters of interest, the uncertainty of this measurement is a contour in the two dimensional plane of A-B. The possible correlation between the measurement of quantity A and the measurement of quantity B can be revealed from this 2-D measurement. One example is to measure the mass of the particle and the signal strength parameter simultaneously. In this case, both m_H and μ are parameters of interest, and the profile likelihood ratio is defined as:

$$-2ln\lambda(\mu,m_H) = -2ln\frac{L(m_H,\mu,\hat{\theta})}{L(\hat{m_H},\hat{\mu},\hat{\hat{\theta}})} \tag{6.19}$$

Since there are two parameters of interest, the uncertainty of the measurement is presented as a contour in the 2-D plane of m_H-μ. The likelihood ratio values corresponding to 2 degree-of-freedoms are used to define the 68%, and 95% confidence levels [98].

6.3 Search procedure and expected analysis performance

6.3.1 The search procedure

The statistical interpretation will be performed for a series of hypothetical Higgs boson masses m_H. This interpretation consists of setting a CL_s limit on μ, evaluating the p_0-value, and evaluating the best-fit signal strength μ. The choice of step size between the two nearby Higgs boson mass hypotheses is related to the $m_{\gamma\gamma}$ resolution. Searching with a very large step size may potentially miss a real signal excess located between the two nearby m_H hypotheses. On the other hand, if the step is too small, there is a larger chance to pick up unphysical fluctuations. Given that the $m_{\gamma\gamma}$ resolution is about 1.7 GeV, the step size is chosen to be 0.5 GeV, resulting in 81 m_H points to be investigated in the range of 110 GeV $\leq m_H \leq$ 150 GeV. This range is where the branching ratio of $H \to \gamma\gamma$ reaches its maximum value and gives competitive sensitivity compared to other channels, such as $H \to ZZ^{(\star)} \to 4l$ and $H \to WW^{(\star)} \to l\nu l\nu$ channels.

6.3.1.1 $look - elsewhere$ effect

The p_0-value discussed by far is in fact the "local" p_0-value, because it is the probability that the background fluctuates to give an excess or deficit at a particular mass. It is also legitimate to ask: what is the probability that the background fluctuates to give an excess or deficit at anywhere in the mass range being investigated? The answer to this question is the so-called "global" p_0-value. It is somehow more approporiate to question the global p_0-value of an excess as the m_H is $a\ priori$ unknown.

In Ref. [99], a method to estimate the global p_0-value is proposed. Following this method, one should first obtain the average number of up-crossings N_c at an abitrary reference local significance level Z_0 from pseudo-experiments. The number of up-crossings is the number of times that the observed significance as a function of m_H crosses a reference significance level in a dataset. Then, $N_c(Z_{obs})$, the average number of up-crossings at the observed local significance Z_{obs} can be extrapolated from the $N_c(Z_0)$, and the $N_c(Z_{obs})$ is the ratio of the global p_0-value over the local p_0-value so that the global p_0-value can be calculated. In practice, the reference significance level is usually chosen to be 0, so that the number of up-crossings then reduces to the number of times that the best fit signal strength crosses 0 upwards in the full mass range being investigated. The $average$ number of up-crossings can be obtained from pseudo-experiment. In this analysis, the N_c is found to be about 3.3.

6.3.2 Pseudo-experiments and implementation of the diphoton mass scale uncertainty

Sec. 6.2.4.1 has shown that the asymptotic approximation is not strictly valid once the diphoton mass scale uncertainty is implemented. As the breakdown of the asymptotic behavior happens at the tail part of the test statistic distribution, its impact on the p-value and significance varies for different observations. The diphoton mass scale uncertainty does not have a clear meaning in the absence of an excess in data, and therefore, the likelihood model without the diphoton mass scale uncertainties is used for the limit setting and the asymptotic formulae is used to derive the limit. The p_0-value is also calculated from the likelihood model without the diphoton mass scale uncertainties using the asymptotic formulae, and when there is a significance excess in data, the p_0-value is determined from pseudo-experiments with a likelihood model that incorporates the diphoton mass scale uncertainties.

6.3.3 The expected analysis performance

The expected significance is the significance evaluated on a pseudo-dataset where the data are in perfect agreement with a SM signal-plus-background hypothesis. The expected limit on μ is the limit on μ evaluated on a pseudo-dataset where the data are in perfect agreement with a background-only hypothesis. The typical expected significance and expected CL_s limit on μ at a few benchmark m_H are summarized in Table 6.1. The analysis is most sensitive to a Higgs boson signal with $m_H \sim$ 125 GeV, and the expected significance can be as large as 2.5 σ for a SM Higgs boson at $m_H = 125$ GeV

Table 6.1 The expected significance Z_{exp} and the expected 95% CL_s limit μ_{up} at 9 benchmark m_H points for the $\sqrt{s} = 7$ TeV sample, $\sqrt{s} = 8$ TeV sample, and their combination.

m_H (GeV)	Combined		$\sqrt{s} = 7$ TeV		$\sqrt{s} = 8$ TeV	
	$Z_{exp}\sigma$	μ_{up}	$Z_{exp}\sigma$	μ_{up}	$Z_{exp}\sigma$	μ_{up}
110	2.08	0.97	1.36	1.52	1.60	1.28
115	2.27	0.88	1.48	1.38	1.74	1.17
120	2.42	0.84	1.58	1.30	1.85	1.10
125	2.47	0.83	1.61	1.29	1.90	1.09
130	2.42	0.86	1.58	1.33	1.86	1.13
135	2.30	0.90	1.50	1.40	1.77	1.19
140	2.11	0.99	1.38	1.53	1.61	1.30
145	1.74	1.17	1.13	1.81	1.33	1.54
150	1.28	1.83	0.84	2.45	0.98	2.08

Chapter 7

Observation of an excess of events

This chapter reports the observation of an excess of diphoton events in the search analysis defined in Chapter. 5. The $m_{\gamma\gamma}$ distributions are presented in Sec. 7.1. The statistics interpretation is carried out following the procedure defined in Sec. 6.3.1. Sec. 7.2 reports the limit on μ. Sec. 7.3 reports the p_0-value results. Sec. 7.4 reports the best-fit signal strength. Sec. 7.5 reports the measurement of the mass of the observed excess. Each section also documents additional checks performed to scrutinize the excess. Sec. 7.6 reports the observation of excesses in the other Higgs boson search channels, namely, the $H \to ZZ^{(\star)} \to 4l$ and $H \to WW^{(\star)} \to l\nu l\nu$ channels, and the discovery of a new boson established by the statistical combination of all Higgs boson search analyses.

7.1 The diphoton invariant mass distributions

The $m_{\gamma\gamma}$ distributions for the 20 categories are shown in Figures 7.1 – 7.5. In each of these figures, the data distribution is shown as black points with $Poisson$ error bars, the expected background distribution determined from a background-only fit is shown as a red solid line, and the expected signal distribution at m_H= 126.5 GeV normalized to the Standard Model prediction is shown as a dashed line on top of the expected background distribution. The $m_{\gamma\gamma}$ distribution of all selected events in the $\sqrt{s}$ $=$ 7 TeV and $\sqrt{s}$ $=$ 8 TeV samples is shown in in Fig. 7.6. In this figure, the expected background distribution is a normalization-weighted sum of fitted individual background PDFs from the 20 categories, and the SM signal distribution is also shown. An excess of diphoton events at around $m_{\gamma\gamma}$ $\sim$ 126 GeV is already discernible.

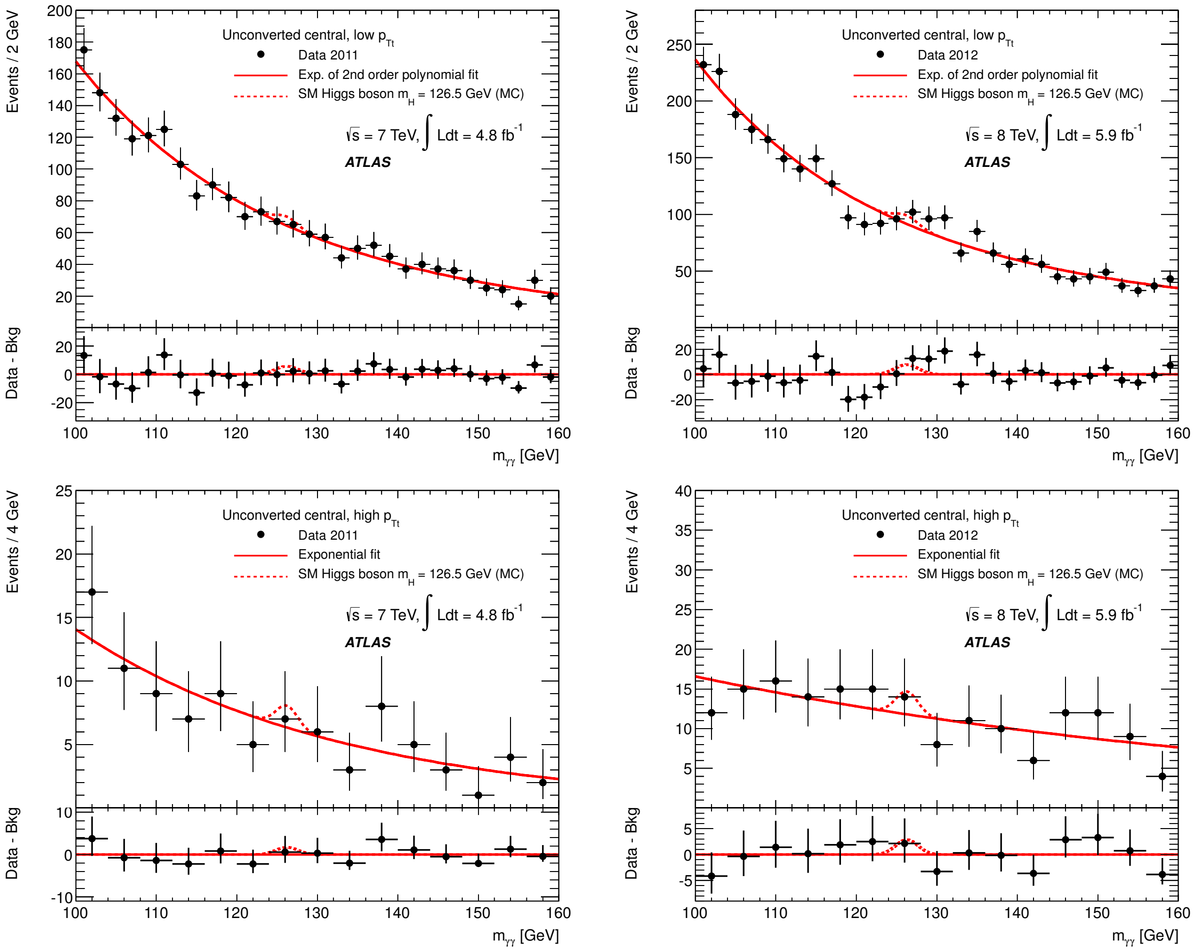

Figure 7.1 Background-only fits to the diphoton invariant mass spectra for categories Unconverted central, low p_{Tt}, and Unconverted central, high p_{Tt}. The bottom inset displays the residual of the data with respect to the background fit. The Higgs boson expectation for a mass hypothesis of 126.5 GeV corresponding to the SM cross section is also shown. All figures on the left side correspond to the $\sqrt{s}$ = 7 TeV data sample and the ones on the right to the $\sqrt{s}$ = 8 TeV data sample

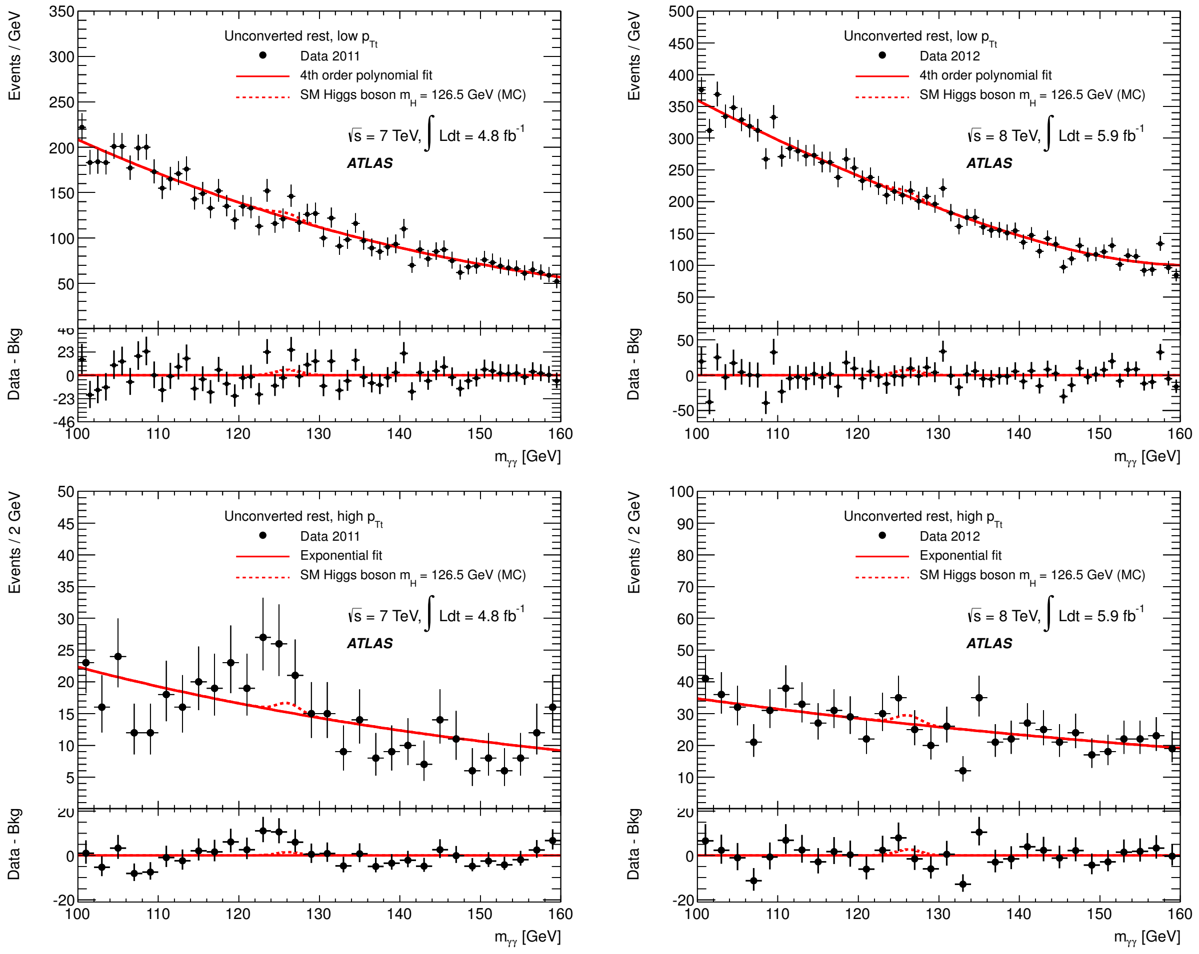

Figure 7.2 Background-only fits to the diphoton invariant mass spectra for categories Unconverted rest, low p_{T_t} and Unconverted rest, high p_{Tt}. The bottom inset displays the residual of the data with respect to the background fit. The Higgs boson expectation for a mass hypothesis of 126.5 GeV corresponding to the SM cross section is also shown. All figures on the left side correspond to the $\sqrt{s} = 7$ TeV data sample and the ones on the right to the $\sqrt{s} = 8$ TeV data sample

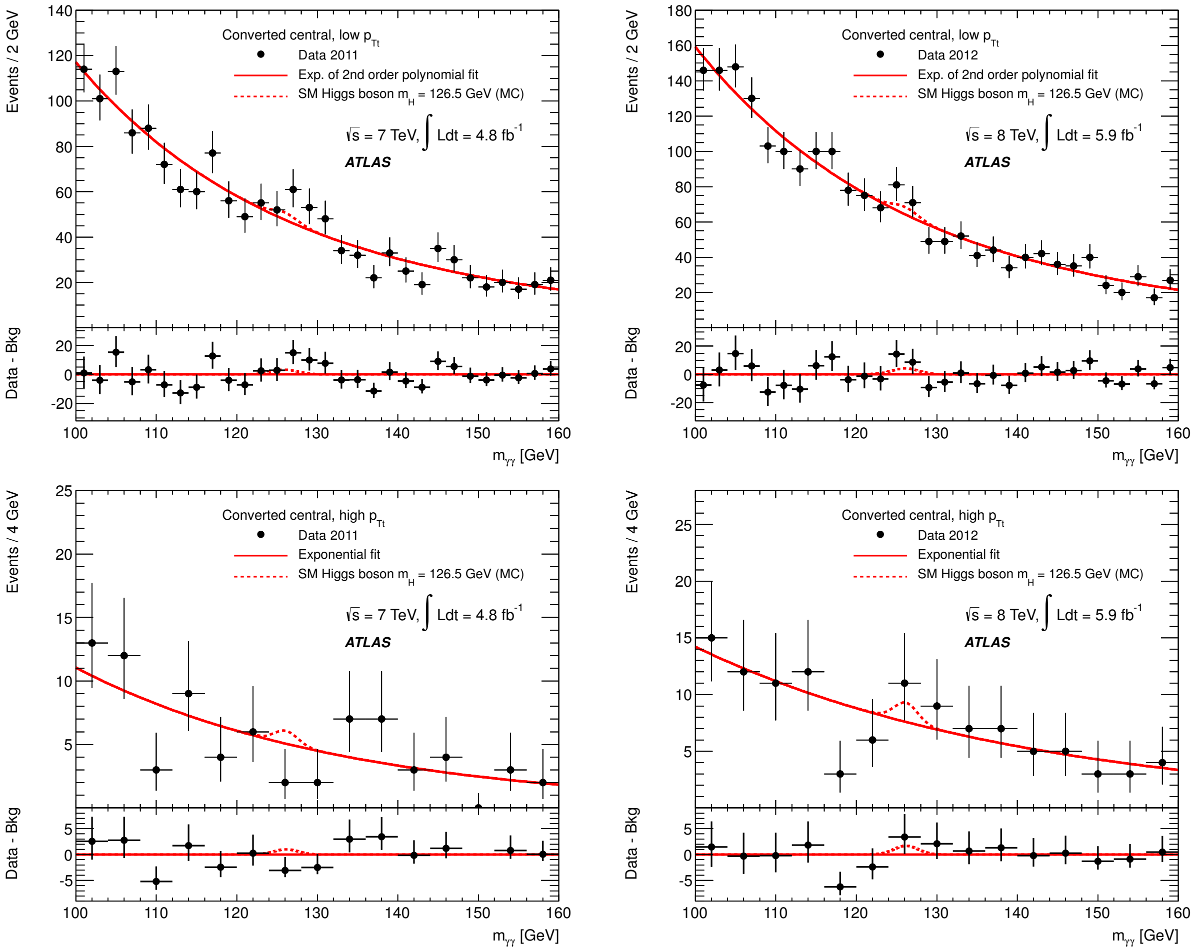

Figure 7.3 Background-only fits to the diphoton invariant mass spectra for categories Converted central, low p_{Tt}, and Converted central, high p_{Tt}, The bottom inset displays the residual of the data with respect to the background fit. The Higgs boson expectation for a mass hypothesis of 126.5 GeV corresponding to the SM cross section is also shown. All figures on the left side show the $\sqrt{s} = 7$ TeV data sample and the ones on the right show the $\sqrt{s} = 8$ TeV data sample.

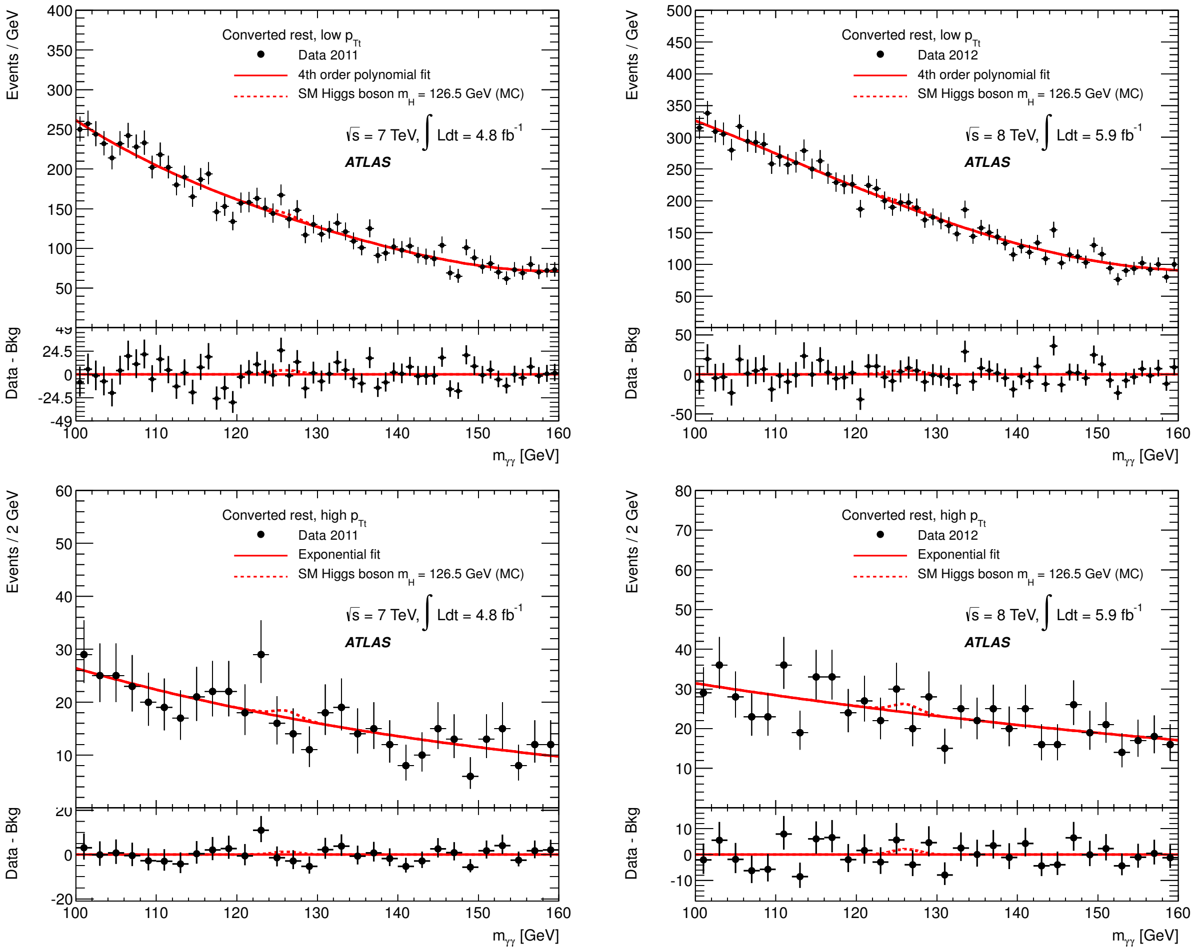

Figure 7.4 Background-only fits to the diphoton invariant mass spectra for categories Converted rest, low p_{Tt} and and Converted rest, high p_{Tt}. The bottom inset displays the residual of the data with respect to the background fit. The Higgs boson expectation for a mass hypothesis of 126.5 GeV corresponding to the SM cross section is also shown. All figures on the left side show the $\sqrt{s} = 7$ TeV data sample and the ones on the right show the $\sqrt{s} = 8$ TeV data sample.

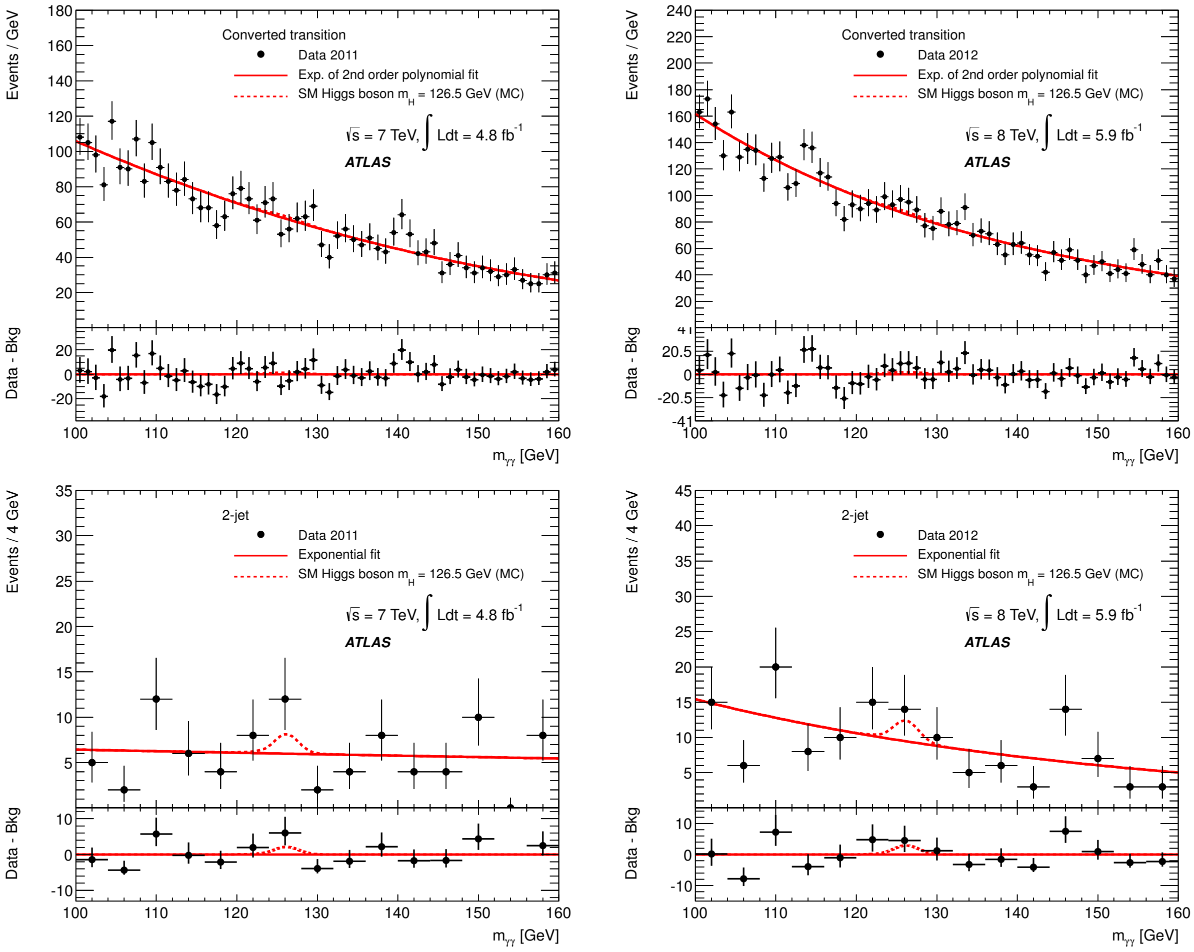

Figure 7.5 Background-only fits to the diphoton invariant mass spectra for categories Converted transition and 2-jets. The bottom inset displays the residual of the data with respect to the background fit. The Higgs boson expectation for a mass hypothesis of 126.5 GeV corresponding to the SM cross section is also shown. All figures on the left side show the $\sqrt{s} = 7$ TeV data sample and the ones on the left side show the $\sqrt{s} = 7$ TeV data sample and the ones on the right show the $\sqrt{s} = 8$ TeV data sample.

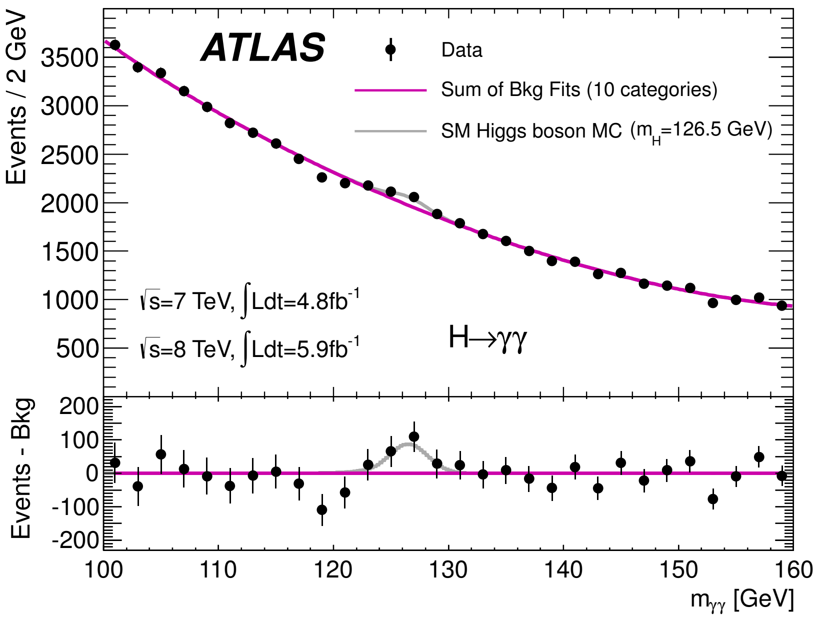

Figure 7.6 Invariant mass distribution of diphoton candidates for the combined $\sqrt{s}$ = 7 TeV and $\sqrt{s}$ = 8 TeV data samples, overlaid with the total background obtained from summing the fitted background-only models to the distributions in the individual categories. The bottom inset displays the residual of the data with respect to the total background. The Higgs boson expectation for a mass hypothesis of 126.5 GeV corresponding to the SM cross section is also shown.

7.2 Exclusion limit

Fig. 7.7 shows the CL_s limits for the $\sqrt{s} = 7$ TeV sample, $\sqrt{s} = 8$ TeV sample, and Fig. 7.8 shows the CL_s limits for the combination of the two samples.

The expected CL_s limit on μ from 7 TeV data ranges between 1.3 and 2.4 in the region of 110 GeV $< m_H <$ 150 GeV, and the best expected limit is achieved at $m_H \sim$ 125 GeV. The expected CL_s limit on μ from 8 TeV data ranges between 1.1 and 2.1 in the region of 110 GeV $< m_H <$ 150 GeV, and the best expected limit is achieved at $m_H \sim$ 125 GeV which is consistent

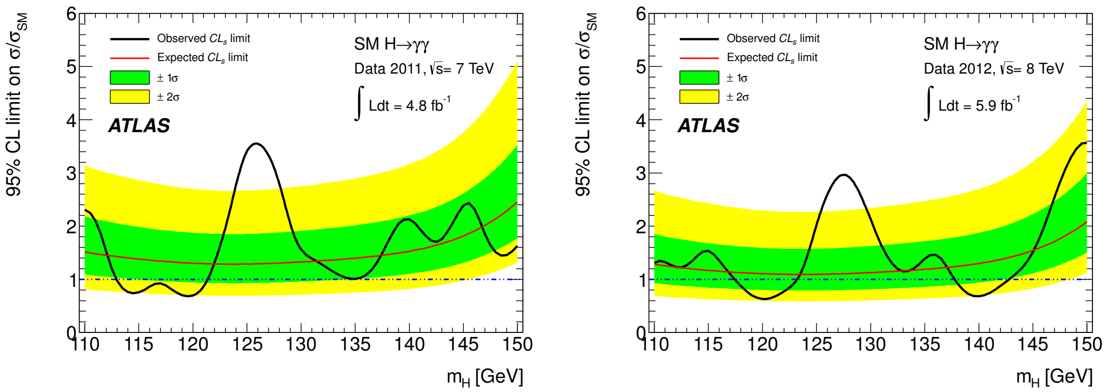

Figure 7.7 Observed and expected CL_s limit on the normalised signal strength as a function of the assumed Higgs boson mass for the $\sqrt{s}$ = 7 TeV (left) and $\sqrt{s}$ = 8 TeV (right) analyses. The dark (green) and light (yellow) bands indicate the expected limits with ± 1 sigma and ± 2 sigma fluctuations, respectively.

with the analysis at $\sqrt{s} = 7$ TeV. With the two analyses combined, the expected CL_slimit ranges between 0.8 and 1.6, and the SM Higgs boson is expected to be excluded at 95% CL in the range of 110 GeV $\leq m_H \leq$ 140.5 GeV. In the observed result of the combination of the two samples, the observed CL_s limit has excluded the SM Higgs boson hypothesis in the regions of 112 GeV $\leq m_H \leq$ 123 GeV and 132 GeV $\leq m_H \leq$ 143.5 GeV. In the range of 123 GeV $< m_H <$ 132 GeV, where the analysis is most sensitive to a SM Higgs boson, the observed CL_s limit on μ is as large as 2.8. In Fig. 7.8, the highest point in the observed limit curve is beyond the 2 σ upward uncertainty band of the background-only expectation, indicating the presence of a strong excess over the background expectation.

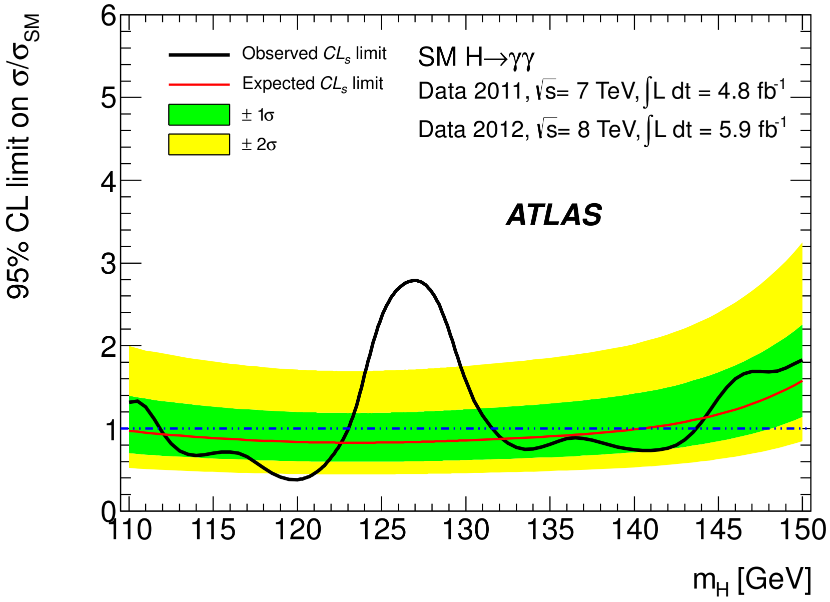

Figure 7.8 Expected and observed CL_s limit on the normalised signal strength as a function of the assumed Higgs boson mass for the combined $\sqrt{s}$ = 7 TeV and $\sqrt{s}$ = 8 TeV analysis. The dark (green) and light (yellow) bands indicate the expected limits with ± 1 sigma and ± 2 sigma fluctuations, respectively.

7.3 The observed p_0-value

As explained in Sec. 6.2.4.1, the p_0-value is calculated with a likelihood model that does not incorporate the diphoton mass scale uncertainties. The calculation is done for the $\sqrt{s}$ = 7 TeV sample, $\sqrt{s}$ = the 8 TeV sample, and the combination of the two samples using the asymptotic formulae. These results are shown in Fig. 7.9.

For the $\sqrt{s} = 7$ TeV sample, the smallest p_0-value, corresponding to the largest excess, is found to be 2.4 $\times 10^{-4}$ at $m_H = 126$ GeV. For the $\sqrt{s} = 8$ TeV sample, the smallest p_0-value is found to

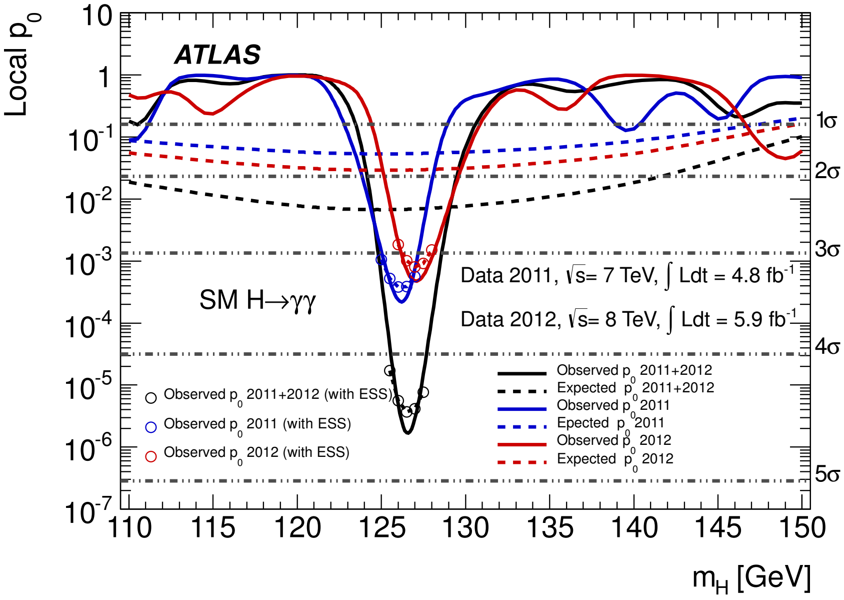

Figure 7.9 The observed p_0 is shown as a function of m_H for the 7 TeV analysis (blue), 8 TeV anlysis (red) and the combined analysis (black). The expected p_0 curves are also shown in dashed lines.

be 4.8 $\times 10^{-4}$ at $m_H = 127$ GeV. In the combination of the $\sqrt{s} = 7$ TeV and $\sqrt{s} = 8$ TeV samples, the smallest p_0-value is found to be 1.7 $\times 10^{-6}$ at $m_H = 126.5$ GeV.

Since significant excesses are seen at $m_H \sim 126$ GeV in both years' samples and the combination, p_0-values at around $m_H = 126.5$ GeV is calculated with a likelihood model that incorporates the diphoton mass scale uncertainties using pseudo-experiments. The pseudo-experiments are generated at the 5 m_H values surrounding the m_H where the largest excess is observed, and this is done for the $\sqrt{s} = 7$ TeV sample, $\sqrt{s} = 8$ TeV sample and the combination, separately. The observed p_0-values with diphoton mass scale uncertainties from pseudo-experiments are generally larger than those calculated from a likelihood model without diphoton mass scale uncertainties. Since the introduction of the diphoton mass scale uncertainties leads to a greater flexibility in the signal PDF, it is more likely to pick up fluctuations in pseudo-experiments, and thus it leads to a larger p_0-value. The introduction of diphoton mass scale uncertainties does not change the m_H value where the largest excess is observed.

Based on the likelihood model with diphoton mass scale uncertainties, the largest excess in the $\sqrt{s} = 7$ TeV sample has a p_0-value of 3.8 $\times 10^{-4}$, corresponding to 3.4 σ statistical significance, and the largest excess in the $\sqrt{s} = 8$ TeV sample has a p_0-value of 8.0 $\times 10^{-4}$, corresponding to 3.2 σ statistical significance, and the largest excess in the combined analysis has a p_0-value of 3.7 $\times 10^{-6}$, corresponding to 4.5 σ statistical significance. These p_0-values from a likelihood model incorporating diphoton mass scale uncertainties are considered to be the most accurate quantification of the excess and were reported in the Ref. [25]. In the results of the $\sqrt{s} = 7$ TeV sample, $\sqrt{s} = 8$ TeV sample and the combination, the observed significance is always larger than the expected significance at around $m_H = 126$ GeV. This suggests that the signal strength of the excess is larger than the SM expected value. Table 7.1 summarizes the p_0-value, significance and the corresponding m_H of the largest excesses observed in the $\sqrt{s} = 7$ TeV sample, $\sqrt{s} = 8$ TeV sample and the combination.

To estimate the *look elsewhere effect*, the average number of up-crossings (N_c) is calculated from pseudo-experiments and is found to be 3.3 at the reference level of $Z = 0$. The N_c value is found be essentially the same for the $\sqrt{s} = 7$ TeV sample, $\sqrt{s} = 8$ TeV sample and the combination. Using $N_c = 3.3$, the global significance is found to be 2.3 σ for the $\sqrt{s} = 7$ TeV sample, 2.0 σ for the $\sqrt{s} = 8$ TeV sample, and 3.6 σ for the combination. As the global significance of the excess at m_H = 126.5 GeV in the combination is as large as 3.6 σ, one can conclude this excess is statistically significant.

Table 7.1 The expected and observed p_0-values, statistical significances, and the best-fit signal strength at the m_H of the largest observed excess.

	m_H (GeV)	p_0-value		Significance		Signal strength
		observed	expected	observed	expected	μ
7 TeV	126	2.4×10^{-4}	5.3×10^{-2}	3.5 σ	1.6 σ	2.17 ± 0.75
8 TeV	127	4.8×10^{-4}	2.9×10^{-2}	3.2 σ	1.9 σ	1.74 ± 0.64
combined	126.5	1.7×10^{-6}	6.8×10^{-3}	4.6 σ	2.5 σ	1.84 ± 0.51

The local p_0-value and significance are also calculated for each individual category. Fig. 7.3 and Fig. 7.11 present the individual category's observed p_0-value (significance) as a function of m_H for the $\sqrt{s} = 7$ TeV and $\sqrt{s} = 8$ TeV samples, respectively.

The expected and observed statistical significances are also calculated using an "inclusive" analysis where the samples are not categorized. In the inclusive analysis, the events in$\sqrt{s} = 7$ TeV sample and $\sqrt{s} = 8$ TeV sample are separated to correctly assign the systematical uncertainties which may differ between two samples, i.e., the inclusive analysis still has two categories, one for $\sqrt{s} = 7$ TeV diphoton events and one for $\sqrt{s} = 8$ TeV diphoton events. The result is shown

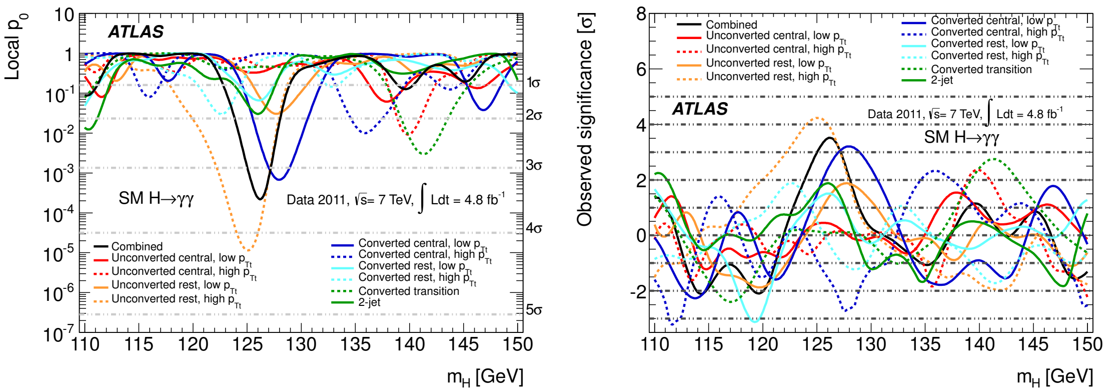

Figure 7.10 The observed local p_0-value for each individual category in the $\sqrt{s} = 7$ TeV sample(left), and the observed local significance for each individual category in the $\sqrt{s} = 7$ TeV sample(right).

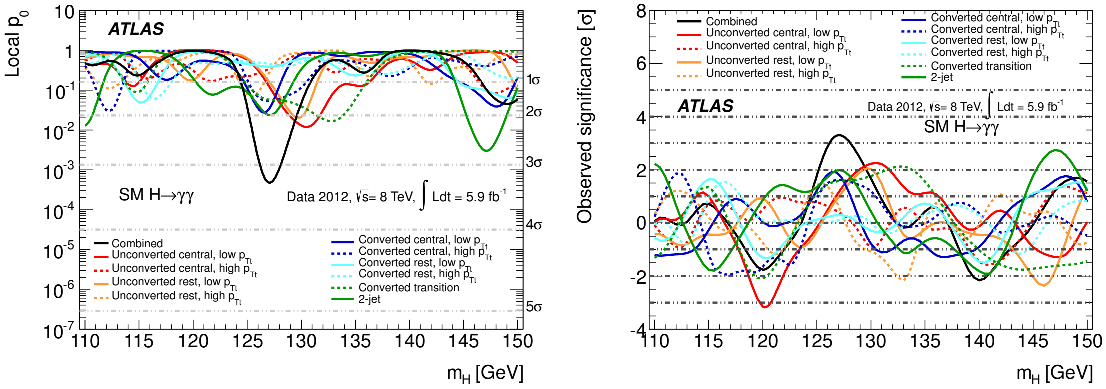

Figure 7.11 The observed local p_0-value for each individual category in the $\sqrt{s} = 8$ TeV sample(left), and the observed local significance for each individual category in the $\sqrt{s} = 8$ TeV sample(right).

in Fig. 7.12 and compared to the result from the category analysis. The expected significance of the inclusive analysis is lower compared to the category analysis as the category analysis is supposed be statistically more sensitive to signal. The observed significance of the inclusive analysis at $m_H = 126$ GeV is 3.3 σ, which also suggests the presence of an excess of events. In the inclusive analysis, the observed significance at $m_H = 126$ GeV is larger than the expected significance, indicating that the signal strength observed from the inclusive analysis is also larger than the SM expectation. The observed significance in the inclusive analysis is lower than the observed significance in the category analysis, which is consistent with the expectation.

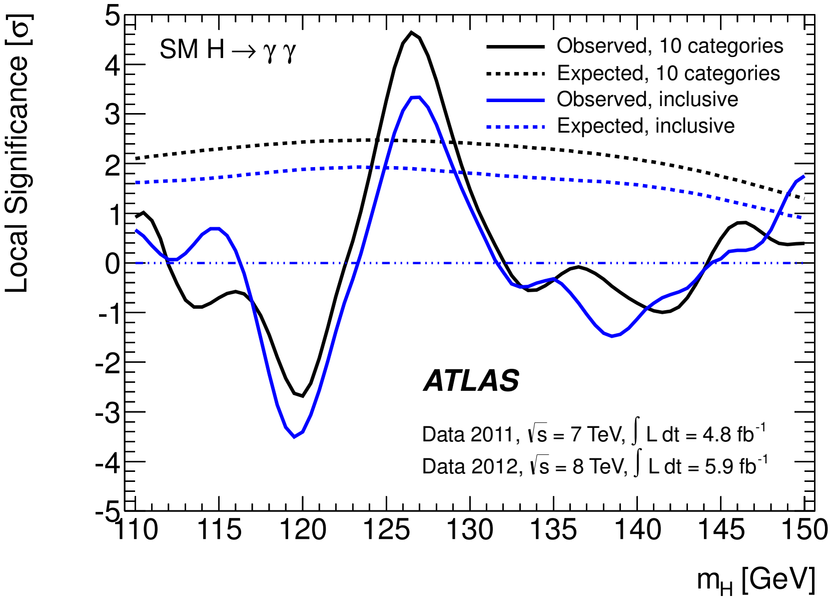

Figure 7.12 Observed and expected local significances obtained with the analysis using the inclusive category, compared with the result using the ten categories, for the combined $\sqrt{s} = 7$ TeV and $\sqrt{s} = 8$ TeV data samples.

The improvement that the categorization introduces to the analysis can be also visualized by drawing the $m_{\gamma\gamma}$ distribution with weighted diphoton events, as shown in Fig. 7.13. To plot this distribution, each event is assigned a weight that is the ln(1+S/B) of the category to which the event belongs. The excess at around m$_{\gamma\gamma} \sim 126.5$ GeV is considerably more visible in Fig. 7.13 compared to that in Fig. 7.6

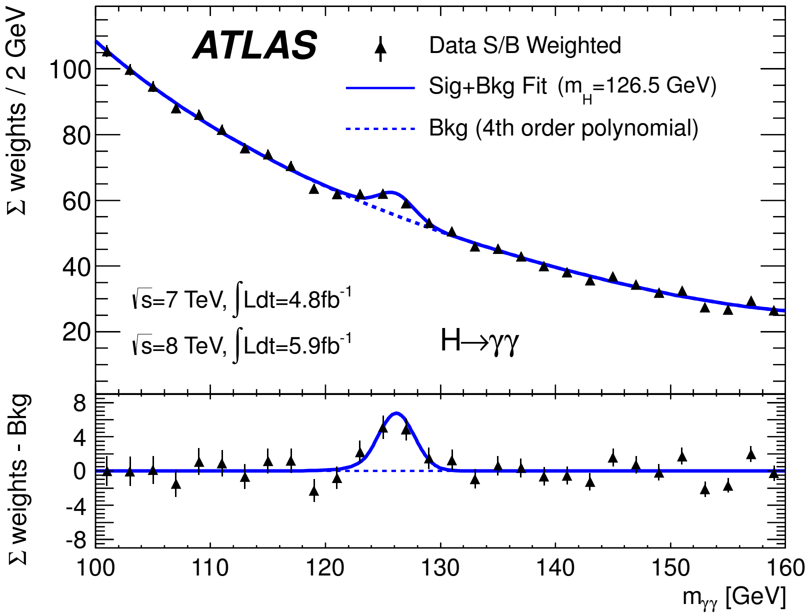

Figure 7.13 The weighted distribution of invariant mass of diphoton candidates for the combined $\sqrt{s} = 7$ TeV and $\sqrt{s} = 8$ TeV data samples. The weight w_i for category i from $[1, 10]$ is defined to be $ln(1 + \frac{S_i}{B_i})$, where S_i is 90% of the expected signal for m_H = 126.5 GeV, and Bi is the integral, in a window containing S_i, of a background-only fit to the data. The values S_i/B_i have only a mild dependence on m_H. The result of a fit to the data of the sum of a signal component fixed to m_H = 126.5GeV and a background component described by a fourth-order Bernstein polynomial is superimposed. The bottom inset displays the residuals of the data with respect to the fitted background component.

7.4 Signal strength

The best-fit signal strength is calculated for the $\sqrt{s} = 7$ TeV sample, the $\sqrt{s} = 8$ TeV sample, and their combination. Fig. 7.4 shows the best-fit signal strength results from the 7 TeV and 8 TeV samples, and Fig. 7.14 shows the best fit signal strength for the combined analysis.

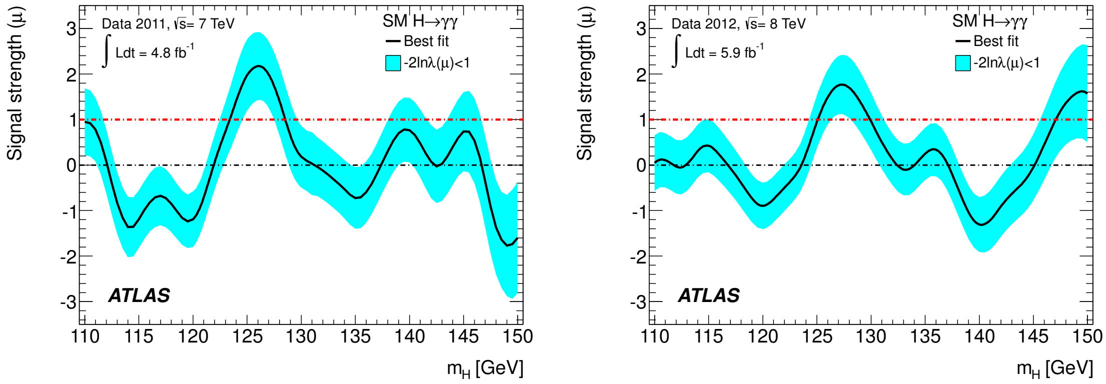

Figure 7.14 Best fit value for the signal strength as a function of the assumed Higgs boson mass for the $\sqrt{s} = 7$ TeV (left) and $\sqrt{s} = 8$ TeV (right) analyses.

Over the range of 110 GeV $< m_H <$ 150 GeV, the observed best-fit signal strength fluctuates around $\mu = 0$, reflecting the statistical fluctuations in data. In the region around $m_H = 126$ GeV, there is an upward deviation from $\mu = 0$ in all of the $\sqrt{s} = 7$ TeV sample, $\sqrt{s} = 8$ TeV sample and their combination. The right plot in Fig. 7.15 also presents an "injection" test: the signal strength is measured from a pseudo-dataset that is in perfect agreement with a SM Higgs at m_H 126.5 GeV signal-plus-background hypothesis. The observed best-fit signal strength curve from the artificial data behaves similarly to the observed curve from the real data at around m_H 126.5 GeV. One

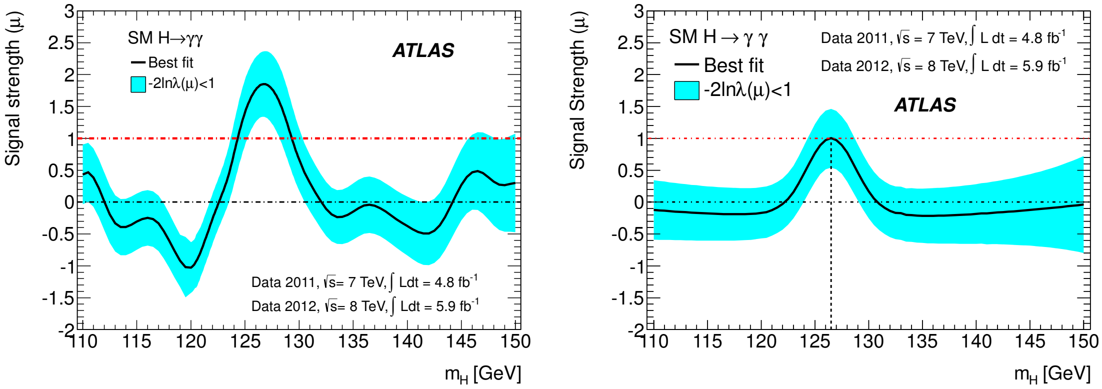

Figure 7.15 Best fit value for the signal strength as a function of the assumed Higgs boson mass for the combined analysis (left). The expected signal strength as a function of m_H when a SM Higgs boson signal with m_H = 126.5 GeV is injected (right).

feature in both plots of Fig. 7.15 is that on the two sides of the excess region ($m_H \sim 126$ GeV), the best-fit signal strengths are negative. As shown in the injection test plot, this is a feature of the fit machinery. When a real excess is present in data, the background expectation for $m_H \sim$ 120 GeV or 133 GeV is lifted by the excess at around $m_H = 126$ GeV, leading to a negative fitted signal strength. The observed best-fit signal strengths at the m_H of the largest excesses for the three analyses are summarized in Table 7.2.

The best-fit signal strength is also evaluated for all 20 individual categories to help understand each category's contribution to the excess observed in the individual year's analysis and the combined analysis. Fig. 7.4 summarizes the best-fit signal strength for individual categories at m_H= 126.5 GeV, and Fig. 7.4 summarizes the best-fit signal strength from a combination of the same category in two years' samples.

Table 7.2 The observed best-fit signal strengths at $m_H = 126$ GeV, 126.5 GeV and 127 GeV for the $\sqrt{s} = 7$ TeV sample, $\sqrt{s} = 8$ TeV sample and the combination.

Analysis	m_H (GeV)		
	126	126.5	127
7 TeV	2.2 ± 0.8	2.1 ± 0.7	2.0 ± 0.7
8 TeV	1.5 ± 0.6	1.7 ± 0.6	1.8 ± 0.6
combination	1.8 ± 0.5	1.8 ± 0.5	1.8 ± 0.5

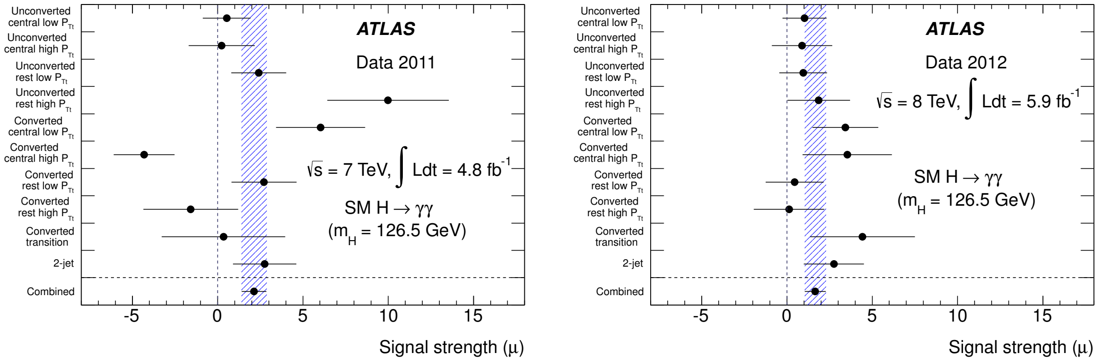

Figure 7.16 Best fit value for the signal strength in the different categories at m_H = 126.5 GeV for the $\sqrt{s} = 7$ TeV (left) and the $\sqrt{s} = 8$ TeV (right) data sample. The blue band corresponds to the error of the combined result.

7.5 Measurement of the mass of the excess

As the “search” for a SM Higgs boson in the diphoton final state is carried out with limited granularity in m_H, the $m_H = 126.5$ GeV where the largest excess is observed in the combination is not necessarily the mass of the excess. To best determine the mass of the particle responsible for

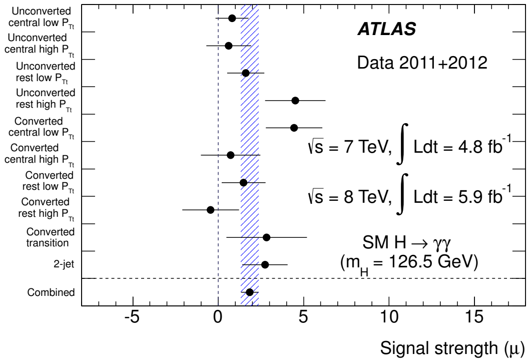

Figure 7.17 Best-fit signal strength from a combination of the same category in two years' samples.

the observed excess, a dedicated mass measurement needs to be performed with a profile likelihood ratio of m_H.

In the mass measurement test statistic, the m_H is the parameter of interest, and the signal strength μ is treated as a nuisance parameter. Following the procedure described in Sec. 6.2.5.3, profile likelihood ratio scans on m_H are performed for the $\sqrt{s} = 7$ TeV sample, $\sqrt{s} = 8$ TeV sample and their combination, and these scan curves are shown in Fig. 7.18. The minima in these curves correspond to the best-fit m_H values, and the uncertainties of these measurements are determined by the m_H values that deviates from the minimum m_H by $-2\Delta ln\lambda(m_H) = 1$.

The measured mass from the $\sqrt{s} = 7$ TeV sample is found to be:

$$m_H = 126.2 \pm 0.55(stat) \pm 0.58(syst)\ GeV, \tag{7.1}$$

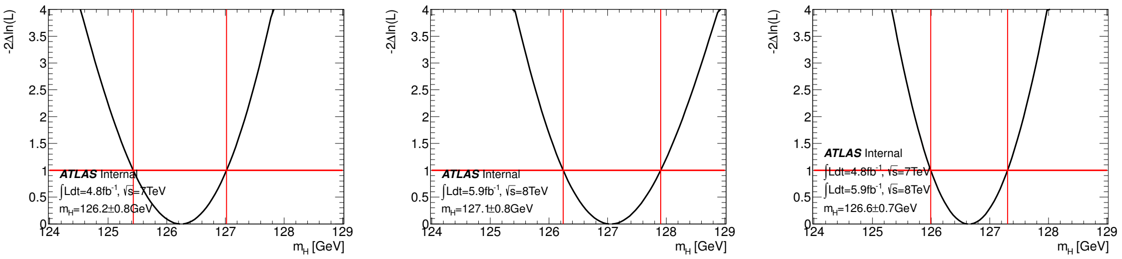

Figure 7.18 The profile likelihood ratio $-2ln\lambda(m_H)$ curves for the $\sqrt{s} = 7$ TeV sample, $\sqrt{s} = 8$ TeV sample and the combination.

and the measured mass from the $\sqrt{s} = 8$ TeV sample is found to be:

$$m_H = 127.1 \pm 0.65(stat) \pm 0.51(syst)\ GeV \tag{7.2}$$

The measured mass from the combination is:

$$m_H = 126.6 \pm 0.41(stat) \pm 0.51(syst)\ GeV \tag{7.3}$$

Fig. 7.19 shows a two dimensional measurement of m_H and μ where the best-fit values of m_H and μ from a simultaneous fit are shown. Multiple uncertainty contours are also plotted in Fig. 7.19 to show the impact of the systematical uncertainties on the measurement of m_H and μ. The removal of the diphoton mass scale uncertainties from the measurement squeezes the uncertainty contours horizontally, and the removal of uncertainties on the signal yield and the diphoton mass resolution uncertainty squeezes the uncertainty contours vertically. These changes and the orientation of the contours suggest that the measurement of m_H and the measurement of μ are not strongly correlated.

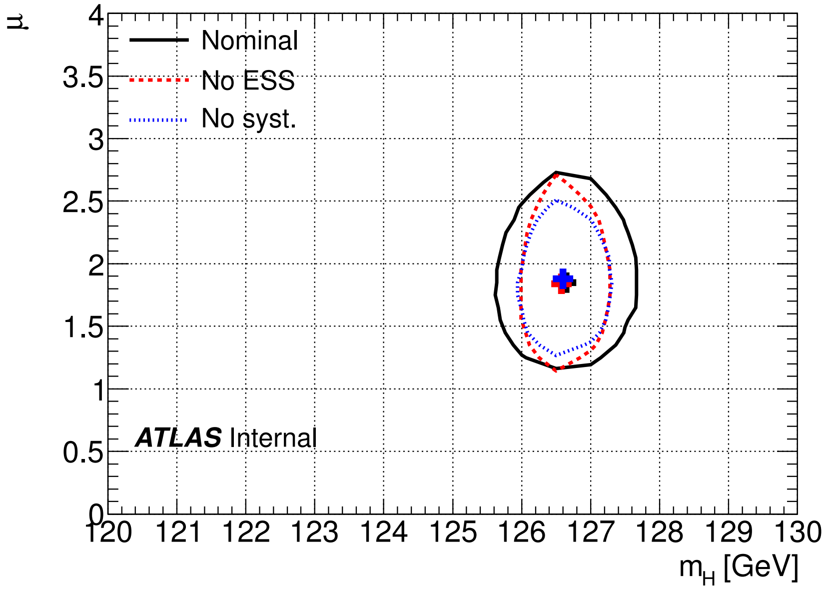

Figure 7.19 Confidence interval contours for the $H \rightarrow \gamma\gamma$ channel in the (μ, m_H) plane. The 68% CL contours for the case where all systematic uncertainties are included (solid black), the case where the diphoton mass scale uncertainty is removed (dashed red), and the case where all systematic uncertainties are removed (dashed blue), are shown.

7.6 Observation of excess in other channels and the combined Higgs boson searches

As reported in Ref. [25], the 4.8 fb^{-1} $\sqrt{s} = 7$ TeV data and 5.9 fb^{-1} $\sqrt{s} = 8$ TeV data collected by the ATLAS experiment are also analyzed for the search for the SM Higgs boson decaying to ZZ in the 4-lepton final state and the search for the SM Higgs boson decaying to WW in the $l\nu l\nu$

final state. Fig. 7.20 [25] shows the observed p_0-values in the 4-lepton analysis, $\gamma\gamma$ analysis and the $l\nu l\nu$ analysis. The largest excess observed in the 4-lepton final state is found to be 3.6 σ at $m_H = 125$ GeV, and the largest excess observed in the $l\nu l\nu$ final state is found to be 2.8 σ at $m_H = 125$ GeV [25]. The $H \rightarrow \gamma\gamma$, $H \rightarrow ZZ^{(*)} \rightarrow 4l$ and $H \rightarrow WW^{(\star)} \rightarrow l\nu l\nu$ analyses are combined with the searches for the SM Higgs boson in $b\bar{b}$ and $\tau\tau$ final states from the ATLAS experiment [100]. Fig. 7.21 [25] shows the p_0-value as a function of m_H from the combination of SM Higgs boson searches. The combined analysis shows clear and convincing evidence for the production of a neutral boson with a measured mass of 126.0 ± 0.4 (stat) ± 0.4 (sys) GeV. This observation has a local statistical significance of 5.9 σ, corresponding to a p_0-value of 1.7×10^{-9}. Fig. 7.22 [25] shows the best-fit signal strength values from all five SM Higgs boson searches and the combined search at $m_H = 126$ GeV. The best-fit signal strength from the combination is 1.4 ± 0.3 at $m_H = 126$ GeV

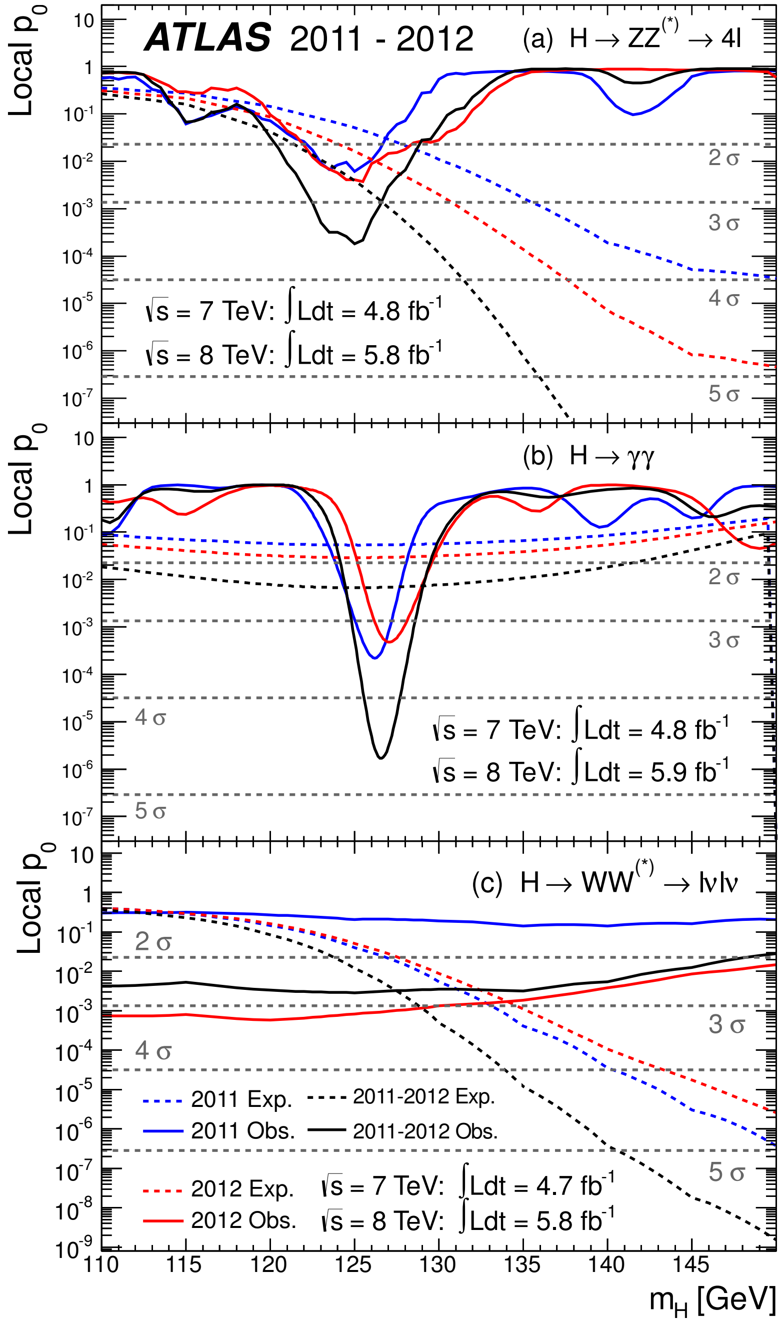

Figure 7.20 The observed local p_0 as a function of the hypothesized Higgs boson mass for the (a) $H \rightarrow ZZ^{(*)} \rightarrow 4l$, (b) $H \rightarrow \gamma\gamma$ and (c) $H \rightarrow WW^{(\star)} \rightarrow l\nu l\nu$ channels. The dashed curves show the expected local p_0 under the hypothesis of a SM Higgs boson signal at that mass. Results are shown separately for the $\sqrt{s} = 7$ TeV data (dark blue), the $\sqrt{s} = 8$ TeV data (light red), and their combination (black).

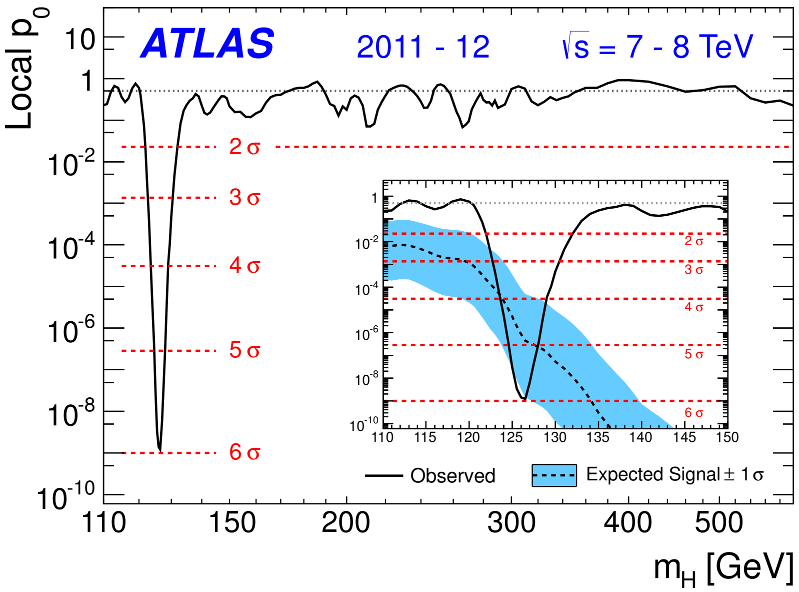

Figure 7.21 The local probability p_0 for a background-only experiment to be more signal-like than the observation as a function of m_H reported (cover) in Phys. Lett. B 716 (2012) 1-29. The dashed curve shows the median expected local p_0 under the hypothesis of a Standard Model Higgs boson production signal at that mass. The horizontal dashed lines indicate the p-values corresponding to significances of 1 σ to 6 σ.

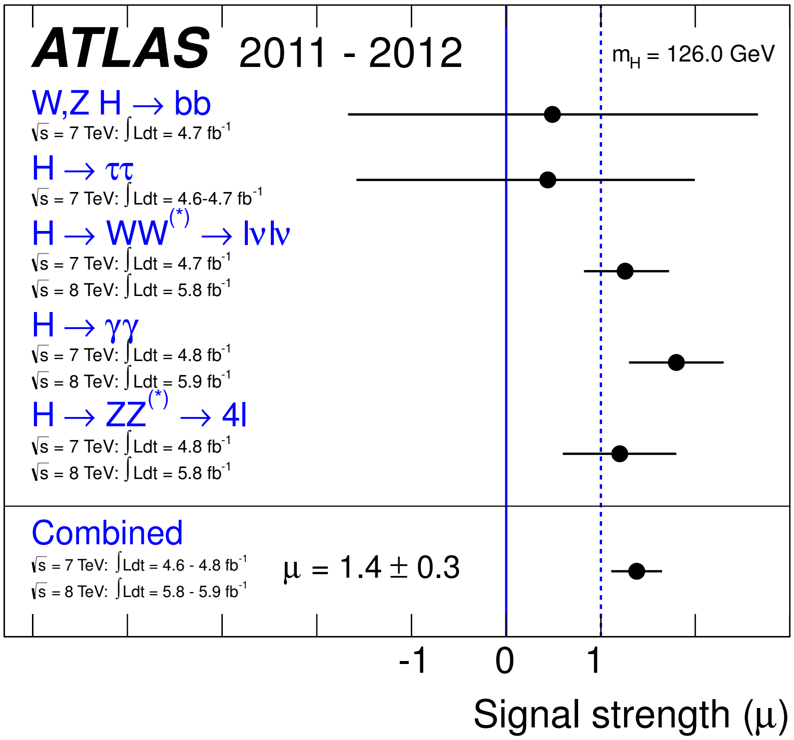

Figure 7.22 Measurements of the signal strength parameter μ for $m_H = 126$ GeV for the individual channels and their combination.

Chapter 8

Measurement of the properties of the newly observed boson

8.1 Overview

This chapter presents measurements of the new particle's mass, signal strength and the signal strengths of major production modes in the $H \to \gamma\gamma$ channel. A comprehensive measurement of the properties of this new particle should be performed with a combination of information provided by all relevant Higgs boson decay channels. Nevertheless, measurements in the $H \to \gamma\gamma$ channel are important building blocks of the combined measurement. These measurements are performed with 4.8 fb^{-1} data at $\sqrt{s} = 7$ TeV and 20.7 fb^{-1} data at $\sqrt{s} = 8$ TeV. The $\sqrt{s} = 8$ TeV part of the analysis is changed with respect to the one presented in Chapeter. 5. The new categorization of the $\sqrt{s} = 8$ TeV sample is introduced in Sec. 8.2. Sec. 8.3 describes the systematical uncertainties used for the $\sqrt{s} = 8$ TeV part of the "measurement" analysis. Sec. 8.4 presents the $m_{\gamma\gamma}$ distributions for the 14 categories of diphoton events of $\sqrt{s} = 8$ TeV defined in the measurement analysis. Sec. 8.5 reports the statistical significance of the excess in the full data sample. In Sec. 8.6, the measurement of the new particle's mass with the full data samples is presented. In

Sec. 8.7, the measurement of the new particle's signal strength with the full data samples is presented. In Sec. 8.8, the measurement of the strength parameters for individual production modes with the full data samples is presented. Sec. 8.9 reports the major measurements performed in the combination of the $H \to \gamma\gamma$, $H \to ZZ^{(\star)} \to 4l$ and $H \to WW^{(\star)} \to l\nu l\nu$ channels and also the measurement relevant to the $H \to \gamma\gamma$ channel.

8.2 The "measurement" analysis

Since the discovery of the new particle in July, 2012, changes have been made to the analysis of 8 TeV data in order to improve the sensitivity to individual production modes, in particular, the VBF and VH production modes. Three categories that cover the leptonic, hadronic and invisible decay final states of the weak boson in the VH signals are introduced. The high mass 2-jet selection in the $\sqrt{s} = 8$ TeV sample is re-optimized with a multivariate discriminant, and now the high mass 2-jet category is split into two categories. The p_{Tt}-η-conversion categories that constrain the normalization of ggF production are kept the same as the "search" analysis.

8.2.1 VH categories

For $m_H \sim 125$ GeV, approximately 5% of Higgs bosons produced at the LHC come from VH production, of which 3% are WH production and 2% are ZH production. With 20.7 fb^{-1} data at $\sqrt{s} = 8$ TeV, the expected number of VH signal events is ~ 4.2 after the diphoton event selection. The presence of a weak boson in the $H \to \gamma\gamma$ event provides additional discriminating variable to suppress background events and also unique event topologies to separate VH signal events from signal events produced from other production modes.

Three event topologies are considered for categorizing diphoton events:

- Diphoton events with at least one additional lepton. Such events mainly come from WH/ZH signal where the weak boson decays leptonically. In principle, additional requirements on E_T^{miss} or the presence of a second lepton with the same flavor and opposite charge can be added. However, the number of events after the one-lepton requirement is very low. Further applying topological cuts increases the S/B at a cost of losing statistical power.

- Diphoton events with large missing transverse energy (E_T^{miss}). Such events primarily come from the ZH signal where the Z boson decays to neutrinos. Events from the WH signal where W decays leptonically can also be selected if the lepton is a τ lepton or not properly reconstructed in the event.

- Diphoton events with two additional jets where the characteristics of the two jets are consistent with those of two jets decaying from a weak boson. Specifically, the invariant mass of the dijet system should be close to W boson mass and Z boson mass; these two jets should not be widely separated in pseudo-rapidity. In addition, the diphoton system should be boosted.

The categories selecting such VH event topologies are described below.

8.2.1.1 One lepton category

This category is defined to select VH signal events where the vector boson decays leptonically. The diphoton events must have at least one lepton. If the additional letpon is an electron, two more requirements are applied to reject the contamination from $Z \rightarrow e^{+}e^{-}$ events. First, the invariant mass of the electron and any of the two leading photons should not be in the window between 84 GeV and 94 GeV; second, neither of the two photons should be matched to an electron candidate that passes the electron identification selection.

8.2.1.2 E_T^{miss} significance category

The E_T^{miss} significance of the diphoton events must be greater than 5. To reject diboson backgrounds, it is required that neither of the two photons is matched to an electron candidate that passes the electron identification selection.

8.2.1.3 Low mass two-jet category

This category is defined to select the VH events where the vector boson decays hadronically. The diphoton events are required to have two additional jets. The pseudo-rapidity separation between the two jets, $|\Delta\eta_{jj}|$, must be less than 3.5, and the invariant mass of the two jets must be between 60 GeV and 110 GeV. The difference in pseudo-rapidity between the diphoton system and dijet system, $\Delta\eta_{\gamma\gamma,jj}$, must be less than 1. The p_{Tt} of diphoton system must be larger than 70 GeV.

8.2.2 High mass two-jet (VBF-enriched) categories

The “measurement” analysis uses a Boost-Decison-Tree (BDT) [101] based multivariate discriminant to define two high mass two-jet categories, one with more stringent requirements on the multivariate discriminant and one with looser requirement.

This BDT discriminant is built with the following variables: $\Delta\eta_{jj}$, the pseudo-rapidity gap between the two jets, m_{jj}, the invariant mass of the dijet system, η_{j1}, the pseudo-rapidity of the leading jet, η_{j2}, the pseudo-rapidity of the subleading jet, $\Delta\phi_{\gamma\gamma,jj}$, the difference in ϕ direction between the diphoton system and the dijet system, p_{Tt} of the diphoton system, $\eta^* = \eta_{\gamma\gamma} - \frac{\eta_{j1}+\eta_{j2}}{2}$, the difference between the pseudo-rapidity of the diphoton system and the average pseudo-rapidity of the two jets [102], and the minimal $\Delta R_{\gamma,jet}$ of any possible combination of photon and jet.

In the training of the BDT discriminant, the vector boson fusion Higgs boson sample at $m_H =$ 125 GeV is used as the signal sample, and a combination of Monte Carlo sample and data control sample is used as the background sample. The irreducible $\gamma\gamma$ background is modeled by the SHERPA Monte Carlo, and the reducible backgrounds of γ-jet and multi-jets are modeled by a data control region that is defined as a sample of diphoton events where at least one photon candidate fails the isolation requirement. The irreducible and reducible backgrounds are normalized to their fractions determined from a data driven method [70, 71].

The BDT response distributions from vector boson fusion signal, gluon fusion signal and background samples are shown in Fig. 8.1. The BDT response not only provides discriminating power for vector boson fusion signal events over background events, but also provides separation power between the VBF signal events and the ggF signal events. This variable is used to define high mass 2-jet categories in the "measurement" analysis.

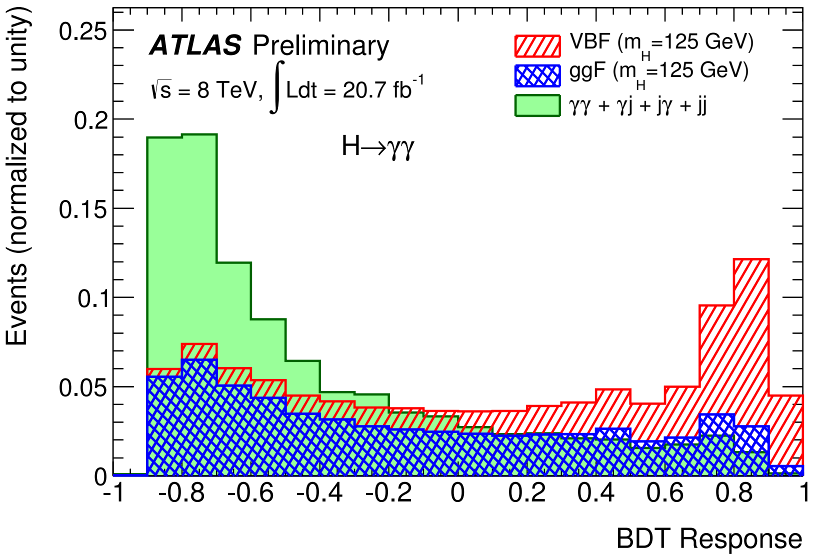

Figure 8.1 The response of the VBF BDT to the VBF signal sample, to the ggF signal sample, and to the expected background after selection cuts,

The BDT response distributions from background Monte Carlo sample and data sample are compared in Fig. 8.2. Due to the low S/B of the $\gamma\gamma$+2 jets sample, the data distribution can be seen as dominated by background events, and hence is compared to the distribution of background Monte Carlo sample. There is a reasonably good agreement between the two distributions, which indicates that the training is likely to be optimal because the background is well modeled by the Monte Carlo samples. It is also noteworthy that the extent to which the two distributions agree does not play a role in the analysis because the background expectation at a hypothesized Higgs boson mass is determined by a fit of $m_{\gamma\gamma}$ distributions and does not depend on the prediction from the background Monte Carlo sample.

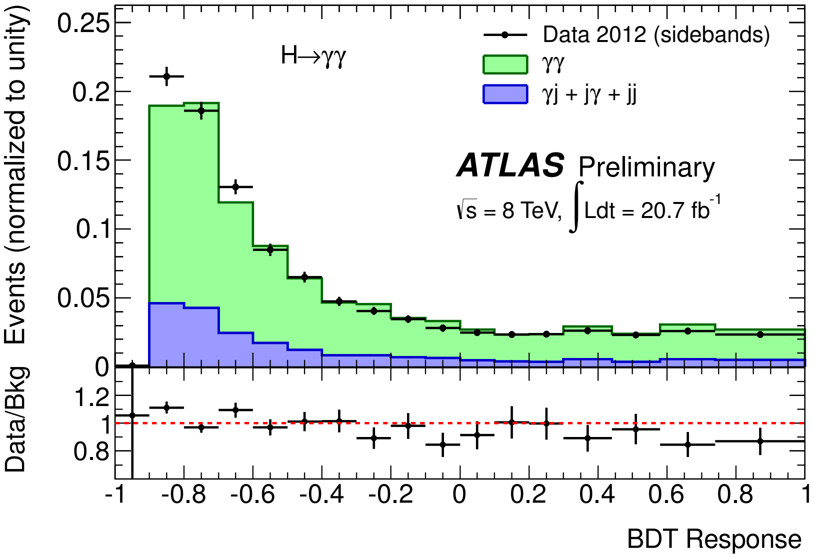

Figure 8.2 The response of the VBF BDT to the data in the signal sidebands (excluding the $m_{\gamma\gamma}$ in [120-130] GeV region) and to the expected background after selection cuts, normalized to unity.

8.2.2.1 Two-jet BDT loose and tight categories

Two categories are defined by the BDT response described in Sec. 8.2.2 to select VBF signal events. First, a tight high mass 2-jet category is defined by requiring the BDT response be larger than 0.74 in the diphoton events. Then, a loose high mass 2-jet category is defined by requiring the BDT response be between 0.44 and 0.74.

8.2.3 Summary information of the 14 categories of the 8 TeV sample

Table 8.1 summarizes the signal mass resolution, number of observed events, number of expected signal events (N_S), number of expected background events (N_B), and signal to background ratio (N_S/N_B) in a mass window around $m_H = 126.5$ GeV (containing 90% of the expected signal events) in each category and the inclusive sample for the "measurement" analysis. Event yield information in Table 8.1 is normalized to 20.7 fb^{-1}.

The expected number of signal events normalized to the integrated luminosity and the fraction of each production mode in each category are shown in Table 8.2. The highest fraction of VH signal events is found to be $\sim 82\%$ in the E_T^{miss} category, followed by the one-lepton category that gives a VH fraction of $\sim 78\%$. The VH signal fraction is $\sim 48\%$ in the low mass two-jet category, noticeably higher than that in the p_{Tt}-η-convserion categories and high mass 2-jet categories.

8.3 Systematic uncertainties for the "measurement" analysis

For most systematic uncertainties, the treatment and estimation method follow are the same as those used for the "search" analysis.

8.3.1 Yield uncertainty

- **Luminosity uncertainty.** The 2011 luminosity uncertainty is 1.8% and the 2012 luminosity uncertainty is 3.6% [79].

- **Trigger efficiency uncertainty.** The trigger efficiency uncertainty is 0.5% per event.

Table 8.1 Signal mass resolution (σ_{CB}), number of observed events, number of expected signal events (N_S), number of expected background events (N_B) and signal to background ratios (N_S/N_B) in a mass window around $m_H = 126.5$ GeV containing 90% of the expected signal for each of the 14 categories of the $\sqrt{s} = 8$ TeV data analysis. The numbers of background events are obtained from the background + signal fit to the $m_{\gamma\gamma}$ data distribution.

$\sqrt{s}$	8 TeV				
Category	$\sigma_{CB}(\,GeV)$	Observed	N_S	N_B	N_S/N_B
Unconv. central, low p_{T_t}	1.50	911	46.6	881	0.05
Unconv. central, high p_{T_t}	1.40	49	7.1	44	0.16
Unconv. rest, low p_{T_t}	1.74	4611	97.1	4347	0.02
Unconv. rest, high p_{T_t}	1.69	292	14.4	247	0.06
Conv. central, low p_{T_t}	1.68	722	29.8	687	0.04
Conv. central, high p_{T_t}	1.54	39	4.6	31	0.15
Conv. rest, low p_{T_t}	2.01	4865	88.0	4657	0.02
Conv. rest, high p_{T_t}	1.87	276	12.9	266	0.05
Conv. transition	2.52	2554	36.1	2499	0.01
Loose High-mass two-jet	1.71	40	4.8	28	0.17
Tight High-mass two-jet	1.64	24	7.3	13	0.57
Low-mass two-jet	1.62	21	3.0	21	0.14
E_T^{miss} significance	1.74	8	1.1	4	0.24
One-lepton	1.75	19	2.6	12	0.20
Inclusive	1.77	14025	355.5	13280	0.03

- **Photon identification efficiency uncertainty.** The uncertainty of photon identification efficiency in the $\sqrt{s} = 8$ TeV sample is reduced to 2.4%.

- **Isolation efficiency uncertainty.** The isolation efficiency uncertainty is estimated to be 1% per event.

Table 8.2 Fraction of expected signal events per category at $m_H = 126.5$ GeV and $\sqrt{s} = 8$ TeV and the breakdown by production process.

Category	Events	$gg \to H$ [%]	VBF [%]	WH [%]	ZH [%]	ttH [%]
Unconv. central, low p_{T_t}	51.8	93.7	4.0	1.4	0.8	0.2
Unconv. central, high p_{T_t}	7.9	79.3	12.6	4.1	2.5	1.4
Unconv. rest, low p_{T_t}	107.9	93.2	4.0	1.6	1.0	0.1
Unconv. rest, high p_{T_t}	16.0	78.1	13.3	4.7	2.8	1.1
Conv. central, low p_{T_t}	33.1	93.6	4.0	1.3	0.9	0.2
Conv. central, high p_{T_t}	5.1	78.9	12.6	4.3	2.7	1.5
Conv. rest, low p_{T_t}	97.8	93.2	4.1	1.6	1.0	0.1
Conv. rest, high p_{T_t}	14.4	77.7	13.0	5.2	3.0	1.1
Conv. transition	40.1	90.7	5.5	2.2	1.3	0.2
Loose high-mass two-jet	5.3	45.0	54.1	0.5	0.3	0.1
Tight high-mass two-jet	8.1	23.8	76.0	0.1	0.1	0.0
Low-mass two-jet	3.3	48.1	3.0	29.7	17.2	1.9
E_T^{miss} significance	1.3	4.1	0.5	35.7	47.6	12.1
One-lepton	2.9	2.2	0.6	63.2	15.4	18.6
All categories (inclusive)	395.0	88.0	7.3	2.7	1.5	0.5

- **Diphoton selection efficiency uncertainty due to the photon energy scale uncertainty.** The uncertainty of diphoton event selection introduced by the photon energy scale uncertainty is estimated to be 0.25%.

- **Theoretical uncertainties on cross section and branching ratio.** These uncertainties are treated in the same way as the “search” analysis.

- **The QCD scale uncertainty on the ggF cross section in jet bins** The uncertainty resulted from missing higher order calculations has been estimated with a new method [103], based on the MCFM [104] calculation. The new procedure estimates the uncertainty on ggF cross section by studying the variation in the distribution of the infrared sensitive variable $\Delta\phi_{\gamma\gamma,jj}$ after the high mass 2-jet categories' selection. The resulting uncertainty on the ggF signal yield is found to be 48% in the tight high mass 2-jet category and 28% in the loose high mass 2-jet category. For the low mass 2-jet category, the uncertainty on the ggF yield is evaluated from MCFM and found to be 30%.

- **The material mis-modeling uncertainty.** This uncertainty is not changed with respect to the "search" analysis.

- **The p_{T_t} categorization uncertainty due to uncertainty on the Higgs boson p_T modeling.** The estimation procedure is not changed with respect to the "search" analysis and it is applied to the new categorization. The uncertainty is found to be 1.3% on the low-p_{T_t} categories, 10.2% on the high-p_{T_t} categories, 10.4% on the tight high mass 2-jet category, 8.5% on the loose high mass 2-jet category, 2.0% on the E_T^{miss} significance category and 4.0% on the one-lepton category.

- **The jet energy scale uncertainty.** The jet energy scale uncertainty is about 11.8% (10.7%) for the tight high mass (loose) 2-jet category, 6.7% for the low mass 2-jet category, and 0.7% for other categories.

- **The jet energy resolution uncertainty.** The jet energy resolution uncertainty is found to be 3.8% (3.4%) on the tight high mass (loose) 2-jet category, 3.4% on the low mass 2-jet category and 0.9% on all other categories.

- **The underlying event uncertainty** The uncertainty resulted from the modeling of underlying event is estimated by comparing the event yields and distributions in simulation samples with and without multi-parton interaction (MPI). The default underlying event tune used for the Monte Carlo sample is the AU2-CT10 [105]. This uncertainty mainly affects the 2-jet categories and is found to be 8.8% on the ggF, VH and ttH normalizations in the tight high mass 2-jet category, and 2% on the VBF normalization in the tight high mass 2-jet category, 12.8% on the ggF, VH and ttH normalizations in the loose high mass 2-jet category, and 3.3% on the VBF normalization in the loose high mass 2-jet category, 12% on the ggF, VH and ttH normalizations in the low mass 2-jet category, and 3.9% on the VBF normalization in the low mass 2-jet category.

- **The systematical uncertainty on the modeling of the $\Delta\phi_{\gamma\gamma,jj}$ distribution.** This is a new uncertainty as the training of the BDT discriminant uses the $\Delta\phi_{\gamma\gamma,jj}$ variable as one of the inputs. The $\Delta\phi_{\gamma\gamma,jj}$ of the ggF signal is modeled by POWHEG at NLO QCD accuracy. The POWHEG distributions are reweighted to those from LO SHERPA sample with matrix element matching for up to three patrons in the final state. The resulting variation in the ggF signal yields in the high mass 2-jet categories is taken as the uncertainty. This uncertainty is found to be 12.1% (8.5%) for the tight high mass (loose) 2-jet category.

- **The systematical uncertainty on the modeling of the $\eta^\star$ distribution.** This uncertainty also arises from the training of BDT discriminant. The jet distributions from the POWHEG ggF signal sample are reweighted to those from MCFM. The resulting variation in the ggF signal yield in the high mass 2-jet categories is taken as the uncertainty. This uncertainty is found to be 7.6% (6.2%) for the tight high mass (loose) 2-jet category.

- **The jet-vertex-fraction uncertainty.** The JVF uncertainty is found to be 0.3% (0.2%) for ggF (VBF) in the loose high mass 2-jet category, and 2.3% (2.4%) for ggF (VBF) in the low mass 2-jet category.

- **The uncertainties on the electron and muon reconstruction efficiency.** The electron reconstruction and identification efficiency uncertainty is found to be less than 1% on the VH and ttH signal yields in the one-lepton category. The uncertainty on the VH and ttH signal yields in the one-lepton category from the electron energy scale and resolution uncertainties is found to be less than 1% on the VH and ttH signal yields in the one-lepton category. The uncertainty on the VH and ttH signal yields in the one-lepton category from the muon reconstruction efficiency uncertainty and tracker resolution uncertainty is found to be less than 1%.

- E_T^{miss} uncertainties. The E_T^{miss} uncertainties are estimated by shifting the transverse energy of each contributing object in the reconstruction of E_T^{miss} up and down within their respective uncertainties. The resulting uncertainty on the signal yields in the E_T^{miss} significance category is 66.4% for the ggF signal, 30.7% for the VBF signal, and 1.2% for the VH and ttH signal.

8.3.2 Diphoton mass resolution and scale systematic uncertainties

Resolution uncertainty. Additional uncertainty is assigned to cover the observed difference in the $Z \to ee$ shape between data and MC. This leads to a total $m_{\gamma\gamma}$ resolution uncertainty between 14% and 23% depending on the category.

The diphoton mass scale uncertainties. The diphoton mass scale uncertainties are re-evaluated and summarized in Table 8.3. In addition, about 0.35% mass scale uncertainty due to the potential mis-modeling of the background is identified and assigned to all categories as a correlated mass scale uncertainty.

Table 8.3 2012 uncertainty on peak position due to energy scale uncertainties, in different categories

Category	Method	Material low η ($\|\eta\| < 1.8$)	Material high η ($\|\eta\| > 1.8$)	Presampler Barrel	Presampler *Endcap*
Inclusive	$\pm0.34\%$	$\pm0.39\%$	$\pm0.06\%$	$\pm0.10\%$	$\pm0.01\%$
Unconverted Central Low-p_{T_t}	$\pm0.30\%$	$\pm0.26\%$	-	$\pm0.10\%$	-
Unconverted Central High-p_{T_t}	$\pm0.31\%$	$\pm0.26\%$	-	$\pm0.11\%$	-
Unconverted Rest Low-p_{T_t}	$\pm0.35\%$	$\pm0.47\%$	$\pm0.10\%$	$\pm0.16\%$	$\pm0.02\%$
Unconverted Rest High-p_{T_t}	$\pm0.35\%$	$\pm0.49\%$	$\pm0.08\%$	$\pm0.18\%$	$\pm0.01\%$
Converted Central Low-p_{T_t}	$\pm0.31\%$	$\pm0.19\%$	-	$\pm0.03\%$	-
Converted Central High-p_{T_t}	$\pm0.31\%$	$\pm0.20\%$	-	$\pm0.07\%$	-
Converted Rest Low-p_{T_t}	$\pm0.35\%$	$\pm0.31\%$	$\pm0.09\%$	$\pm0.05\%$	-
Converted Rest high-p_{T_t}	$\pm0.35\%$	$\pm0.39\%$	$\pm0.11\%$	$\pm0.08\%$	-
Converted Transition	$\pm0.38\%$	$\pm0.71\%$	$\pm0.07\%$	$\pm0.05\%$	$\pm0.06\%$
loose high mass 2-jet	$\pm0.33\%$	$\pm0.41\%$	$\pm0.07\%$	$\pm0.10\%$	-
tight high mass 2-jet	$\pm0.33\%$	$\pm0.38\%$	$\pm0.03\%$	$\pm0.13\%$	-
Low Mass 2-jet	$\pm0.33\%$	$\pm0.43\%$	$\pm0.06\%$	$\pm0.12\%$	-
E_T^{miss} significance	$\pm0.34\%$	$\pm0.39\%$	$\pm0.05\%$	$\pm0.12\%$	-
One-lepton	$\pm0.34\%$	$\pm0.40\%$	$\pm0.07\%$	$\pm0.10\%$	-

8.3.3 The background $m_{\gamma\gamma}$ modeling uncertainty

The background function selection procedure is performed for all 14 categories of the "measurement" analysis and the background modeling uncertainty is also evaluated for the 14 chosen background functions. Table 8.4 summarizes the selected background function and the assigned modeling uncertainty in the unit of number of events.

8.4 The diphoton invariant mass distributions with 20.7 fb^{-1} $\sqrt{s} = 8$ TeV data

The $m_{\gamma\gamma}$ distributions for the 14 categories from 20.7 fb^{-1} $\sqrt{s} = 8$ TeV data are shown in Fig. 8.3, Fig. 8.4, Fig. 8.5, and Fig. 8.6.

Table 8.4 Systematic uncertainty on the number of fitted signal events due to the background model for the $\sqrt{s} = 7$ TeV (10 categories) and $\sqrt{s} = 8$ TeV (14 categories) analyses. Three different background models are used depending on the category: an exponential function; a fourth order polynomial; and the exponential of a second order polynomial.

Category	Parametrisation	Uncertainty $[N_{\mathrm{evt}}]$	
		$\sqrt{s}$ = 7	$\sqrt{s}$ = 8
Inclusive	4th order pol.	7.3	12.0
Unconverted central, low p_{Tt}	Exp. of 2nd order pol.	2.1	4.6
Unconverted central, high p_{Tt}	Exponential	0.2	0.8
Unconverted rest, low p_{Tt}	4th order pol.	2.2	11.4
Unconverted rest, high p_{Tt}	Exponential	0.5	2.0
Converted central, low p_{Tt}	Exp. of 2nd order pol.	1.6	2.4
Converted central, high p_{Tt}	Exponential	0.3	0.8
Converted rest, low p_{Tt}	4th order pol.	4.6	8.0
Converted rest, high p_{Tt}	Exponential	0.5	1.1
Converted transition	Exp. of 2nd order pol.	3.2	9.1
Loose high-mass two-jet	Exponential	0.4	1.1
Tight high-mass two-jet	Exponential	-	0.3
Low-mass two-jet	Exponential	-	0.6
E_T^{miss} significance	Exponential	-	0.1
One-lepton	Exponential	-	0.3

8.5 Excess observed in the full data set

The observed and expected p_0-values calculated from the 4.8 fb^{-1} data at $\sqrt{s} = 7$ TeV and 20.7 fb^{-1} data at $\sqrt{s} = 8$ TeV are shown in Fig. 8.7. The likelihood model used for this p_0-value calculation does not incorporate the diphoton mass scale uncertatineis. The largest excess is observed at $m_H = 126.5$ GeV, and the observed p_0-value of this excess is 8.9×10^{-14}, corresponding

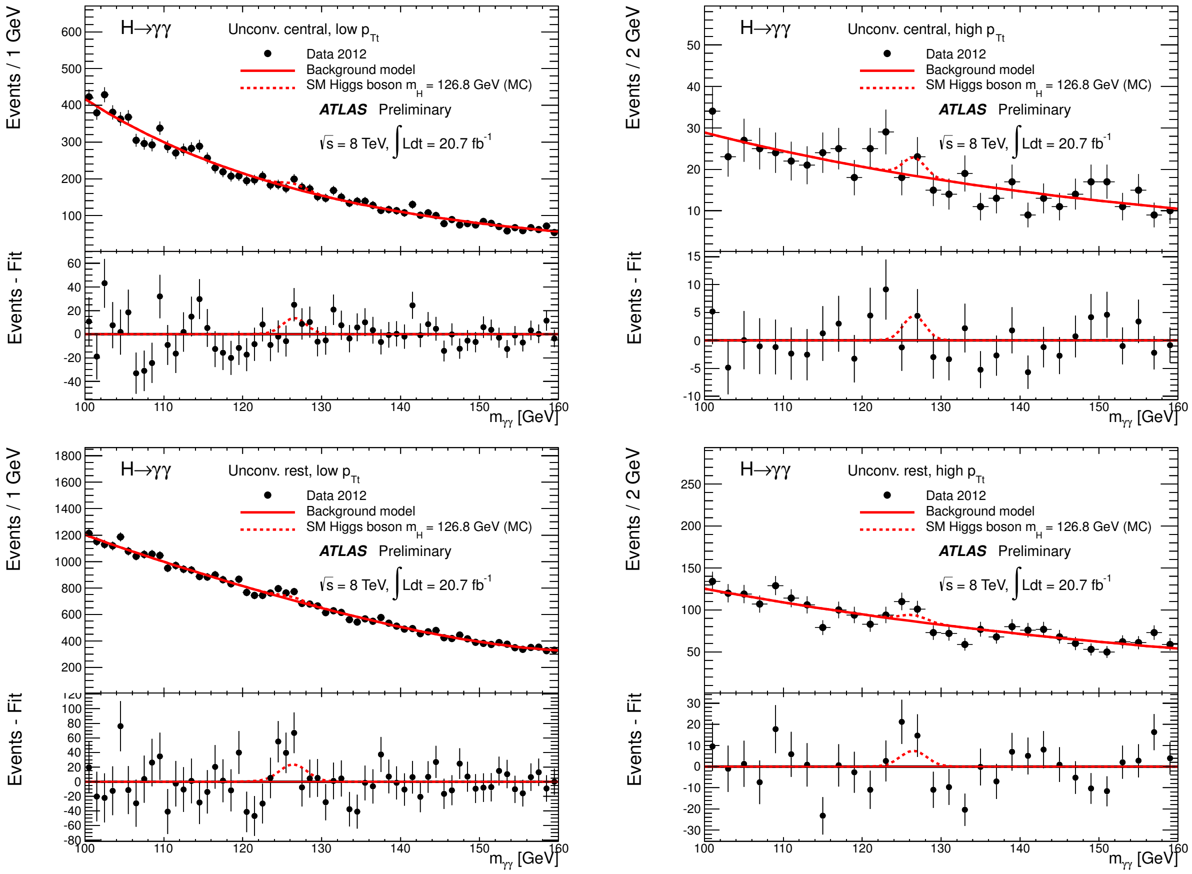

Figure 8.3 Background-only fits to the diphoton invariant mass spectra for categories. The bottom inset displays the residual of the data with respect to the background fit. The Higgs boson expectation for a mass hypothesis of 126.8 GeV corresponding to the SM cross section is also shown.

to a statistical significance of 7.4 σ. With this observation, the diphoton final state by itself can establish the discovery of this new boson.

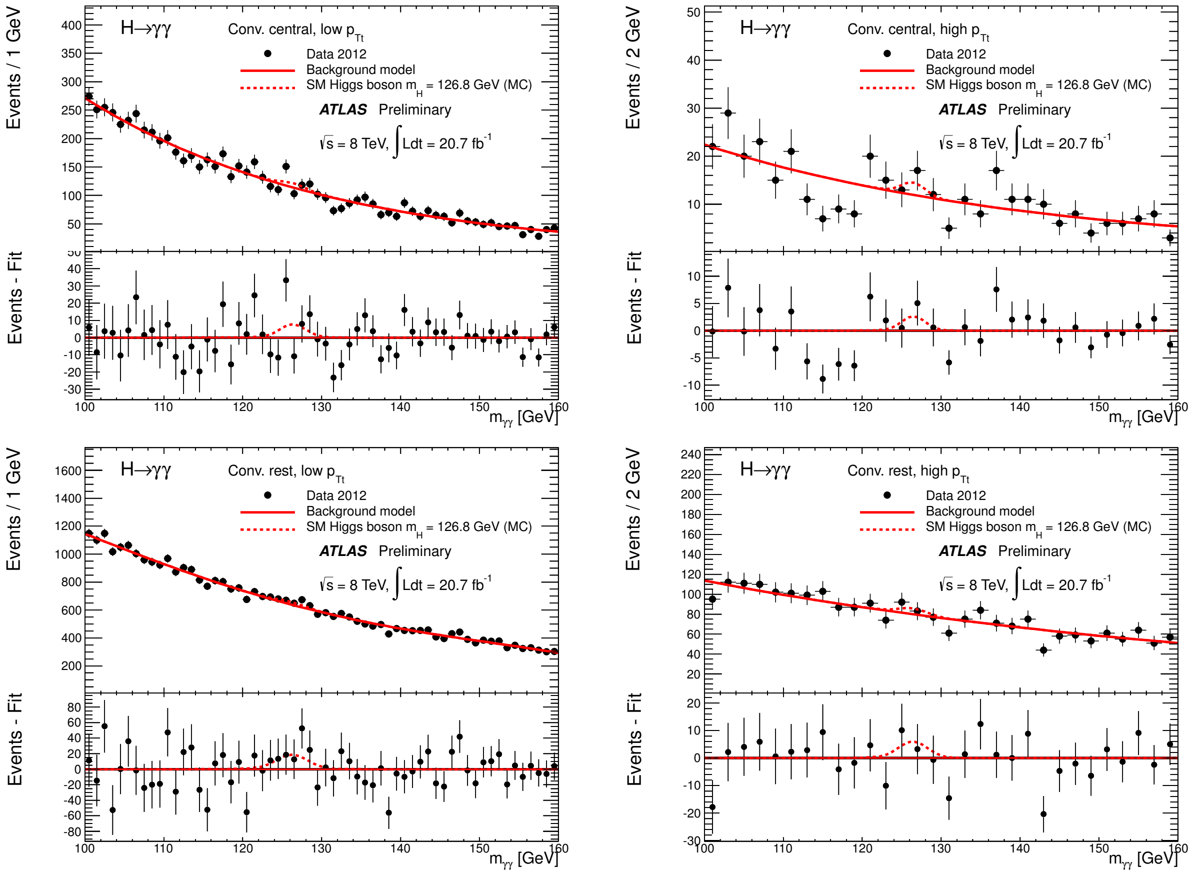

Figure 8.4 Background-only fits to the diphoton invariant mass spectra for categories. The bottom inset displays the residual of the data with respect to the background fit. The Higgs boson expectation for a mass hypothesis of 126.8 GeV corresponding to the SM cross section is also shown.

8.6 Determination of the mass

The mass of the new boson is measured with full 2011 and 2012 datasets, and the measurement result is:

$$m_H = 126.8 \pm 0.2(stat) \pm 0.7(syst)\ GeV \tag{8.1}$$

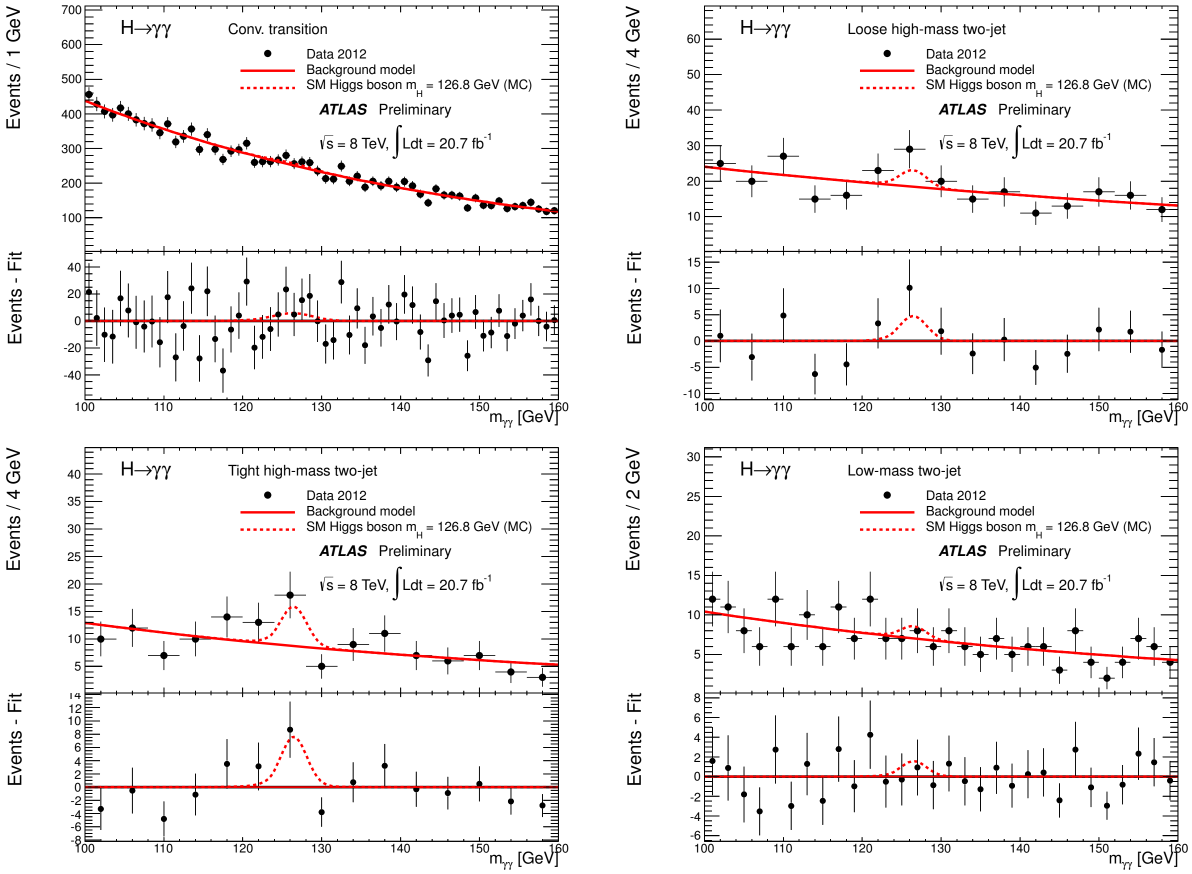

Figure 8.5 Background-only fits to the diphoton invariant mass spectra for categories. The bottom inset displays the residual of the data with respect to the background fit. The Higgs boson expectation for a mass hypothesis of 126.8 GeV corresponding to the SM cross section is also shown.

8.7 Determination of the signal strength

The signal strength measurement is carried out at the measured mass $m_H = 126.8$ GeV. The best fit μ value is found to be:

$$\mu = 1.57^{+0.32}_{-0.28} \tag{8.2}$$

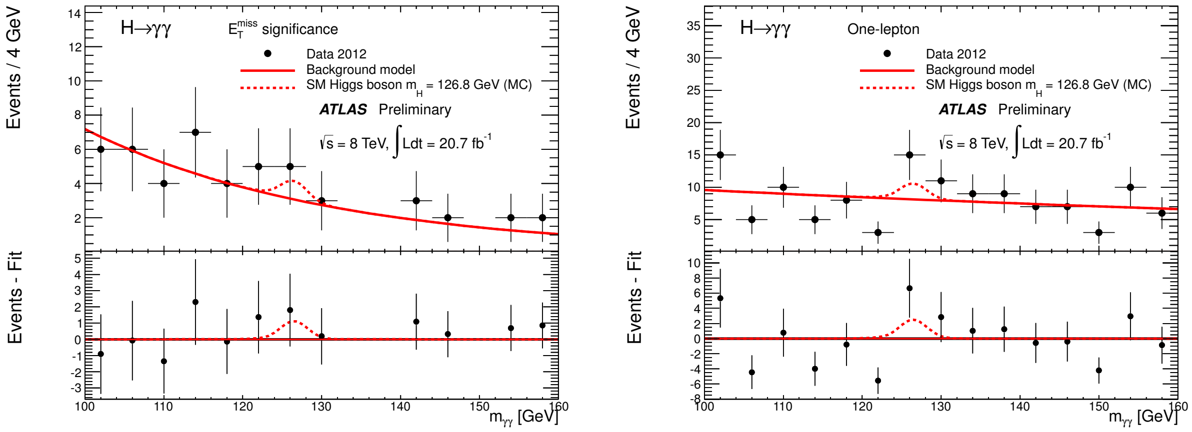

Figure 8.6 Background-only fits to the diphoton invariant mass spectra for categories. The bottom inset displays the residual of the data with respect to the background fit. The Higgs boson expectation for a mass hypothesis of 126.8 GeV corresponding to the SM cross section is also shown.

The uncertainty of this measurement is further broken down to the statistical uncertainty, systematic uncertainty and theoretical uncertainty using the procedure described in Sec. 6.2.5.2, and this is shown in Eq. 8.3.

$$\mu = 1.57 \pm 0.22(stat) \pm 0.17(syst) \pm 0.14(theory) \tag{8.3}$$

The theory uncertainty includes the QCD scale uncertainty of all signal production modes except the ggF+2jets uncertainties, PDF uncertainty and branching ratio uncertainties. These uncertainties affect the prediction of the total signal yields. Other uncertainties that are of theoretical nature but are related to the specific way that the analysis is designed, e.g., the Higgs boson p_T modeling, ggF+2jets uncertainties, etc., are classified as systematic uncertainty.

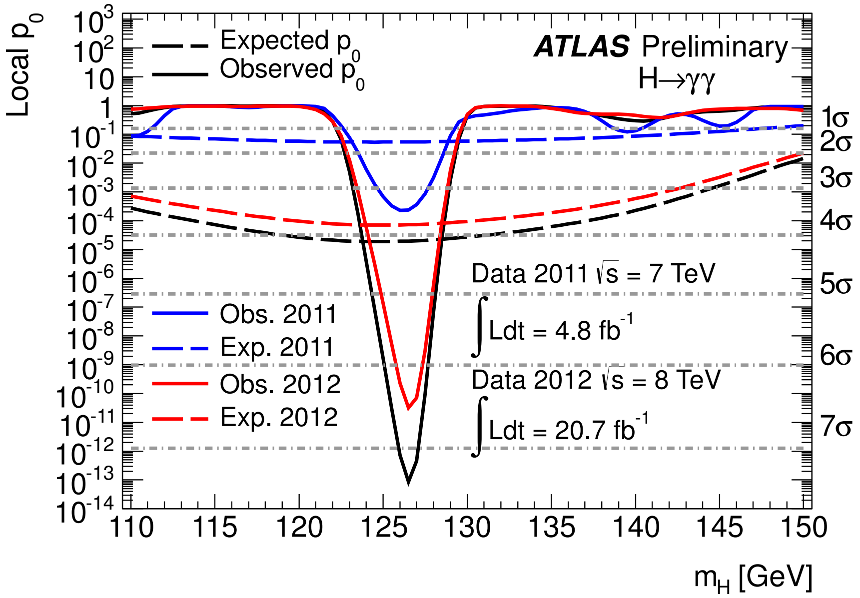

Figure 8.7 The observed p_0 is shown as a function of m_H for the 7 TeV analysis (blue), 8 TeV analysis (red) and the combined analysis (black). The expected p_0 curves are also shown in dashed lines.

The largest contribution to the systematic uncertainty comes from the $m_{\gamma\gamma}$ resolution uncertainty. To illustrate the impact that the $m_{\gamma\gamma}$ resolution uncertainty has on the measurement of μ, a test measurement of μ is performed on two sets of S+B Asimov data[1], one generated with a resolution smaller than the nominal $m_{\gamma\gamma}$ resolution used in the analysis, and the other one generated with a resolution larger than the nominal $m_{\gamma\gamma}$ resolution. In this measurement, the nominal value of $m_{\gamma\gamma}$ resolution is used to construct the PDF. It is found that an underestimated $m_{\gamma\gamma}$ resolution

---

[1] Asimov data is a dataset that perfectly agrees with a given hypothesis and the result obtained from the Asimov data is the expected result corresponding to the given hypothesis. The Asimov data is usually generated as weighted events from the PDF of the given hypothesis.

can lead to a measured μ value that is smaller than its true value, while an overestimated $m_{\gamma\gamma}$ resolution can lead to a measured μ value that is higher than its true value. Among the experimental uncertainties on the signal yield prediction, the luminosity uncertainty and photon identification uncertainty are the dominant uncertainties.

8.7.1 Quantify the deviation from the Standard Model prediction

To quantify the compatibility between the measured μ value and the SM prediction, a new test statistic is constructed:

$$q_1 = -2ln\lambda(\mu) = -2ln\frac{L(\mu)}{L(\hat{\mu})} \tag{8.4}$$

where μ in the numerator is fixed to 1. The test statistic can be used to report the significance on the observed μ value's deviation from the Standard Model prediction. This deviation is found to be at the level of 2.1 σ.

8.8 Towards measuring the coupling

Measuring the individual production mode's contribution in $H \to \gamma\gamma$ channel is an intermediate step towards understanding the coupling between the new particle and other elementary particles. In $H \to \gamma\gamma$ channel, the observables are the strength parameter of the cross section of a production mode i times $H \to \gamma\gamma$ branching ratio, defined as $(\sigma_{i,obs} \times BR_{obs})/(\sigma_{i,SM} \times BR_{SM})$, where $\sigma_{i,obs}(\sigma_{i,SM})$ is the observed (SM expected) cross section for production mode i and $BR_{obs}(BR_{SM})$ is the observed (SM expected) branching ratio for $H \to \gamma\gamma$. Because the production cross section and the branching ratio cannot be measured separately from $H \to \gamma\gamma$ channel alone, the product of them is the only observable.

The measurement analysis has 10 categories from $\sqrt{s} = 7$ TeV data and 14 categories from $\sqrt{s} = 8$ TeV data, and this provides 24 constraints on the signal yields. These constraints can be used to perform various measurements of signal strengths of individual production modes. The idea of such a measurement is illustrated below.

The background-subtracted event yields of the 24 categories at $m_H = 126.8$ GeV can be denoted as a vector $\{O_i\}$ where i is the index of category. Similarly, the expected signal yields of the 24 categories at the same m_H can be denoted as a vector $\{S_i\}$. The effect of a simultaneous fit where μ is the parameter of interest is similar to minimizing the difference between $\{O_i\}$ and $\mu \times \{S_i\}$ although the fit is driven by maximizing the log likelihood value.

The expected signal yields $\{S_i\}$ can be decomposed to a linear combination of the individual production mode's expected signal yields $\{S_{l,i}\}$ (l is the index of the production mode):

$$\begin{pmatrix} S_1 \\ S_2 \\ \vdots \\ S_{24} \end{pmatrix} = \mu_{ggF} \times \begin{pmatrix} S_{ggF,1} \\ S_{ggF,2} \\ \vdots \\ S_{ggF,24} \end{pmatrix} + \mu_{ttH} \times \begin{pmatrix} S_{ttH,1} \\ S_{ttH,2} \\ \vdots \\ S_{ttH,24} \end{pmatrix} + \mu_{VBF} \times \begin{pmatrix} S_{VBF,1} \\ S_{VBF,2} \\ \vdots \\ S_{VBF,24} \end{pmatrix} + \mu_{VH} \times \begin{pmatrix} S_{VH,1} \\ S_{VH,2} \\ \vdots \\ S_{VH,24} \end{pmatrix}$$

In the SM expectation, the strength parameters μ_{ggF}, μ_{VBF}, μ_{VH} and μ_{ttH} have a value of 1. Since the number of constraints from data is 24, these four strength parameters can be determined from data if $\{S_{ggF,i}\}$, $\{S_{VBF,i}\}$, $\{S_{VH,i}\}$ and $\{S_{ttH,i}\}$ are linearly independent. For a hypothetical fit where the parameters of interests are μ_{ggF}, μ_{VBF}, μ_{VH} and μ_{ttH}, the fit effectively minimizes the difference between $\{O_i\}$ and $\mu_{ggF}\times\{S_{ggF,i}\}+\mu_{VBF}\times\{S_{VBF,i}\}+\mu_{VH}\times\{S_{VH,i}\}+\mu_{ttH}\times\{S_{ttH,i}\}$. Tables 5.3 and 8.2 summarize the information of $\{S_{l,i}\}$ and suggest the four $\{S_{l,i}\}$ vectors are linearly independent.

8.8.1 The $\mu_{ggF+ttH}$-μ_{VBF+VH} Model

In this analysis, the expected signal yields of the ttH process is very small and no category is dedicated to selecting ttH signal events. The uncertainty of the μ_{ttH} measurement is therefore expected to be very large. In a simplified model, the strength parameters of ggF and ttH processes are merged as these two processes both concern the coupling between the Higgs boson and top quarks and hence the signal strengths of the two processes are assumed to scaled together. The same argument can be applied to the VBF and VH processes both of which concern the coupling between the Higgs boson and weak bosons. In this simplified model, the expected signal yields $\{S_i\}$ can be decomposed as follows:

$$\begin{pmatrix} S_1 \\ S_2 \\ \vdots \\ S_{24} \end{pmatrix} = \mu_{ggF+ttH} \times \begin{pmatrix} S_{ggF+ttH,1} \\ S_{ggF+ttH,2} \\ \vdots \\ S_{ggF+ttH,24} \end{pmatrix} + \mu_{VBF+VH} \times \begin{pmatrix} S_{VBF+VH,1} \\ S_{VBF+VH,2} \\ \vdots \\ S_{VBF+VH,24} \end{pmatrix}$$

One should have:

$$S_{ggF+ttH,i} = S_{ggF,i} + S_{ttH,i};$$

$$S_{VBF+VH,i} = S_{VBF,i} + S_{VH,i}$$

and the fit effectively minimizes the difference between $\{O_i\}$ and $\mu_{ggF+ttH} \times \{S_{ggF+ttH,i}\} + \mu_{VBF+VH} \times \{S_{VBF+VH,i}\}$. The two parameters of interests can be explicitly written as:

$$\mu_{ggF+ttH} = \frac{(\sigma_{ggF} + \sigma_{ttH})_{obs}}{(\sigma_{ggF} + \sigma_{ttH})_{SM}} \cdot \frac{BR_{obs}}{BR_{SM}} \tag{8.5}$$

and

$$\mu_{VBF+VH} = \frac{(\sigma_{VBF} + \sigma_{VH})_{obs}}{(\sigma_{VBF} + \sigma_{VH})_{SM}} \cdot \frac{BR_{obs}}{BR_{SM}}. \tag{8.6}$$

The profile likelihood ratio constructed on these two parameters of interest is:

$$-2ln\lambda(\mu_{ggF+ttH}, \mu_{VBF+VH}) = -2ln\frac{L(\mu_{ggF+ttH}, \mu_{VBF+VH})}{L(\mu_{gg\hat{F}+ttH}, \mu_{VB\hat{F}+VH})} \tag{8.7}$$

The measurement with this model is shown in Fig. 8.8, and the best fit point of $(\mu_{ggF+ttH}, \mu_{VBF+VH})$ is (1.5,1.8).

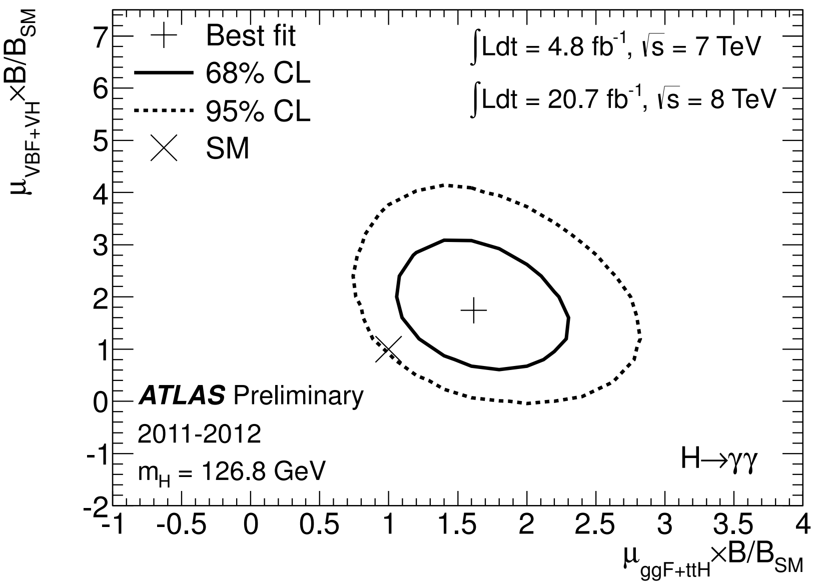

Figure 8.8 The best-fit values (+) of $\mu_{ggF+ttH}$ and μ_{VBF+VH} from a simultaneous fit to the data and their 68% (solid) and 95% (dashed) CL contours. The expectation for a SM Higgs boson is also shown (x).

8.8.2 The $\mu_{ggF+ttH}$-μ_{VBF}-μ_{VH} Model

In an alternative simplified model, the ggF and ttH processes are still assumed to share the same strength parameter, but the strength parameters of VBF and VH processes are independent, i.e., $\mu_{ggF+ttH}$, μ_{VBF} and μ_{VH} are parameters of interest. This model takes advantage of the fact that the $\sqrt{s} = 8$ TeV part of the analysis has VH-enriched categories to enhance the sensitivity to the VH production modes. In this model, the expected signal yields $\{S_i\}$ is decomposed as follows:

$$\begin{pmatrix} S_1 \\ S_2 \\ \vdots \\ S_{24} \end{pmatrix} = \mu_{ggF+ttH} \times \begin{pmatrix} S_{ggF+ttH,1} \\ S_{ggF+ttH,2} \\ \vdots \\ S_{ggF+ttH,24} \end{pmatrix} + \mu_{VBF} \times \begin{pmatrix} S_{VBF,1} \\ S_{VBF,2} \\ \vdots \\ S_{VBF,24} \end{pmatrix} + \mu_{VH} \times \begin{pmatrix} S_{VH,1} \\ S_{VH,2} \\ \vdots \\ S_{VH,24} \end{pmatrix}$$

The profile likelihood ratio is therefore defined as:

$$-2ln\lambda(\mu_i) = -2ln\lambda \frac{L(\mu_i, \hat{\mu_j}, \hat{\mu_k})}{L(\hat{\mu_i}, \hat{\hat{\mu_j}}, \hat{\hat{\mu_k}})} \tag{8.8}$$

The measurement results are:

$$\mu_{ggF+ttH} = 1.54^{+0.42}_{-0.36} = 1.54^{+0.31}_{-0.31}(stat.)^{+0.17}_{-0.16}(syst.)^{+0.18}_{-0.17}(theory) \tag{8.9}$$

$$\mu_{VBF} = 1.63^{+0.95}_{-0.83} = 1.63^{+0.78}_{-0.71}(stat.)^{+0.35}_{-0.33}(syst.)^{+0.25}_{-0.25}(theory) \tag{8.10}$$

$$\mu_{VH} = 1.71^{+1.48}_{-1.28} = 1.71^{+1.40}_{-1.25}(stat.)^{+0.26}_{-0.24}(syst.)^{+0.14}_{-0.12}(theory). \tag{8.11}$$

A spin-off of the $\mu_{ggF+ttH}$-μ_{VBF}-μ_{VH} model is that the p-value of the VBF process can be reported. In Chapter 7 and Sec. 8.5, the p_0-value of the excess is reported with a test statistic where μ is the parameter of interest. The statistically significant excess establishes the discovery of a particle in diphoton final state, but that does not directly suggest the observation of any specific Higgs boson production mode. Given that the ggF signal makes up approximately 90% of the expected signal and the analysis is defined with categories that heavily rely on the correct prediction of individual production mode's event yield distributions between categories, the observation of a statistically significant excess implies the observation of the ggF production mode. This is evident in Fig. 8.8 where the distance between the observed $\mu_{ggF+ttH}$ value and the line of $\mu_{ggF+ttH} = 0$ is far larger than two standard deviations. It is noteworthy that Fig. 8.8 presents a two-dimensional measurement where the contour is defined with a more stringent requirement on the likelihood ratio compared to a one-dimensional hypothesis test.

The observation of the VBF production is less obvious. To quantify the statistical significance of the VBF production from data, the p-value should be evaluated for the null-VBF hypothesis where μ_{VBF} is the parameter of interest and $\mu_{ggF+ttH}$ and μ_{VH} are treated as nuisance parameters. In this statistical test, the role of ggF, ttH and VH processes is the same as background. The test statistic is defined as:

$$-2ln\lambda(\mu_{VBF}) = -2ln\lambda\frac{L(\mu_{VBF}, \mu_{gg\hat{F}+ttH}, \mu_{\hat{V}H})}{L(\mu_{\hat{V}BF}, \mu_{gg\hat{\hat{F}}+ttH}, \mu_{\hat{\hat{V}}H})} \tag{8.12}$$

Fig. 8.9 shows the $p_{0,VBF}$ as a function of m_H. At $m_H =$ 126.8 GeV, the mass measured from the combination of all categories, the statistical significance of VBF process is slightly lower than 2 σ. The largest excess in μ_{VBF} is found at $m_H =$ 123.5 GeV, about 2 GeV away from 126.8 GeV, and its statistical significance is about 2.9 σ. Given that the best fit m_H from the mass measurement in $H \to \gamma\gamma$ channel is 126.8 GeV, it is less biased to consider the result at $m_H = 126.8$ GeV as the observed significance of the VBF production in the $H \to \gamma\gamma$ channel. With the current data in the $H \to \gamma\gamma$ channel, the observation of VBF production cannot be established.

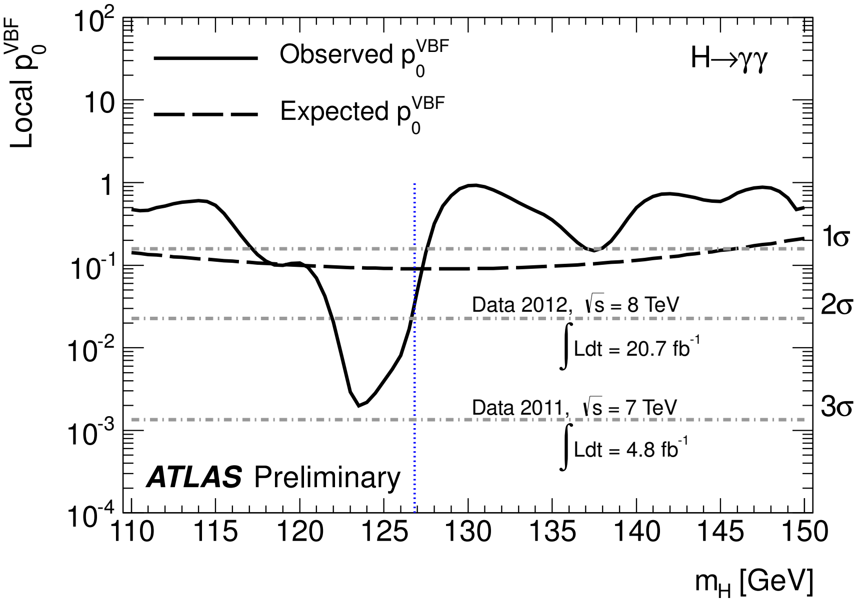

Figure 8.9 The observed local $p_{0,VBF}$ value for VBF production as a function of m_H for the combination of $\sqrt{s} = 7$ TeV and $\sqrt{s} = 8$ TeV data (solid line) and the corresponding expected local $p_{0,VBF}$ values for the SM Higgs boson signal plus background hypothesis (dashed line).

8.9 The $H \to \gamma\gamma$ relevant measurements in the combination of diboson final states

The $H \to \gamma\gamma$ result with the 4.8 fb^{-1} $\sqrt{s} = 7$ TeV data and 20.7 fb^{-1} $\sqrt{s} = 8$ TeV data is combined with the result from $H \to ZZ^{(\star)} \to 4l$ channel and the result from $H \to WW^{(\star)} \to l\nu l\nu$ channel to measure the properties of the neural boson [106, 107].

The mass of the neutral boson is measured from the $H \to \gamma\gamma$ channel and the $H \to ZZ^{(\star)} \to 4l$ channel, the two channels with good resolution. The measured mass from $H \to \gamma\gamma$ channel is

$m_H = 126.8 \pm 0.2$ (stat) ± 0.7 (sys) GeV, and the measured mass from $H \rightarrow ZZ^{(\star)} \rightarrow 4l$ channel is $m_H = 124.3^{+0.6}_{-0.5}$ (stat) $^{+0.5}_{-0.3}$ (sys) GeV. The mass measurement combing these two channels leads to $m_H = 125.5$ ± 0.2 (stat) $^{+0.5}_{-0.6}$ (sys) GeV. Fig. 8.10 [106] shows the profile likelihood ratio scan on m_H for the $H \rightarrow \gamma\gamma$ channel, $H \rightarrow ZZ^{(\star)} \rightarrow 4l$ channel and their combination. The m_H where each curve reaches its minimum corresponds to the measured central value of the m_H in that particular measurement. It is noticeable that the $H \rightarrow \gamma\gamma$ and $H \rightarrow ZZ^{(\star)} \rightarrow 4l$ channels lead to different measured m_H, and this difference is measured to be $\Delta m = 2.3$ $^{+0.6}_{-0.7}$ (stat) ± 0.6 GeV. To quantify the consistency in the measured m_H between the two channels, a hypothesis of $\Delta m = 0$ is tested against the observation with pseudo-experiments, and the p-value of the $\Delta m = 0$ hypothesis is found to 1.5%. This p-value increases to $\sim 8\%$ when the possible non-Gaussian effect of the uncertainty is considered. It is therefore concluded that no statistically significant mass difference between the diphoton channel and four-lepton channel is observed in data.

The Higgs boson signal strength is then measured at $m_H = 125.5$ GeV, the m_H measured from the combination of the $H \rightarrow \gamma\gamma$ and $H \rightarrow ZZ^{(\star)} \rightarrow 4l$ channels, by combining the inputs from the $H \rightarrow \gamma\gamma$, $H \rightarrow ZZ^{(\star)} \rightarrow 4l$ and $H \rightarrow WW^{(\star)} \rightarrow l\nu l\nu$ channels. Fig. 8.11 [106] shows the profile likelihood ratio scan over μ. The measured Higgs boson signal strength is 1.33 ± 0.14 (stat) ± 0.15 (sys).

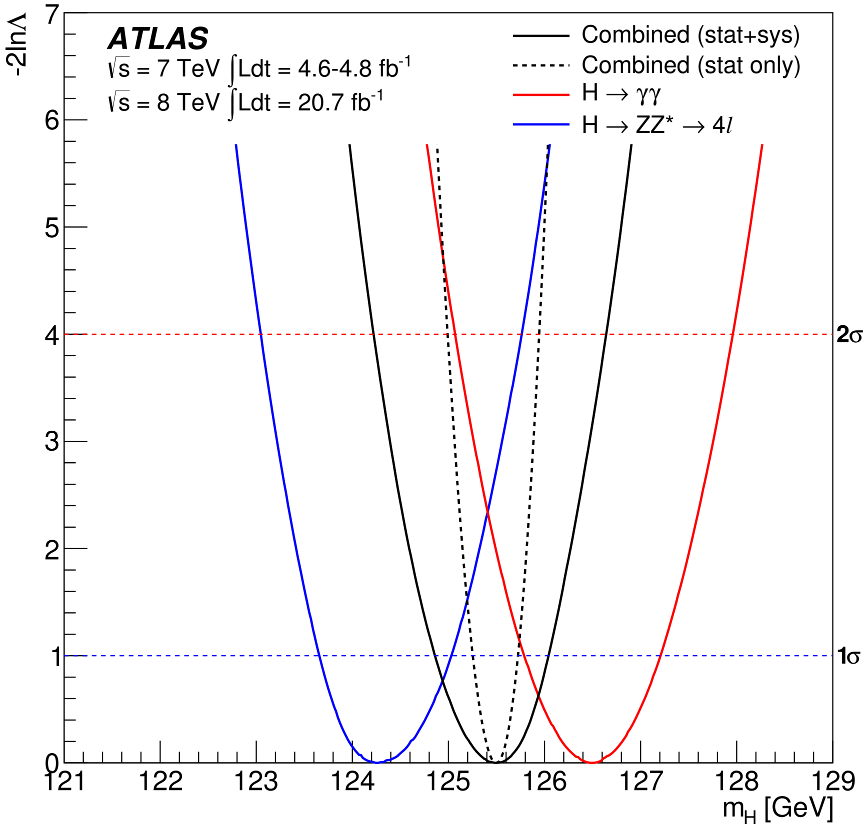

Figure 8.10 The profile likelihood ratio as a function of m_H for the $H \to \gamma\gamma$ and $H \to ZZ^{(\star)} \to 4l$ channels and their combination, obtained by allowing the signal strengths of $H \to \gamma\gamma$ and $H \to ZZ^{(\star)} \to 4l$ to vary independently. The dashed line shows the statistical component of the uncertainty on the combined mass measurement. Mass scale systematic uncertainties are treated as correlated between $H \to \gamma\gamma$ and $H \to ZZ^{(\star)} \to 4l$ also for the individual $H \to \gamma\gamma$ and $H \to ZZ^{(\star)} \to 4l$ distributions.

The signal strength of $H \to \gamma\gamma$ is also measured at $m_H = 125.5$ GeV and found to be:

$$\mu = 1.55^{+0.33}_{-0.28} = 1.55^{+0.23}_{-0.22}(stat)^{+0.24}_{-0.18}(sys). \tag{8.13}$$

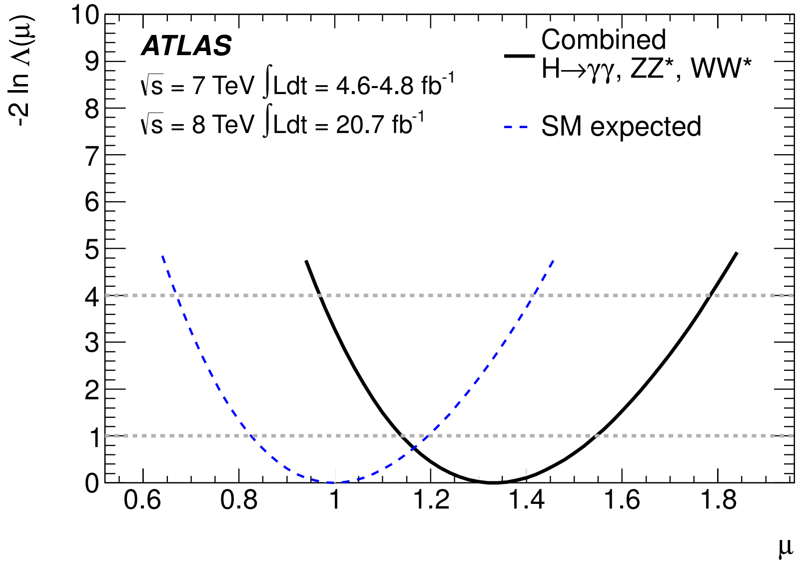

Figure 8.11 The profile likelihood ratio as a function of μ for the combination of the $H \to \gamma\gamma$, $H \to ZZ^{(\star)} \to 4l$ and $H \to WW^{(\star)} \to l\nu l\nu$ channels. The dashed curve shows the SM expectation.

The signal strength measured at $m_H = 125.5$ GeV is not so different from the signal strength measured at $m_H = 126.8$ GeV, primarily because the diphoton mass scale uncertainties are incorporated in the likelihood model. The mass of the new boson measured from the $H \to \gamma\gamma$ channel is about 126.8 GeV, and the signal PDF at $m_H = 125.5$ GeV is not aligned with the peak physically at around 126.8 GeV in data. However, since the fit is driven by maximizing the log likelihood value, it is possible to increase the log likelihood value by pulling diphoton mass scale nuisance parameters so that the signal PDF at $m_H = 125.5$ GeV with a shifted mean value is better aligned with the peak at $m_H = 126.8$ GeV. The pulling of nuisance parameters introduces negative contributions to the log likelihood value, but at the same time, as the signal PDF gets better aligned with the peak in data, the statistical component of the log likelihood would increase. As a "rule of thumb", the pulling of the nuisance parameter can be pproximately as large as the statistical significance of the excess in data, because the final log likelihood value is a sum of the log likelihood value of the statistical component and the log likelihood value of systematic component. The 7.4 σ excess leaves a room for the diphoton mass scale nuisance parameters to be pulled as large as ≈ 7.4 standard deviations. The total systematic uncertainty of the $H \to \gamma\gamma$ mass measurement is 0.7 GeV, and the difference between the measured from the $H \to \gamma\gamma$ channel alone and the mass from the combination of $H \to \gamma\gamma$ and $H \to ZZ^{(\star)} \to 4l$ channels is 1.3 GeV. This means that only approximately 2 standard deviations pulling of the diphoton mass scale nuisance parameters can make the signal PDF at $m_H = 125.5$ GeV perfectly aligned with the diphoton peak at $m_H = 126.8$ GeV and this 2 σ level of pulling is much less than the statistical significance of the excess. Since the signal PDF at $m_H = 125.5$ GeV can be easily shifted to $m_H = 126.8$ GeV by pulling the nuisance parameters, the fitted number of signal events from the shifted signal PDF at $m_H = 125.5$ GeV should be the same the fitted number of signal events from the measurement with a signal PDF at $m_H = 126.8$ GeV. The difference in the measured μ between Eq. 8.13 and Eq. 8.3 is simply due to the difference in the expected signal yield at these two m_H points.

Fig. 8.12 shows the signal strengths measured in the $H \to \gamma\gamma$, $H \to ZZ^{(\star)} \to 4l$, and $H \to WW^{(\star)} \to l\nu l\nu$ channels and their combination at $m_H = 125.5$ GeV.

The gluon fusion production and $H \rightarrow \gamma\gamma$ decay are both loop-induced processes which are sensitive to potential BSM physics processes. The strength of the ggF production and the strength of $H \rightarrow \gamma\gamma$ branching ratio can be separated in the combined measurement where the $H \rightarrow ZZ^{(\star)} \rightarrow 4l$ and $H \rightarrow WW^{(\star)} \rightarrow l\nu l\nu$ channels can constrain the ggF production and thus break the degeneracy between the ggF production strength and $H \rightarrow \gamma\gamma$ decay strength in the $H \rightarrow \gamma\gamma$ channel. In the combination, κ_g^2 and κ_γ^2 are introduced to be the strength parameter of the gluon fusion production and the strength parameter of $H \rightarrow \gamma\gamma$ decay, respectively [108, 106]. A 2-D measurement that simultaneously determines the central values of κ_g and κ_γ and reveals the correlation between the measurement of κ_g and the measurement of κ_γ is shown in Fig. 8.13 [106].

The best-fit values of κ_g and κ_γ are:

$$\kappa_g = 1.04 \pm 0.14 \tag{8.14}$$

$$\kappa_\gamma = 1.20 \pm 0.15 \tag{8.15}$$

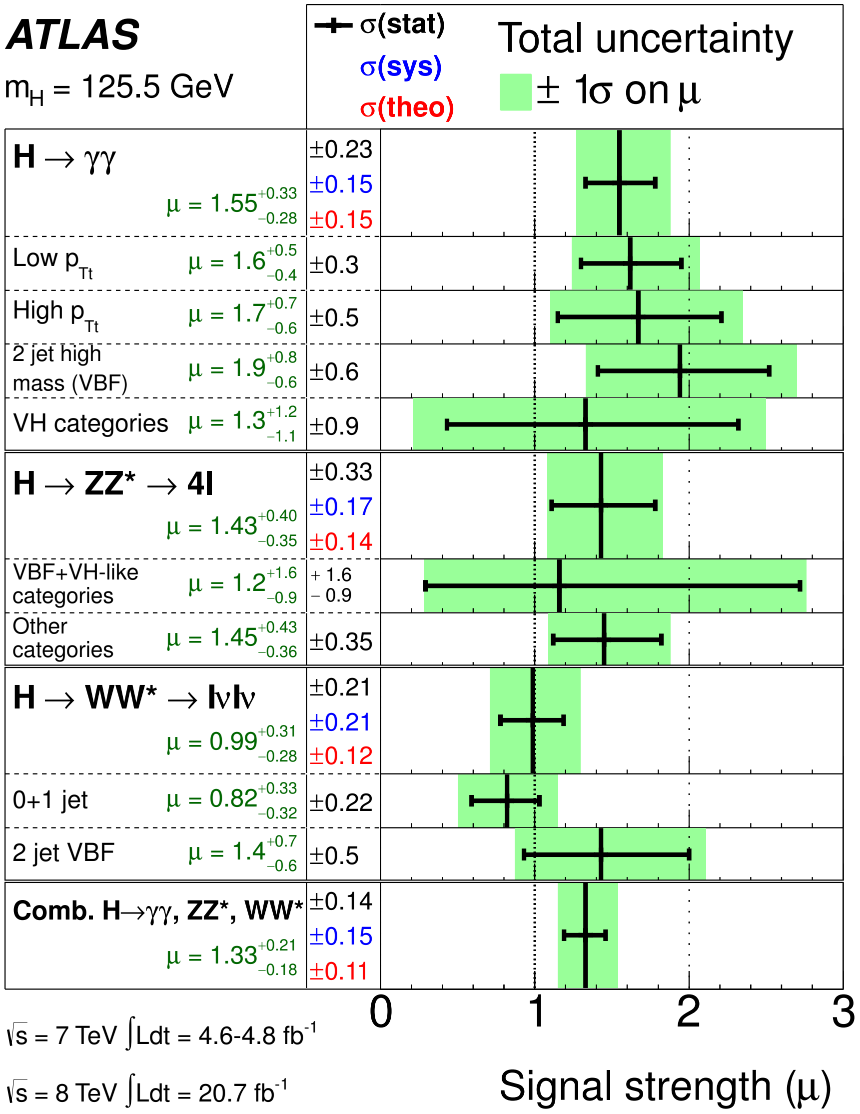

Figure 8.12 The measured production strengths for a Higgs boson of mass m_H =125.5 GeV, normalized to the SM expectations, for diboson final states and their combination. Results are also given for the main categories of each analysis. The best-fit values are shown by the solid vertical lines, with the total $\pm1\sigma$ uncertainty indicated by the shaded band, and the statistical uncertainty by the superimposed horizontal error bars. The numbers in the second column specify the contributions of the (symmetrized) statistical uncertainty (top), the total (experimental and theoretical) systematic uncertainty (middle), and the theory uncertainty (bottom) on the signal cross section (from QCD scale, PDF, and branching ratios) alone; for the individual categories only the statistical uncertainty is given.

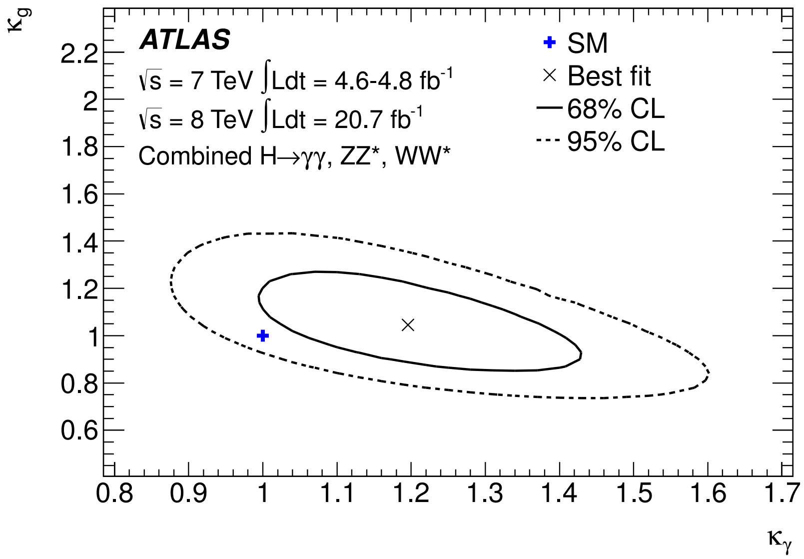

Figure 8.13 Likelihood contours for the coupling scale factors κ_γ and κ_g probing BSM contributions to the $H \to \gamma\gamma$ and $gg \to H$ loops, assuming no BSM contributions to the total Higgs boson width. The best-fit result ($\times$) and the SM expectation (+) are also indicated.

Chapter 9

Conclusion and outlook

With 4.8 fb^{-1} data at $\sqrt{s} = 7$ TeV taken in 2011 and 5.9 fb^{-1} data at $\sqrt{s} = 8$ TeV taken from March to June in 2012, an excess of events at $m_H = $ 126.5 GeV with a statistical significance of 4.5 σ is observed in the search for a SM Higgs boson in the diphoton final state. The diphoton excess, along with the excesses of events observed in the search for SM $H \to ZZ^{(\star)} \to 4l$ and the search for SM $H \to WW^{(\star)} \to l\nu l\nu$, lead to an excess at $m_H = $ 126 GeV with a statistical significance of 5.9 σ in the combination of the SM Higgs boson searches. This establishes the discovery of a new boson. With the 20.7 fb^{-1} data at $\sqrt{s} = 8$ TeV collected in the entire year of 2012 and the 4.8 fb^{-1} data at $\sqrt{s} = 7$ TeV taken in 2011, the statistical significance of the diphoton excess reaches 7.4 σ and hence the diphoton channel by itself can establish the discovery of the new boson.

The mass of the new boson measured from the diphoton final state alone is 126.8 ± 0.4(stat.) ± 0.8(syst.) GeV. The signal strength measured at this mass is 1.57 $^{+0.32}_{-0.28}$ which shows a 2.1 σ level deviation from the SM prediction. The mass of the new boson measured from a combination of the $H \rightarrow \gamma\gamma$ channel and $H \rightarrow ZZ^{(\star)} \rightarrow 4l$ channel is 125.5 ±0.2 (stat) $^{+0.5}_{-0.6}$ (sys) GeV, and the $H \rightarrow \gamma\gamma$ signal strength measured at this mass is $1.55^{+0.33}_{-0.28}$.

The observation of the $H \rightarrow \gamma\gamma$ process offers rich and interesting physics that can be explored with much more data to be collected in the next LHC run at $\sqrt{s}$ = 13 or 14 TeV. First of all, the $H \rightarrow \gamma\gamma$ signal strength measured from the ATLAS experiment shows a 2.1 σ upward deviation from the SM prediction. However, the CMS experiment observes a $H \rightarrow \gamma\gamma$ signal strength that agrees with the SM prediction [109]. This difference between two experiments will have to be resolved in the coming years. Since the $H \rightarrow \gamma\gamma$ decay is induced by charged particle loops, a precision measurement of the $H \rightarrow \gamma\gamma$ signal strength will provide sensitivity to potential BSM physics that may change the decay rate of $H \rightarrow \gamma\gamma$. Additionally, it is also interesting to measure the ratio of the $H \rightarrow \gamma\gamma$ branching ratio over the $H \rightarrow Z\gamma$ branching ratio. Both of these decays are induced by charged particle loops, however, the potential variation in the $H \rightarrow Z\gamma$ branching ratio due to the presence of a charged BSM particle is also dependent on the weak charge of the new particle and therefore the variation in the loop-induced branching ratios can be different between the two decays. Measuring the ratio of $\frac{BR(H\rightarrow\gamma\gamma)}{BR(H\rightarrow Z\gamma)}$ can reveal characteristics of the BSM particle that contributes to the loops, should such a BSM particle exist.

Furthermore, the signature of diphoton resonance provides an easy and clear tag for Higgs boson decay in measurements or searches for more complicated processes where a Higgs boson is in the final state. For a hadron collider, the conventional wisdom usually suggests that signatures like $b\bar{b}$ or $\tau^+\tau^-$ should be considered as a tag for the Higgs boson decay in searches for those complicated processes due to their large branching ratios. However, triggering, reconstructing, and identifying these signatures are difficult and often achieved at a cost of losing signal efficiencies. The competitiveness of the diphoton channel becomes clear after the event selection is applied. More specifically, measurements of the VBF, VH and ttH productions can be performed in the $H \rightarrow \gamma\gamma$ channel where both the signal and background are easier to reconstruct and control than channels such as WW, $b\bar{b}$, and $\tau\tau$. This is also the case for some potential BSM processes where a Higgs boson is the decay product or produced in association with other new particles. In the longer term, the Higgs boson self-coupling measurement can also be done by reconstructing the diphoton resonance at around 126 GeV and tagging two b-jets.

The success of the future measurements and searches involved with the $H \rightarrow \gamma\gamma$ signature will critically depend on improvements in the photon performance in the ATLAS detector and a better understanding of the background distribution. Specially, the photon energy resolution uncertainty, which is the largest contribution to the uncertainty of the $H \rightarrow \gamma\gamma$ signal strength measurement, needs to be reduced so that a more precise determination of the strength parameter of the $H \rightarrow \gamma\gamma$ decay loop κ_γ is possible. Moreover, the current understanding of the potential bias in modeling background $m_{\gamma\gamma}$ distribution is at the level at around 20% of the *current* background statistical uncertainty. As the modeling uncertainty is not scaled with luminosity, this uncertainty will affect the measurement more severely as the size of the diphoton sample gets larger. When the statistical uncertainty gradually reduces in future, these aforementioned systematical uncertainties will pose the ultimate bound on the precision that $H \rightarrow \gamma\gamma$ channel can achieve.

LIST OF REFERENCES

[1] C. N. Yang and R. L. Mills, "Conservation of isotopic spin and isotopic gauge invariance," *Phys. Rev.*, vol. 96, pp. 191–195, Oct 1954.

[2] A. Salam and J. C. Ward, "On A Gauge Theory OF Elementary Interactions," *Nuovo Cim.*, vol. 19, pp. 165–170, 1961.

[3] S. Glashow, "Partial Symmetries of Weak Interactions," *Nucl.Phys.*, vol. 22, pp. 579–588, 1961.

[4] A. Salam and J. C. Ward, "Electromagnetic and weak interactions," *Phys.Lett.*, vol. 13, pp. 168–171, 1964.

[5] S. Weinberg, "A model of leptons," *Phys. Rev. Lett.*, vol. 19, pp. 1264–1266, Nov 1967.

[6] A. Salam, "Elementary particle theory: Relativistic groups and analyticity (nobel symposium no. 8)," p. 367, 1968.

[7] J. Schwinger, "A theory of the fundamental interactions," 1957.

[8] T. D. Lee and C. N. Yang, "Possible nonlocal effects in μ decay," *Phys. Rev.*, vol. 108, pp. 1611–1614, Dec 1957.

[9] J. Goldstone, "Field Theories with Superconductor Solutions," *Nuovo Cim.*, vol. 19, pp. 154–164, 1961.

[10] F. Englert and R. Brout, "Broken symmetry and the mass of gauge vector mesons," *Phys. Rev. Lett.*, vol. 13, p. 321, 1964.

[11] P. W. Higgs, "Broken symmetries, massless particles and gauge fields," *Phys. Lett.*, vol. 12, p. 132, 1964.

[12] G. Guralnik, C. Hagen, and T. Kibble, "Global Conservation Laws and Massless Particles," *Phys.Rev.Lett.*, vol. 13, pp. 585–587, 1964.

[13] F. Hasert *et al.*, "Observation of Neutrino Like Interactions Without Muon Or Electron in the Gargamelle Neutrino Experiment," *Phys.Lett.*, vol. B46, pp. 138–140, 1973.

[14] G. Arnison *et al.*, "Experimental Observation of Isolated Large Transverse Energy Electrons with Associated Missing Energy at $\sqrt{s}$ = 540-GeV," *Phys.Lett.*, vol. B122, pp. 103–116, 1983.

[15] M. Banner *et al.*, "Observation of Single Isolated Electrons of High Transverse Momentum in Events with Missing Transverse Energy at the CERN $p\bar{p}$ Collider," *Phys.Lett.*, vol. B122, pp. 476–485, 1983.

[16] G. Arnison *et al.*, "Experimental Observation of Lepton Pairs of Invariant Mass Around 95-GeV/c^2 at the CERN SPS Collider," *Phys.Lett.*, vol. B126, pp. 398–410, 1983.

[17] P. Bagnaia *et al.*, "Evidence for $Z^0 \to e^+e^-$ at the CERN $p\bar{p}$ Collider," *Phys.Lett.*, vol. B129, pp. 130–140, 1983.

[18] R. Barate *et al.*, "Search for the standard model Higgs boson at LEP," *Phys.Lett.*, vol. B565, pp. 61–75, 2003.

[19] T. Aaltonen *et al.*, "Combination of Tevatron searches for the standard model Higgs boson in the W+W- decay mode," *Phys.Rev.Lett.*, vol. 104, p. 061802, 2010.

[20] L. Evans and P. Bryant, "LHC Machine," *JINST*, vol. 3, p. S08001, 2008.

[21] G. Aad *et al.*, "The ATLAS Experiment at the CERN Large Hadron Collider," *JINST*, vol. 3, p. S08003, 2008.

[22] S. Chatrchyan *et al.*, "The CMS experiment at the CERN LHC," *JINST*, vol. 3, p. S08004, 2008.

[23] K. Aamodt *et al.*, "The ALICE experiment at the CERN LHC," *JINST*, vol. 3, p. S08002, 2008.

[24] J. Alves, A. Augusto *et al.*, "The LHCb Detector at the LHC," *JINST*, vol. 3, p. S08005, 2008.

[25] G. Aad *et al.*, “Observation of a new particle in the search for the Standard Model Higgs boson with the ATLAS detector at the LHC,” *Phys.Lett.*, vol. B716, pp. 1–29, 2012.

[26] S. Chatrchyan *et al.*, “Observation of a new boson at a mass of 125 GeV with the CMS experiment at the LHC,” *Phys.Lett.*, vol. B716, pp. 30–61, 2012.

[27] S. Dittmaier *et al.*, “Handbook of LHC Higgs Cross Sections: 1. Inclusive Observables,” 2011.

[28] S. Dawson and R. Kauffman, “QCD corrections to Higgs boson production: nonleading terms in the heavy quark limit,” *Phys.Rev.*, vol. D49, pp. 2298–2309, 1994.

[29] A. Djouadi, M. Spira, and P. Zerwas, “Production of Higgs bosons in proton colliders: QCD corrections,” *Phys.Lett.*, vol. B264, pp. 440–446, 1991.

[30] D. Graudenz, M. Spira, and P. M. Zerwas, “Qcd corrections to higgs-boson production at proton-proton colliders,” *Phys. Rev. Lett.*, vol. 70, pp. 1372–1375, Mar 1993.

[31] M. Spira, A. Djouadi, D. Graudenz, and P. Zerwas, “Higgs boson production at the LHC,” *Nucl.Phys.*, vol. B453, pp. 17–82, 1995.

[32] R. V. Harlander, “Virtual corrections to g g —gt; H to two loops in the heavy top limit,” *Phys.Lett.*, vol. B492, pp. 74–80, 2000.

[33] S. Catani, D. de Florian, and M. Grazzini, “Higgs production in hadron collisions: Soft and virtual QCD corrections at NNLO,” *JHEP*, vol. 0105, p. 025, 2001.

[34] R. V. Harlander and W. B. Kilgore, “Soft and virtual corrections to $p\ \vec{p}\ h+x$ at next-to-next-to-leading order,” *Phys. Rev. D*, vol. 64, p. 013015, Jun 2001.

[35] R. V. Harlander and W. B. Kilgore, “Next-to-next-to-leading order higgs production at hadron colliders,” *Phys. Rev. Lett.*, vol. 88, p. 201801, May 2002.

[36] C. Anastasiou and K. Melnikov, “Higgs boson production at hadron colliders in NNLO QCD,” *Nucl.Phys.*, vol. B646, pp. 220–256, 2002.

[37] V. Ravindran, J. Smith, and W. L. van Neerven, “NNLO corrections to the total cross-section for Higgs boson production in hadron hadron collisions,” *Nucl.Phys.*, vol. B665, pp. 325–366, 2003.

[38] J. Blumlein and V. Ravindran, “Mellin moments of the next-to-next-to leading order coefficient functions for the Drell-Yan process and hadronic Higgs-boson production,” *Nucl.Phys.*, vol. B716, pp. 128–172, 2005.

[39] M. Ciccolini, A. Denner, and S. Dittmaier, “Strong and electroweak corrections to the production of Higgs + 2-jets via weak interactions at the LHC,” *Phys. Rev. Lett.*, vol. 99, p. 161803, 2007.

[40] M. Ciccolini, A. Denner, and S. Dittmaier, “Electroweak and QCD corrections to Higgs production via vector-boson fusion at the LHC,” *Phys. Rev.*, vol. D77, p. 013002, 2008.

[41] K. Arnold *et al.*, “VBFNLO: A Parton level Monte Carlo for processes with electroweak bosons,” *Comput. Phys. Commun.*, vol. 180, p. 1661, 2009.

[42] P. Bolzoni, F. Maltoni, S.-O. Moch, and M. Zaro, “Higgs production via vector-boson fusion at NNLO in QCD,” *Phys. Rev. Lett.*, vol. 105, p. 011801, 2010.

[43] T. Han and S. Willenbrock, “QCD correction to the $pp \to WH$ and ZH total cross-sections,” *Phys. Lett.*, vol. B273, p. 167, 1991.

[44] O. Brein, A. Djouadi, and R. Harlander, “NNLO QCD corrections to the Higgs-strahlung processes at hadron colliders,” *Phys. Lett.*, vol. B579, p. 149, 2004.

[45] M. Ciccolini, S. Dittmaier, and M. Krämer, “Electroweak radiative corrections to associated WH and ZH production at hadron colliders,” *Phys. Rev.*, vol. D68, p. 073003, 2003.

[46] W. Beenakker *et al.*, “Higgs radiation off top quarks at the Tevatron and the LHC,” *Phys. Rev. Lett.*, vol. 87, p. 201805, 2001.

[47] W. Beenakker *et al.*, “NLO QCD corrections to $t\bar{t}H$ production in hadron collisions,” *Nucl. Phys.*, vol. B653, p. 151, 2003.

[48] S. Dawson, L. Orr, L. Reina, and D. Wackeroth, “Next-to-leading order QCD corrections to $pp \to t\bar{t}h$ at the CERN Large Hadron Collider,” *Phys. Rev.*, vol. D67, p. 071503, 2003.

[49] S. Dawson, C. Jackson, L. Orr, L. Reina, and D. Wackeroth, “Associated Higgs production with top quarks at the large hadron collider: NLO QCD corrections,” *Phys. Rev.*, vol. D68, p. 034022, 2003.

[50] J. R. Ellis, M. K. Gaillard, and D. V. Nanopoulos, “A Phenomenological Profile of the Higgs Boson,” *Nucl.Phys.*, vol. B106, p. 292, 1976.

[51] B. W. Lee, C. Quigg, and H. Thacker, “The Strength of Weak Interactions at Very High-Energies and the Higgs Boson Mass,” *Phys.Rev.Lett.*, vol. 38, pp. 883–885, 1977.

[52] B. W. Lee, C. Quigg, and H. B. Thacker, “Weak interactions at very high energies: The role of the higgs-boson mass,” *Phys. Rev. D*, vol. 16, pp. 1519–1531, Sep 1977.

[53] J. F. Gunion, S. Dawson, H. E. Haber, and G. L. Kane, *The Higgs hunter’s guide*. Frontiers in Physics, Boulder, CO: Westview, 1990. Later reprinted under the ’Frontiers in Physics’ series from Perseus Publishing in 2000 (this edition also available in the library).

[54] M. Spira, “QCD effects in Higgs physics,” *Fortsch.Phys.*, vol. 46, pp. 203–284, 1998.

[55] T. Binoth, J. Guillet, E. Pilon, and M. Werlen, “A Full next-to-leading order study of direct photon pair production in hadronic collisions,” *Eur.Phys.J.*, vol. C16, pp. 311–330, 2000.

[56] T. Binoth, J. Guillet, E. Pilon, and M. Werlen, “A next-to-leading order study of pion pair production and comparison with E706 data,” 2001.

[57] T. Binoth, J. Guillet, E. Pilon, and M. Werlen, “A Next-to-leading order study of photon pion and pion pair hadro production in the light of the Higgs boson search at the LHC,” *Eur.Phys.J.direct*, vol. C4, p. 7, 2002.

[58] T. Sjostrand, S. Mrenna, and P. Z. Skands, “PYTHIA 6.4 Physics and Manual,” *JHEP*, vol. 0605, p. 026, 2006.

[59] G. Aad *et al.*, “Expected Performance of the ATLAS Experiment - Detector, Trigger and Physics,” 2009.

[60] “Electron performance measurements with the ATLAS detector using the 2010 LHC proton-proton collision data,” *Eur. Phys. J.*, vol. C72, p. 1909, 2012.

[61] “Energy linearity and resolution of the {ATLAS} electromagnetic barrel calorimeter in an electron test-beam,” *Nuclear Instruments and Methods in Physics Research Section A: Accelerators, Spectrometers, Detectors and Associated Equipment*, vol. 568, no. 2, pp. 601 – 623, 2006.

[62] W. Lampl *et al.*, “Calorimeter clustering algorithms: description and performance,” Tech. Rep. ATL-LARG-PUB-2008-002, 2008.

[63] M. Cacciari, G. P. Salam, and G. Soyez, “The Anti-k(t) jet clustering algorithm,” *JHEP*, vol. 0804, p. 063, 2008.

[64] C. Cojocaru *et al.*, “Hadronic calibration of the ATLAS liquid argon end-cap calorimeter in the pseudorapidity region $1.6 < |\eta| < 1.8$ in beam tests,” *Nucl. Instrum. Meth.*, vol. A 531, pp. 481–514, 2004.

[65] “Jet energy measurement with the ATLAS detector in proton-proton collisions at $\sqrt{s} = 7$,” *Submitted to EPJ*, 2011.

[66] “Pile-up corrections for jets from proton-proton collisions at $\sqrt{s} = 7$ in atlas in 2011,” Tech. Rep. ATLAS-CONF-2012-064, 2012.

[67] “Jet energy measurement with the ATLAS detector in proton-proton collisions at $\sqrt{s} = 7$,” 2011.

[68] “Improved electron reconstruction in ATLAS using the Gaussian Sum Filter-based model for bremsstrahlung,” *ATLAS-PHYS-PUB-2011-007*, 2012.

[69] “Performance of the ATLAS Trigger System in 2010,” *Eur. Phys. J.*, vol. C72, p. 1849, 2012.

[70] “Search for the standard model higgs boson in the diphoton decay channel with $4.9\,\mathrm{fb}^{-1}$ of atlas data at $\sqrt{s} = 7$,” *ATLAS-CONF-2011-161*, 2011.

[71] “Measurement of the isolated di-photon cross-section in pp collisions at $\sqrt{s} = 7$ with the ATLAS detector,” *Phys. Rev.*, vol. D85, p. 012003, 2012.

[72] “The ATLAS simulation infrastructure,” *Eur. Phys. J.*, vol. C70, pp. 823–874, 2010.

[73] S. Alioli, P. Nason, C. Oleari, and E. Re, “NLO Higgs boson production via gluon fusion matched with shower in POWHEG,” *JHEP*, vol. 0904, p. 002, 2009.

[74] P. Nason and C. Oleari, “NLO Higgs boson production via vector-boson fusion matched with shower in POWHEG,” *JHEP*, vol. 1002, p. 037, 2010.

[75] T. Gleisberg, S. Hoeche, F. Krauss, M. Schonherr, S. Schumann, *et al.*, "Event generation with SHERPA 1.1," *JHEP*, vol. 0902, p. 007, 2009.

[76] F. Caravaglios, M. L. Mangano, M. Moretti, and R. Pittau, "A New approach to multijet calculations in hadron collisions," *Nucl.Phys.*, vol. B539, pp. 215–232, 1999.

[77] M. L. Mangano, M. Moretti, and R. Pittau, "Multijet matrix elements and shower evolution in hadronic collisions: $Wb\bar{b} + n$ jets as a case study," *Nucl.Phys.*, vol. B632, pp. 343–362, 2002.

[78] M. L. Mangano, M. Moretti, F. Piccinini, R. Pittau, and A. D. Polosa, "ALPGEN, a generator for hard multiparton processes in hadronic collisions," *JHEP*, vol. 0307, p. 001, 2003.

[79] "Updated luminosity determination in pp collisions at $\sqrt{s} = 7$ using the atlas detector," *ATLAS-CONF-2012-080*, 2012.

[80] M. Botje *et al.*, "The PDF4LHC working group interim recommendations," 2011.

[81] H.-L. Lai, M. Guzzi, J. Huston, Z. Li, P. M. Nadolsky, *et al.*, "New parton distributions for collider physics," *Phys. Rev.*, vol. D82, p. 074024, 2010.

[82] A. Martin, W. Stirling, R. Thorne, and G. Watt, "Parton distributions for the LHC," *Eur. Phys. J.*, vol. C63, pp. 189–285, 2009.

[83] R. D. Ball, V. Bertone, F. Cerutti, L. Del Debbio, S. Forte, *et al.*, "Impact of heavy quark masses on parton distributions and LHC phenomenology," *Nucl. Phys.*, vol. B849, pp. 296–363, 2011.

[84] A. Denner, S. Heinemeyer, I. Puljak, D. Rebuzzi, and M. Spira, "Standard Model Higgs-boson branching ratios with uncertainties," *Eur. Phys. J.*, vol. C71, p. 1753, 2011.

[85] G. Bozzi, S. Catani, D. de Florian, and M. Grazzini, "The q(T) spectrum of the Higgs boson at the LHC in QCD perturbation theory," *Phys.Lett.*, vol. B564, pp. 65–72, 2003.

[86] G. Bozzi, S. Catani, D. de Florian, and M. Grazzini, "Transverse-momentum resummation and the spectrum of the Higgs boson at the LHC," *Nucl.Phys.*, vol. B737, pp. 73–120, 2006.

[87] D. de Florian, G. Ferrera, M. Grazzini, and D. Tommasini, "Transverse-momentum resummation: Higgs boson production at the Tevatron and the LHC," *JHEP*, vol. 1111, p. 064, 2011.

[88] LHC Higgs Cross Section Working Group, S. Dittmaier, C. Mariotti, G. Passarino, and R. Tanaka (Eds.), “Handbook of LHC Higgs Cross Sections: 2. Differential Distributions,” *CERN-2012-002*, CERN, Geneva, 2012.

[89] I. W. Stewart and F. J. Tackmann, “Theory uncertainties for Higgs and other searches using jet bins,” *Phys. Rev.*, vol. D85, p. 034011, 2012.

[90] J. M. Campbell, R. K. Ellis, and C. Williams, “Hadronic production of a Higgs boson and two jets at next-to-leading order,” *Phys. Rev.*, vol. D81, p. 074023, 2010.

[91] “ATLAS tunes of PYTHIA 6 and Pythia 8 for MC11,” *ATL-PHYS-PUB-2011-009, online at https://cdsweb.cern.ch/record/1363300*, 2011.

[92] “Procedure for the lhc higgs boson search combination in summer 2011,” Tech. Rep. ATL-PHYS-PUB-2011-011, CERN, Geneva, Aug 2011.

[93] T. Skwarnicki, “A study of the radiative cascade transitions between the υ' and υ resonances,” DESY F31-86-02.

[94] G. Cowan, K. Cranmer, E. Gross, and O. Vitells, “Asymptotic formulae for likelihood-based tests of new physics,” *Eur.Phys.J.*, vol. C71, p. 1554, 2011.

[95] A. L. Read, “Modified frequentist analysis of search results (the cl_s method),” no. CERN-OPEN-2000-205, 2000.

[96] S. S. Wilks, “The Large-Sample Distribution of the Likelihood Ratio for Testing Composite Hypotheses,” *Ann. Math. Statist.*, vol. 9, pp. 60–62, 1938.

[97]

[98] J. Beringer and et al. (Particle Data Group), “Review of particle physics,” *Phys. Rev. D*, vol. 86, p. 010001, Jul 2012.

[99] E. Gross and O. Vitells, “Trial factors or the look elsewhere effect in high energy physics,” *Eur.Phys.J.*, vol. C70, pp. 525–530, 2010.

[100] G. Aad *et al.*, “Combined search for the Standard Model Higgs boson in pp collisions at $\sqrt{s} = 7$ TeV with the ATLAS detector,” *Phys.Rev.*, vol. D86, p. 032003, 2012.

[101] A. Hoecker, P. Speckmayer, J. Stelzer, J. Therhaag, E. von Toerne, and H. Voss, *TMVA 4 (Toolkit for multivariate data analysis with ROOT) Users Guide*. 2009.

[102] D. Rainwater, R. Szalapski, and D. Zeppenfeld, “Probing color-singlet exchange in $z+2$-jet events at the cern lhc,” *Phys. Rev. D*, vol. 54, p. 6680, Dec 1996.

[103] S. Gangal and F. J. Tackmann, “NLO Uncertainties in Higgs + 2 jets from Gluon Fusion,” 2013.

[104] J. M. Campbell and R. Ellis, “MCFM for the Tevatron and the LHC,” *Nucl.Phys.Proc.Suppl.*, vol. 205-206, pp. 10–15, 2010.

[105] “Summary of ATLAS Pythia 8 tunes,” *ATL-PHYS-PUB-2012-003*, Aug 2012.

[106] G. Aad *et al.*, “Measurements of Higgs boson production and couplings in diboson final states with the ATLAS detector at the LHC,” 2013.

[107] G. Aad *et al.*, “Evidence for the spin-0 nature of the Higgs boson using ATLAS data,” 2013.

[108] A. David *et al.*, “LHC HXSWG interim recommendations to explore the coupling structure of a Higgs-like particle,” 2012.

[109] “Search for tth production in events where h decays to photons at 8 tev collisions,” Tech. Rep. CMS-PAS-HIG-13-015, CERN, Geneva, 2013.